

Scaling Haline Flows in Saturated Heterogeneous Formations

Dissertation

zur Erlangung des akademischen Grades doctor rerum naturalium

(Dr. rer. nat.)

vorgelegt dem Rat der Chemisch-Geowissenschaftlichen Fakultät der
Friedrich-Schiller-Universität Jena

von

MSc. Jude Lubega Musuuza

geboren am 01.11.1975 in Rakai, Uganda.

Gutachter:

1. Prof. Dr. Sabine Attinger
2. Prof. Dr. Gabriel Wittum

Tag der öffentlichen Verteidigung: 22. Dezember 2010

Zusammenfassung. Die vorliegende Arbeit untersucht die Stabilität dichte-getriebener Strömungen in heterogenen porösen Formationen. Dichte-getriebene Strömungen entstehen durch Unterschiede im Salzgehalt oder der Temperatur innerhalb eines Fluids. Solche Strömungen treten in vielen Situationen auf wie etwa bei Sickerwasserbewegungen in Deponien oder nuklearen Endlagerstätten, beim Wärmetransport in geothermischen Systemen, bei Salzwasser-Intrusionen in Küstengebieten oder in der Erdölindustrie. Sie berühren viele praktische Anwendungen und deshalb kommt ihrer Untersuchung eine große Bedeutung zu.

In Abhängigkeit von der Richtung der dichte-bedingten Schichtung bezüglich der Strömungsrichtung treten stabile oder instabile Systeme auf. In diesem Sinne bedeutet “Stabilität” das Fehlen von ständigem Nachfließen eines Fluids in ein anderes. Andererseits ist unter “Instabilität” das kontinuierliche erratische Verdrängen eines Fluidkörpers durch einen anderen entlang einer Grenzfläche zu verstehen, das zur Ausbildung des Finger-Phänomens führt. Im Allgemeinen weist diese Finger-Bildung auf die Ausbreitung und das stetige Anwachsen kleiner Turbulenzen hin, die in das System durch physikalische Größen wie die Konzentration eingeführt werden. Bei der Modellierung dichte-getriebener Systeme können Instabilitäten auch numerische Ursachen haben, etwa wegen der Verwendung ungeeigneter numerischer Verfahren, einer ungenügenden Gitterverfeinerung oder (zu) großer Zeitschritte.

Instabile Systeme können zum Beispiel auftreten, wenn ein salzhaltiges Fluid ein salzärmeres überlagert, wenn eine viskose Flüssigkeit von einer Flüssigkeit mit einer höheren Viskosität verdrängt wird oder wenn ein kälteres Fluid ein wärmeres überlagert. Zusätzlich zu diesen Fluideigenschaften beeinflussen auch die Merkmale des Mediums wie Dispersion oder Heterogenität die Stabilität dichte-getriebener Strömungen. Insbesondere die Dispersion verwischt die Lösungswolke des transportierten Stoffs, wenn sie orthogonal zur Richtung der Finger-Ausbreitung auftritt. Dadurch verringern und stabilisieren sich die Konzentrationsgradienten, während Heterogenitäten das System stabilisieren oder auch destabilisieren können. Die dichte-bedingte Schichtung durch Salinitätsunterschiede wird in dieser Arbeit dargestellt.

Die notwendigen Gleichungen für die Untersuchung wurden hergeleitet, indem die

Homogenisierungs-Theorie (Entwicklung 2. Ordnung) auf die Gleichung des Lösungstransports angewandt wurde. Diese Theorie ist ähnlich wie die Volumennormierung ein Upscaling-Verfahren, genügt aber zusätzlich strikten mathematischen Beweisen der Existenz und Eindeutigkeit von Lösungen. Man erhält allgemein folgende drei Gleichungen: die *Verträglichkeitsbedingung* zeigt die Unabhängigkeit makroskopischer Größen von kleinen Skalen, die *Gleichung für kleine Skalen* drückt die mikroskalige Veränderung einer Interessensgröße (in unserem Fall des Massenanteils) aus und die *homogenisierte Gleichung* enthält den hochskalierten Tensor (in unserem Fall die Makrodispersion) als eine Funktion mesoskaliger Variablen (in unserem Fall sind dies der gelöste Stoff, die Geschwindigkeit und die Zeit).

Die Untersuchungen wurden in einem heterogenen Medium derart durchgeführt, daß die individuellen Einflüsse durch die Fluidmerkmale einerseits und die Mediumseigenschaften andererseits isoliert werden konnten. Ausgehend von der kleinskaligen Gleichung wurde ein Stabilitätskriterium für Strömungen in einem heterogenen Medium aus der zeitlichen Entwicklung des Lösungstransports abgeleitet. Die Lösung der kleinskaligen Gleichung hatte die Form $\omega_1(t) = \omega_1(0) \exp(-\Lambda t)$, wobei ω_1 die mesoskalige Lösung, t die Zeit und Λ eine Funktion ist, die den Dispersionstensor und die Einflüsse der mesoskaligen Lösung auf die Geschwindigkeitsfluktuationen enthält. Offensichtlich wächst ω_1 mit zunehmender Dauer unbegrenzt an oder verringert sich - je nach Vorzeichen von Λ , der *Stabilitätszahl*. Unbegrenztes Wachstum nach kleinen Störeinflüssen weist auf instabile Systeme hin. Der Ausdruck für die Stabilitätszahl war notwendig für das Kriterium, das intensiv durch eine variierende Geschwindigkeit, Dichte und Viskosität zu einer bestimmten Zeit getestet wurde.

Anschließend wurde das Kriterium erweitert, um auch die bisher vernachlässigten Dispersionseffekte zu berücksichtigen. Insbesondere untersuchten wir den Schwingungsbereich der Wellenlänge von Störeinflüssen, die durch kleinskalige Diffusion / Dispersion abgedämpft werden und ein Anwachsen der Finger unterdrücken. Eine Stabilisierung durch kleinskalige Diffusion / Dispersion tritt innerhalb einer charakteristischen Breite auf, der Dispersions-Mischungszone. Um das zu erreichen, wurden Verfahren zur Bestimmung einer kritischen cutoff-Wellenlänge sowie eine

analytische Funktion zur Beschreibung der Breite der Mischungszone ausgearbeitet. Störeinflüsse durch unterschiedliche Wellenlängen wurden als Randbedingungen der Zuflüsse eingesetzt und die Wellenlänge, bei der die Finger-Bildung einsetzt, wurde durch Simulationen ermittelt. Ein Ausdruck für die Breite der Mischungszone in Termen der Dispersivitäten wurde ebenfalls hergeleitet und gefittet ! gemäß physikalischer Bedingungen.

Die Variable Λ in den vorhergehenden Abschnitten wurde in Termen der (gelösten) Rayleigh-Zahl neu erfaßt, um einen Vergleich mit früheren Arbeiten anderer Wissenschaftler zu ermöglichen. Die Breite der Mischungszone und die longitudinale Komponente der Dispersion wurden verwendet, um die Rayleigh-Zahl zu berechnen. Dies erfolgte entgegen dem herkömmlichen Gebrauch der Gebietsgröße und des molekularen Diffusionskoeffizienten, der unkonditionierte instabile Systeme und einen großen numerischen Wert für die Rayleigh-Zahl zur Folge hatte.

Dieser zusätzliche dispersive Teil ermöglichte eine Vorhersage an Hand der Stabilitätszahl, ob ein oder mehrere Finger ausgebildet würden. Die Bildung von mehr als einem Finger weist auf eine beginnende Konvektion hin, die in direktem Bezug zur vorherrschenden physikalischen Stabilität des Systems steht. Unsere Wahl an Eingangsgrößen in die Berechnung der Rayleigh-Zahl führte uns zu der Schlußfolgerung, daß die Stabilität von vertikalen Strömungssystemen mit stark verfeinerten Gittern und Zeitschritten durch geeignete Veränderungen der physikalischen Variablen manipuliert werden könnte.

Das Kriterium wurde weiterhin ausgeweitet, um Heterogenitätseffekte des Mediums einzubeziehen, namentlich die Varianz und die Korrelationslänge. Dies wurde durch eine Zerlegung der effektiven Dispersivitäten des heterogenen Mediums in einen lokalen Anteil des homogenen Mediums und diejenigen Anteile umgesetzt, die durch die Heterogenität des Mediums entstehen. Die Untersuchung bestätigte, daß die Varianz der Heterogenität immer stabilisierend wirkt, wobei stabile Systeme nur mit Korrelationslängen unterhalb eines gewissen cutoff-Wertes möglich sind. Dieser cutoff-Wert der Korrelationslänge steht anscheinend in direkter Beziehung zur kritischen Wellenlänge der Störeinflüsse im homogenen Medium.

Das makroskopische Transportverhalten wurde ebenfalls unter Verwendung des homogenisierten Dispersionstensors untersucht. Dies erforderte die Auswertung der im Makrodispersionstensor enthaltenen Elemente durch die großskalige Gleichung der Homogenisierungstheorie. Der Tensor ist symmetrisch mit verschwindenden Nicht-Diagonaleinträgen. Die dominierenden Diagonal-Einträge sind Funktionen der Zeit, der Stabilitätszahl des homogenen Mediums sowie der Varianz, der Korrelationslänge und der Anisotropie des heterogenen Mediums.

Die Zeitabhängigkeit ermöglichte die Analyse der zeitlichen Entwicklung der Koeffizienten in Abhängigkeit von Veränderungen anderer Variablen. Insbesondere das Verhalten des Longitudinal-Koeffizienten lieferte nützliche Informationen hinsichtlich der Stabilität des Systems: stabile Systeme weisen asymptotische Koeffizienten auf, während instabile Systeme durch infinitesimal anwachsende Koeffizienten charakterisiert sind. Die asymptotischen Longitudinal-Koeffizienten zeigten auch den approximierten Schwankungsbereich von Dichteunterschieden, die durch die Heterogenitäten des Mediums stabilisiert wurden.

Die numerischen Simulationen wurden mit Hilfe des Software-Pakets d^3f durchgeführt. Feine Gitter (mindestens 831488 Elemente) und Zeitschritte (0,125 Stunden) wurden verwendet, die zu $Pe \approx 1,4 \times 10^{-2}$ beziehungsweise zu $Cr \approx 5 \times 10^{-5}$ führten. Auf diese Weise wurde die Stabilität der numerischen Lösung ohne die Anwendung von Upwind-Verfahren sichergestellt, was eine künstliche Diffusion einbringen würde.

Zusammenfassend läßt sich sagen, daß die Stabilität dichte-getriebener Strömungen sowohl in Abhängigkeit von den Fluid- als auch den Mediumseigenschaften untersucht wurde unter Verwendung von Gleichungen, die aus der Homogenisierungstheorie und den zugrundeliegenden Entwicklungen 2. Ordnung abgeleitet wurden. In homogenen Medien kommt der Dichte, der Topologie der Poren und der kleinskaligen Diffusion / Dispersion die hauptsächliche Bedeutung zu. Dies wiederum beeinflusst die Breite der Mischungszone und den Schwankungsbereich der Wellenlänge der Störeinflüsse, die zur Finger-Bildung führen können. Für heterogene Medien sind zusätzlich die Varianz und die Korrelationslänge von Bedeutung. Ein Bezug

zwischen der Stabilität und der Anzahl der gebildeten Finger wurde erarbeitet. Auf diese Weise ist es nun möglich, an Hand des Stabilitätskriteriums zu beurteilen, ob ein System diffusiv oder konvektiv ist und ob konvektive Systeme stabile oder instabile transiente Lösungen haben.

Summary. This thesis deals with the stability of density-driven flows in heterogeneous porous formations. Density-driven flows arise from differences in salinity or temperature within a fluid body. Such flows occur in many practical cases like leachate migration at normal and nuclear waste repositories, heat transport in geothermal systems, salty-water intrusion in coastal aquifers and in the petroleum Industry. They thereby cut across many practical applications and their study is of immense practical importance.

Depending on the direction of density stratification in relation to flow, the system can be stable or unstable. Stability in this sense means the absence of continuous etching of one fluid body into another. Instability on the other hand is the continued erratic displacement of one fluid body by another along the common interface, leading to the fingering phenomenon. Fingering generally indicates the propagation and continued growth of small disturbances introduced in the system via physical variables like concentration. In modelling density-driven systems, instabilities may also be numerical because of inappropriate numerical schemes, insufficient grid refinement or large time steps.

Systems are in general unstable when a more saline fluid overlays a less saline or when a less viscous fluid displaces a more viscous one or when a cooler fluid overlays a warmer one. In addition to those fluid properties, medium properties namely the dispersion and medium heterogeneity also play important roles in determining the stability of density-driven systems. Dispersion especially when acting orthogonal to the direction of finger propagation smears out the solute, thereby diminishing concentration gradients and stabilising while heterogeneities can stabilise or destabilise systems. The density stratification from salinity differences will be presented in this work.

The necessary equations for the study were derived by applying homogenization theory (2-scale expansion) to the solute transport equation. The theory is similar to volume averaging as an upscaling technique but can additionally satisfy rigorous mathematical proofs of existence and uniqueness of solutions. The following three equations (in general) result: *the compatibility condition* showing the inde-

pendency of the macroscopic quantities from small scales, the *small-scale equation* that expresses the small-scale variation of the variable of interest (in our case the mass fraction) and the *homogenized equation* that contains the upscaled (in our case macrodispersion) tensor as a function of the mesoscale variables (solute, velocity and time in our case).

The studies were conducted on a heterogeneous medium in such a way that the individual contributions from the fluid and medium properties could be isolated. Starting with the small-scale equation, a stability criterion for flow in a homogeneous medium was derived from the temporal evolution of the solute. The solution to the small-scale equation was in the form $\omega_1(t) = \omega_1(0) \exp(-\Lambda t)$, where ω_1 is the mesoscale solute, Λ a function containing the dispersion tensor and the contribution of the mesoscale solute to the velocity fluctuations and t the time. Clearly $\omega_1(t)$ grows indefinitely with time or decays to zero depending on the sign of Λ , the *stability number*. Indefinite growth with time after small perturbations is indicative of unstable systems. The expression for the stability number was the statement of the criterion, which was tested extensively by varying velocity, density and viscosity, one at a time.

The criterion was then extended to include the neglected dispersive effects. Essentially we analysed the range of perturbation wavelengths that could be damped out by small-scale diffusion/dispersion and prevented from growing into fingers. Stabilisation by small-scale diffusion/dispersion occurs within a certain characteristic width, the dispersion mixing zone. To that end, methods of determining the critical (cutoff) wavelength as well as an analytical function for the mixing zone width were devised. Perturbations of differing wavelengths were imposed as inflow boundary conditions and the wavelength at which fingering started were readily obtained from simulations. An expression for the mixing zone width in terms of the dispersivities was also derived and fitted subject to physical constraints.

The Λ in the preceding paragraphs was reformulated in terms of the (solutorial) Rayleigh number to enable comparison with earlier work by other researchers. The mixing zone width and the longitudinal dispersion were used to compute the Rayleigh

number. This was contrary to the traditional use of the domain size and molecular diffusion coefficient that result in unconditionally unstable systems and a big numerical value of the number.

With the dispersive part added, it was possible to predict from the stability number whether one or more fingers formed. The formation of more than one finger indicates the onset of convection, which is directly related to the prevailing physical stability of the system. Our choice of inputs into the Rayleigh number led to the conclusion that with highly refined grids and time steps, the stability of vertical flow systems could be manipulated by appropriate variations in physical variables.

The criterion was further extended to include medium heterogeneity effects, namely the variance and correlation length. This was done by decomposing the effective heterogeneous-medium dispersivities into the local from the homogeneous medium and the increments caused by the medium heterogeneity. The study confirmed that heterogeneity variance always stabilises while stable systems are only possible with correlation lengths below a certain cutoff value. The cutoff correlation length appeared to have a direct relationship to the critical perturbation wavelength in the homogeneous medium.

The macroscopic transport behaviour was also studied using the homogenized dispersion tensor. This required the evaluation of the elements in the macrodispersion tensor contained in the large-scale homogenization-theory equation. The tensor is symmetrical with zero off-diagonal elements. The leading diagonal elements are functions of time, the homogeneous-medium stability number; and the heterogeneous medium variance, correlation length and anisotropy.

The time dependency enabled the temporal evolution of the coefficients to be studied subject to changes in other variables. The behaviour of the longitudinal coefficient in particular provided useful information regarding the stability of the system: stable systems had asymptotic coefficients while unstable systems had infinitely growing coefficients. The asymptotic longitudinal coefficients also indicated the approximate range of density contrasts stabilised by medium heterogeneities.

The software package d^3f was used for the numerical simulations. Fine grid (atleast 831488 elements) and time steps (0.125 hours) were used resulting in $Pe \approx 1.4 \times 10^{-2}$ and $Cr \approx 5 \times 10^{-5}$ respectively. These ensured stability of the numerical solution without applying upwind techniques, which introduce artificial diffusion.

In summary, the dependency of density-driven flow stability on both fluid and medium properties was investigated using equations derived using homogenization theory and the underlying 2-scale expansions. For homogeneous media, the density, pore topology and small-scale diffusion/dispersion play the principal role. These determine the size of the mixing zone and the range of perturbation wavelengths that can persist into fingers. For heterogeneous media, the variance and correlation lengths additionally play important roles. A link between stability and the number of fingers was also established. It is now possible to tell from the stability criterion if the system is diffusive or convective, and whether the convective systems have stable or unstable transient solutions.

List of symbols

Symbol	Description	Units
p	Pressure	$N \cdot m^{-2}$
$\rho(\omega)$	Density	$kg \cdot m^{-3}$
ρ_0	Density of pure water	$kg \cdot m^{-3}$
ρ_{max}	Maximal density of saline solution	$kg \cdot m^{-3}$
α	Maximum relative density coefficient	
ω	Solute mass fraction	
ω_{max}	Maximal mass fraction	
\mathbf{g}	Gravitational acceleration	$m \cdot s^{-2}$
μ	Viscosity	$Pa \cdot s$
μ_0	Viscosity of pure water	$Pa \cdot s$
β	Maximum relative viscosity coefficient	
\mathbf{k}	Permeability tensor	m^2
ϕ	Porosity	
\mathbf{X}	unscaled spatial variable	m
L	Large scale spatial variable	m
l	Small scale spatial variable	m
\mathbf{x}	Dimensionless macroscale spatial variable	
\mathbf{y}	Dimensionless mesoscale spatial variable	
ϵ	l/L	
t	Dimensionless temporal variable corresponding to L	
τ	Dimensionless temporal variable corresponding to l	
\hat{t}	unscaled time	s
χ^ω	Solution to the cell problem	
\mathbf{q}	Spatial variable in Fourier space	
\mathbf{u}	Darcy velocity	$m \cdot s^{-1}$
\mathbf{v}	$\rho(\omega)\mathbf{u}/\phi$ Linear momentum of flow	$kg \cdot m^{-3} \cdot m \cdot s^{-1}$
\mathbf{v}_0	Average macroscopic velocity	$kg \cdot m^{-3} \cdot m \cdot s^{-1}$
$\tilde{\mathbf{v}}$	Velocity fluctuations	$kg \cdot m^{-3} \cdot m \cdot s^{-1}$

List of symbols

Symbol	Description	Units
v_0	Total downward velocity	$kg \cdot m^{-3} \cdot ms^{-1}$
v_0^p	Pressure-driven velocity component	$kg \cdot m^{-3} \cdot m \cdot s^{-1}$
\mathbf{v}^g	Total gravity-driven velocity	$kg \cdot m^{-3} \cdot m \cdot s^{-1}$
v_0^g	Gravity-driven velocity component	$kg \cdot m^{-3} \cdot m \cdot s^{-1}$
a	$-v_0^g/v_0^p$	
$\omega_1(\mathbf{q})$	Mesoscale mass fraction	
$\tilde{k}(\mathbf{q})$	Permeability heterogeneity	m^2
$\mathbf{M}(\mathbf{q})$	Dependency of $\tilde{\mathbf{v}}$ on $\omega_1(\mathbf{q})$	$kg \cdot m^{-3} \cdot m \cdot s^{-1}$
$\mathbf{L}(\mathbf{q})$	Dependency of $\tilde{\mathbf{v}}$ on $\tilde{k}(\mathbf{q})$	$kg \cdot m^{-3} \cdot m \cdot s^{-1}$
\mathbf{G}	Large scale concentration gradient	—
Λ_o	Stability number for flow orthogonal to gravity	
Λ_p	Stability number for flow parallel to gravity	
\mathbf{D}	Dispersion tensor	$m^2 \cdot s^{-1}$
\mathbf{D}^{eff}	Macrodispersion tensor	$m^2 \cdot s^{-1}$
D_m	Molecular diffusion coefficient	$m^2 \cdot s^{-1}$
D_{\parallel}, D_{\perp}	Longitudinal, transverse dispersion	$m^2 \cdot s^{-1}$
\mathbf{D}^{\star}	$\rho(\omega)\mathbf{D}/D_{\parallel}$	$kg \cdot m^{-3}$
$\alpha_{\parallel}, \alpha_{\perp}$	Longitudinal, transverse dispersivity	m
Pe	Péclet number	
Cr	Courant number	
\mathbf{e}_i	Unit vector in the i principal direction, $i = 1, 2$ or 3	
d	Number of spatial dimensions	
λ	Perturbation wavelength	m
λ_{crit}	Critical wavelength	m
ζ	Mixing zone width	m
Ra	Solutal Rayleigh number	-
Ra_{\parallel}	Longitudinal solutal Rayleigh number	-
λ_h, λ_v	Horizontal, vertical correlation lengths	m

List of symbols

Symbol	Description	Units
ξ	λ_h/λ_v Anisotropy ratio	
ε_j	Integral scale in direction j	
κ	$\frac{LG_n}{D_{\parallel}\rho(\omega)}$	
Θ	$\frac{4\pi\kappa\varepsilon_1\xi v_0\sigma_f^2}{\bar{k}^2}$	

“What we have to learn to do,
we learn by doing.”

by Aristotle

Contents

Zusammenfassung / Summary	i
List of Symbols	xi
1 Introduction	1
1.1 Motivation	1
1.2 Outline	3
2 General Concepts and Methodology	5
2.1 The Porous Medium and Density-driven Systems	6
2.1.1 Description of Flow and Transport Processes	8
2.2 The Stability of Density-driven Systems	12
2.2.1 Previous Stability Studies	14
2.2.2 The Balance and State Equations	20
2.3 The Current Work and Contributions	22
2.3.1 Overview of the Homogenization Theory	28
2.3.2 Overview of the d^3f Program	30
2.3.3 Model Set-up and Simulation Parameters	35
3 Stability Analyses for a Homogeneous Medium	39
3.1 Homogenization of the Transport Equation	40
3.2 The Small-Scale Stability Criterion	45
3.2.1 Systems Parallel to Gravity	47
3.2.2 Systems Orthogonal to Gravity	48
3.3 The Large-scale Stability Criterion	49

3.4	Numerical Results	50
3.4.1	The Schincariol Problem	50
3.4.2	Stability Investigations	51
3.4.2.1	Density Effects	53
3.4.2.2	Viscosity Effects	54
3.4.2.3	Flow velocity Effects	55
3.5	Discussion of Results	56
4	The Effects of Dispersion	59
4.1	Stabilising Effects of Small-Scale Dispersion	60
4.1.1	The Perturbation Wavelength λ	63
4.1.2	The Characteristic Scaling Length	64
4.2	Numerical Results	66
4.2.1	Determination of the Critical Wavelength	68
4.2.2	Derivation and Testing of the Proposed Mixing Zone Width .	69
4.2.3	Testing the Proposed Criterion	71
4.2.3.1	Density Effects	71
4.2.3.2	Longitudinal Dispersivity Effects	73
4.2.3.3	Transverse Dispersivity Effects	74
4.2.4	Discussion of Results	75
5	Stability Analyses for a Heterogeneous Medium	79
5.1	The Stochastic Permeability Field	79
5.2	Stability Analyses in Heterogeneous Media	81
5.2.1	Hypothesis	83
5.3	Large-scale Mixing in Heterogeneous Media	84
5.3.1	The Macrodispersion Coefficients	85
5.3.1.1	The Diagonal Elements	86
5.3.1.2	The Off-diagonal Elements	87
5.3.2	The Evolution of the Coefficients	87
5.3.2.1	The Coefficients without Density Effects	87
5.3.2.2	The Coefficients with Density Effects	88

5.4	Numerical Stability Analysis Results	93
5.4.1	Relation Between λ and λ_v : Effects of the Correlation Length	94
5.4.2	Density Effects	96
5.4.3	Medium Heterogeneity Effects	97
5.4.3.1	Effects of σ^2	97
5.4.3.2	Effect of the Medium Anisotropy ξ	98
5.4.4	Effect of Dispersivity	99
5.4.4.1	Effect of the Longitudinal Dispersivity α_{\parallel}	99
5.4.4.2	Effect of Transverse Dispersivity α_{\perp}	100
5.4.5	Discussion of Results	101
6	Discussion and Conclusion	105
6.1	Discussion	105
6.2	Conclusion	110
6.3	Outlook	111
A	Mathematical Derivations	113
A.1	Derivation of $\mathbf{M}(\mathbf{q})$	113
A.2	Derivation of $\mathbf{L}(\mathbf{q})$	116
A.3	Derivation of the Macrodispersion Tensor Elements	118
A.3.1	The Longitudinal Coefficient D_{11}^{eff}	120
A.3.2	The Transverse Coefficient D_{22}^{eff}	123
A.3.3	The Off-diagonal Elements.	123
	References	125
	Acknowledgements/Danksagung	137

List of Figures

2.1	The Representative Elementary Volume	6
2.2	The homogenization theory scales	7
2.3	Stable and unstable states	13
2.4	The origin of dispersion	15
2.5	Demarcation of the flow regimes by the stability criterion	25
2.6	The relation between Λ_p^* and the number of fingers	25
2.7	Construction of the cell-centred finite volume elements	31
2.8	Model set-up for the orthogonal system	35
2.9	Model set-up for vertical systems	36
3.1	A reproduction of Schincariol results with full equations	51
3.2	Decision between stable and unstable	52
3.3	Finger evolution in a bigger domain, $\rho = 1000 \text{ kg} \cdot \text{m}^{-3}$	52
3.4	Finger evolution in a bigger domain, $\rho = 1000.2 \text{ kg} \cdot \text{m}^{-3}$	53
3.5	Density effects	54
3.6	Density effects with the Oberbeck-Boussinesq approximation	54
3.7	Viscosity effects	54
3.8	Velocity effects	56
3.9	Evolution of fingers at conflicting stability predictions	57
4.1	Trough/Crest spacing for different wavelengths	63
4.2	The recirculation cells	66
4.3	The dependency of the number of fingers on Ra_{\parallel}	67
4.4	Relating the previous and current results	67
4.5	Estimation of the critical wavelength	68
4.6	Fitting the proposed dispersion zone width	69

4.7	α_{\parallel} for fitting the mixing zone width	70
4.8	α_{\perp} for fitting the mixing zone width	70
4.9	Testing the dispersion zone width	71
4.10	The onset of convection	72
4.11	Fingering at higher densities	72
4.12	The effect of α_{\parallel} in a homogeneous medium	73
4.13	The effect of α_{\perp} in a homogeneous medium	74
4.14	Effect of boundary condition on finger symmetry	75
5.1	Macrodispersion coefficients for passive tracers	88
5.2	Coefficients for favourable density and viscosity contrasts	89
5.3	Coefficients for unfavourable density and viscosity contrasts	90
5.4	D_{11}^{eff} for various λ_v	91
5.5	D_{22}^{eff} for various σ^2	92
5.6	Macrodispersion coefficients for various ξ	93
5.7	The critical correlation length at $\sigma^2 = 0.30$ and $\rho_{max} = 998.5 \text{ kg} \cdot \text{m}^{-3}$	94
5.8	The critical correlation length at $\sigma^2 = 0.40$ and $\rho_{max} = 998.5 \text{ kg} \cdot \text{m}^{-3}$	95
5.9	The critical correlation length at $\sigma^2 = 0.50$ and $\rho_{max} = 998.5 \text{ kg} \cdot \text{m}^{-3}$	95
5.10	The onset of fingering at $\sigma^2 = 0.40$ and $\lambda_v = 7.0 \times 10^{-3} \text{ m}$	96
5.11	The onset of fingering at $\sigma^2 = 0.60$ and $\lambda_v = 7.0 \times 10^{-3} \text{ m}$	97
5.12	The onset of fingering at $\sigma^2 = 0.65$ and $\lambda_v = 7.0 \times 10^{-3} \text{ m}$	97
5.13	The effect of increasing σ^2	98
5.14	The effect of medium anisotropy	99
5.15	The effect of α_{\parallel} in a heterogeneous medium	100
5.16	The effect of α_{\perp} in a heterogeneous medium	100
5.17	The regimes demarcated by the stability number	102

List of Tables

2.1	Simulation parameters	37
3.1	Density effects	53
3.2	Viscosity effects	54
3.3	Flow velocity effects	55
3.4	The impact of the Boussinesq Approximation	56
4.1	Testing the dispersion zone width	70
4.2	The new stability numbers for various densities	72
4.3	The effect of α_{\parallel} in a homogeneous medium	73
4.4	The effect of α_{\perp} in a homogeneous medium	74
5.1	Effect of λ_v	95
5.2	Effect of density in a heterogeneous medium	96
5.3	Effect of σ^2	98
5.4	Effect of α_{\parallel} in a heterogeneous medium	99
5.5	Effect of α_{\perp} in a heterogeneous medium	100

Chapter 1

Introduction

1.1 Motivation

The quest for energy is one of the main factors fuelling the un-sustainable exploitation of natural resources. Coal and hydropower drove the industrialisation of many nations but with climate change and the environmental problems related to coal, both have become less appealing in many parts of the world. Many developing nations like China, India, Iran and South Africa are looking at nuclear energy to drive their industrialisation, while the developed Norway, Denmark, Sweden and Germany are moving away from nuclear and venturing into greener alternatives. The radioactive refuse from nuclear plants requires very careful handling and its disposal in deep salt formations is overly expensive. Communities living in the vicinity of the repository sites e.g. Gorleben in Germany fiercely resist the continued deposition of nuclear waste in their localities. The detailed interactions between the nuclear material and the ambient aquifer systems are not clearly understood.

The deposition of waste generally changes the physical properties of aquifer systems i.e. the resident groundwater density, viscosity (and temperature in case of nuclear waste). The dissolution of solutes leads to systems in which flow and transport processes are purely driven by the density differences. In such *density-driven systems* the interface between regions with different densities can typically break down as a

result of the complex exchange of fluid between regions of different solute concentrations. The exchange can lead to the *fingering* phenomenon and the system is then said to be unstable.

Fingering alters both the flow velocity and mass of solute transported. The quantity of species transported have been found to exceed those predicted with passive tracers. The enhanced transport in density-driven systems invalidates break-through time predictions. For example a 15-day retention period was traditionally required for microorganisms to remove pathogenic bacteria like *E-coli* from groundwater. The 15-day retention periods were used to map out safe drinking water zones around contamination sources like barns on farms. The time is appreciably shorter in unstable density-driven systems and the rule is invalidated.

Research into density-driven phenomena was pioneered by Lord Rayleigh and later by Elder (1967), whose inspiring work has become a standard against which extensions are benchmarked. The flow and transport processes in density-driven systems are strongly coupled. Further research in the field was hampered by the limited computed resources and the absence of appropriate numerical codes. Robust codes (see list in Kolditz, Ratke, Diersch and Zielke (1998)) only became available in the 1980's and the field has attracted increasing attention ever since.

Dimensionless numbers were used to demarcate the stability regimes of density-driven systems. Even then, there is no known stability criterion that can make use of physical variables to predict the onset of fingering in density-driven systems. This work is a derivation and testing of such a criterion. A combination of both fluid and medium properties will be investigated. Viscosity and dispersion are known to stabilise while the density and temperature destabilise. The flow velocity can also stabilise or destabilise according to its direction in relation to finger development. The medium heterogeneity is known to stabilise through increased mixing but also destabilise if for example the arrangement of the permeability blocks offers preferential flow paths.

The specific objective of this work is to derive a stability criterion that quantifies the effects of density, viscosity, dispersion and medium heterogeneity and use the

criterion to predict the onset of fingering. We intend to specifically investigate the effects of the density contrast and the role played by dispersion lengths and perturbation wavelengths as well as the individual medium heterogeneity properties. These effects will be formulated into a criterion.

A medium saturated with a single liquid phase (water) in which a solute is completely dissolved will be considered. The software package d^3f (Fein and Schneider 1999) will be used for the numerical simulations.

1.2 Outline

The remainder of this work is organised as follows: general ideas about modelling flow and transport processes in porous media and the methodology used in this work are presented in chapter 2. A review of previous work on stability and a typical derivation of the flow and transport equations from the Reynolds transport theory are also presented there.

The balance equations needed to solve a density-driven system, the state dependencies, a brief review of the Oberbeck-Boussinesq approximations and an overview of the homogenization theory are also presented in chapter 2. The current work and its contributions, a typical implementation of a Boundary Value Problem in the d^3f program and the model setup and simulation parameters used in this work are presented at the end of the chapter.

The application of the homogenization theory to the transport equation to derive the small- and large-scale equations is presented in chapter 3. The treatment of the small-scale equation to derive the stability criterion for flow in a homogeneous medium is also given there. The definition of an optimal grid using the problem from Schincariol, Schwartz and Mendoza (1997) is also presented there. The results of testing the derived criterion for the effects of density, viscosity and velocity are presented there as well. A comparison of the results obtained in this work to others derived by invoking the Boussinesq approximation is presented at the end of the

chapter.

The earlier criterion is reformulated in terms of a Rayleigh number and extended to include dispersion in chapter 4. It is also there that a method is devised to determine the critical perturbation wavelength. Basing on physical considerations, an analytical function for the mixing zone is derived, fitted and tested. The extended criterion is then tested for the onset of convection and subsequent development of fingers. The effects of density and dispersivity are also tested and the results are presented there as well.

The extension of the criterion to include medium heterogeneities is given in chapter 5. The results from testing the criterion for the effects of density, medium heterogeneity and dispersivity are presented there. The application of the large-scale homogenization theory equation to study large-scale mixing is presented there as well. The macrodispersion coefficients are derived and their temporal evolution presented for a range of physical variables. A stability criterion is finally stated at the end of the chapter to predict the onset of unstable convection in density-driven systems.

A discussion of results, conclusion and outlook are presented in chapter 6 while the derivation of mathematical formulas is finally presented in Appendix A.

Chapter 2

General Concepts and Methodology

This chapter introduces the general ideas regarding the modelling of flow and transport processes in porous media, particularly soil. Previous stability studies and the contributions from the current work are also presented here as well as the system of equations required to solve a density-driven system. The homogenization theory procedure is also introduced and its application to the various equations and the different possible outcomes briefly explained. The procedure followed in the implementation of a typical problem in the d^3f program is also presented and briefly explained.

The model setups used in this work to study the different flow configurations and the reference simulation parameters are also presented here.

Throughout the work, a medium saturated with water in which a solute is dissolved will be considered. It is also assumed that a homogeneous liquid phase is maintained upon dissolution and the solute neither reacts with nor adsorbs on the soil matrix. The absence of sources and sinks is further assumed and we do not invoke the Oberbeck-Boussinesq approximations.

2.1 Flow and Transport in Porous Media

Porous media are generally made up of a solid matrix and a void space in which one or more phases may reside. The void space is assumed to be interconnected (see Bear and Bachmat (1991) for types of connectivities) without dead ends. The ratio of the voids to the total volume is defined as the porosity of the medium. Flow and transport processes occur within the void space at the pore scale but due to the immense amount of data and the uncertainty regarding the individual pore geometry and topology, the pore-scale quantities are up-scaled to another scale (Bear and Bachmat 1991, Kolditz 2001) where measurements can be reasonably made.

The continuum hypothesis which neglects the particulate nature of matter and assumes it to be continuous throughout the domain is adopted. Matter can then be described by a set of variables that are continuous and differentiable functions in space and time. To realise a continuum either spatial averaging (Bear and Bachmat 1991) or homogenization theory (Hornung 1996) techniques have to be used. Hornung (1996) distinguishes the two methods according to their respective methodologies: spatial averaging uses the *representative elementary volume* REV while homogenization achieves the upscaling by letting the microscale vanish to zero. The REV shown as the range $r_1 \leq r \leq r_2$ in Fig. 2.1 should be sufficiently large so that the inhomogeneity of the averaged microscopic quantity vanishes but small enough to preserve the macroscopic heterogeneity.

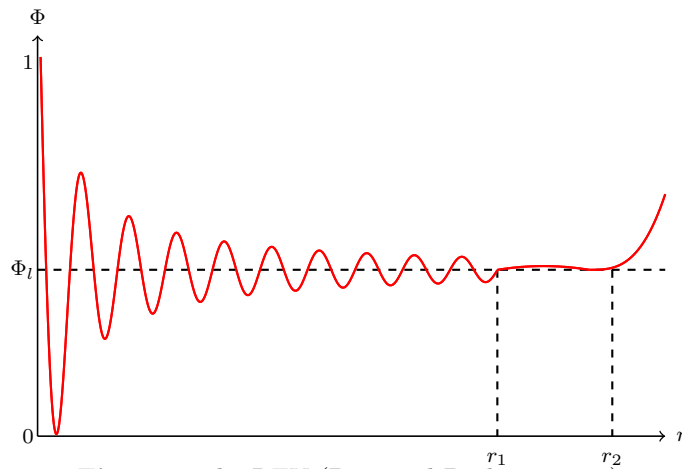


Fig. 2.1 The REV (Bear and Bachmat 1991)

A rapidly oscillating real-valued function u can be smoothened by local averages of the form $\langle u \rangle(x) = \int_{V(x)} u(y) dy$ where $V(x)$ is a neighbourhood of x of the size REV. Homogenization theory on the other hand works with a family of functions u^ϵ , defined on two spatial scales l and L shown in Fig. 2.2. The scales are assumed to be well-separated $L \gg l$ and the functions u^ϵ to oscillate rapidly on l but change slowly on L . The hydraulic conductivity and porosity are prominent examples that exhibit such variability. A spatial parameter $\epsilon := l/L$ is further defined and the problem in question considered to be part of the family of functions.

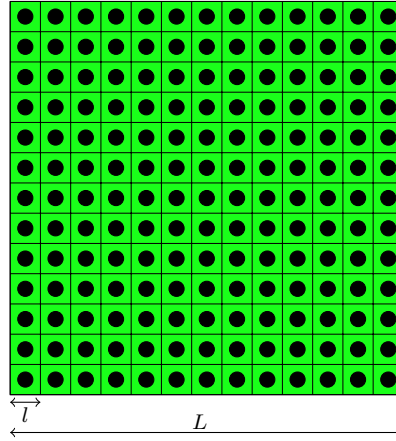


Fig. 2.2 The two homogenization theory scales (Attinger 2006)

The limit $u = \lim_{\epsilon \rightarrow 0} u^\epsilon$ is taken to be a result of the upscaling process. Homogenization then consists of finding differential equations that the limit satisfies and proving certain properties of the differential equations. The ability of homogenization theory to withstand rigorous mathematical scrutiny e.g. proofs of existence and uniqueness of solutions gives it an edge over spatial averaging.

According to (Bear and Bachmat 1991), the continuum model has the following advantages:

- i. Specifying the exact configuration of the interphase interface is not necessary
- ii. It describes pore-scale processes in terms of differentiable quantities, thus enabling solutions to problems via mathematical analysis
- iii. The mesoscale quantities are measurable and useful in practical problems.

The continuum model and homogenization theory were used to up-scale the flow and transport processes.

2.1.1 Description of Flow and Transport Processes

This section develops a model that describes density-driven flow and transport processes at the macroscopic level. The model consists of constitutive relations describing the properties of the phases involved and balance equations for the species being transported and initial and boundary conditions stated at the macroscopic level.

Reynolds Transport Theory

The observation of processes within a defined control volume enables a simplified mathematical description of complex problems. Two approaches can be distinguished: the *Lagrangian* where the control volume moves and paths of individual particles are tracked and the *Eulerian* in which the control volume is stationary. In the latter approach, one is interested in an averaged property e.g. concentration of a cloud of particles. The properties are assumed to be a spatial continuum and partial differential equations can be used to describe them.

Let a fluid flow into a control volume Ω_V through an area A , with velocity \mathbf{u} , which is in general not constant across A and not in the direction of the normal vector \mathbf{n} . The *volume flux* $Q[m^3/s]$ is defined by

$$Q = \int_{\partial\Omega_V} (\mathbf{u} \cdot \mathbf{n}) dA . \quad (2.1)$$

By convention \mathbf{n} points outwards and an inflow or outflow determines the sign of the flux. Multiplying Q with the density $\rho(\omega)$ gives the *mass flux* $\dot{m} [kg/s]$:

$$\dot{m} = \rho(\omega) Q . \quad (2.2)$$

This work concerns density-driven systems hence the explicit dependency of ρ on ω

in (2.2). The *mass fraction* ω is the dimensionless form of concentration $c [ML^{-3}]$, implemented in the software package d^3f . They are related via $c = \omega\rho(\omega)$. The same treatment is however valid for non density-driven systems. Generally if B is an arbitrary extensive property¹ of a flow field e.g. mass, energy or momentum, an extensive value $b = dB/dm$ related to the mass can further be defined. The total amount of B in a control volume is given by

$$B = \int_{\Omega_V} b\rho(\omega) d\Omega_V . \quad (2.3)$$

One is usually interested in the temporal changes of B within Ω_V . The contributions are the accumulation of B within Ω_V ; the in- or out-fluxes of B across the control surfaces of Ω_V and its rate of internal production (Helmig 2004). This is the *Reynolds Transport Theory* which can be formulated as

$$\frac{dB}{dt} = \overbrace{\int_{\Omega_V} \frac{\partial}{\partial t}(b\rho(\omega)) d\Omega_V}^{\text{accumulation term}} + \overbrace{\int_{\partial\Omega_V} b\rho(\omega)(\mathbf{u} \cdot \mathbf{n})dA}^{\text{boundary fluxes}} + \overbrace{\int_{\Omega_V} R(b\rho(\omega)) d\Omega_V}^{\text{sources/sinks}} . \quad (2.4)$$

Equation (2.4) is only valid for control volumes that do not change in space. In case of deformable control volumes, the relative velocity \mathbf{u}_r between the fluid and the control volume is used instead of \mathbf{u} . Non deformable control volumes are considered in this work and source/sink terms are neglected.

The flux term is composed of advective and dispersive parts, which must be considered separately because of the difference in time scales over which they occur. Using the theorem of Gauss, the flux perpendicular to a closed surface can be written as the divergence of that flux within the volume. Furthermore, integration and differentiation can be interchanged since the control volume does not deform (Helmig 2004).

¹A property that depends on the quantity of material in a system while intensive properties like viscosity, temperature and density do not.

Equation (2.4) can be rewritten for a general extensive thermodynamic property as

$$\int_{\Omega_V} \frac{\partial}{\partial t} b \, d\Omega_V + \int_{\Omega_V} \nabla \cdot \mathbf{j}(b) \, d\Omega_V = 0 \quad , \quad (2.5)$$

where $\mathbf{j}(b)$ is the flux within the control volume. The quantity b must be a continuous and integrable function on $\Omega \times (0, T] \rightarrow \mathbb{R}$. $\Omega \subset \mathbb{R}^d$ is an open subset of the physical space in d dimensions and $(0, T]$ is a finite time interval. Since (2.5) holds pointwise in the control volume, the integral signs can be dropped leading to

$$\frac{\partial}{\partial t} b^{(k)} + \nabla \cdot \mathbf{j}^{(k)} = 0 \quad , \quad (2.6)$$

where k is in general any constituent in the fluid phase.

The Nabla Notation ∇

The nabla notation is a shortened way of writing multi-dimensional spatial derivatives. For a scalar s and vector \mathbf{u} in 2-D, the operator is defined by the following respective vector and scalar (Holzbecher 1998):

$$\nabla s = \begin{pmatrix} \frac{\partial s}{\partial x} \\ \frac{\partial s}{\partial y} \end{pmatrix} \text{ and } \nabla \cdot \mathbf{u} = \frac{\partial u_x}{\partial x} + \frac{\partial u_y}{\partial y} \quad . \text{ The operation } \nabla \cdot \mathbf{u} \text{ represents the dot multiplication of vectors, thus the scalar outcome.}$$

The Accumulation Term

Generally, the mass accumulation term in (2.6) is given by

$$b^{(k)} = \phi \rho(\omega) \omega^{(k)} \quad , \quad (2.7)$$

where ϕ is the porosity and $\omega^{(k)}$ is the mass fraction of the k^{th} fluid component in the system. $k = 1$ in this work. The dependency of density on salinity in density-driven systems has to be specified before hand in order to close the system (see section 2.2.2).

The Flux Term

The following assumptions are usually made for ground water flow (Kolditz 2001):

- advective flux by the bulk fluid flow is much larger than the sum of diffusive and dispersive fluxes
- The inertia and convective acceleration terms can be neglected
- Macroscopic dispersive fluxes may be written according to Fick's law.

The fluxes in the subsurface are driven by advection and hydrodynamic dispersion and can be written as a sum

$$\mathbf{j} = \mathbf{j}_{\text{adv}} + \mathbf{j}_{\text{disp}} , \quad (2.8)$$

where \mathbf{j}_{adv} and \mathbf{j}_{disp} are the advective and dispersive fluxes respectively. The hydrodynamic dispersion is composed of the mechanical dispersion and molecular diffusion. Depending on the nature of the system, it is usual to consider only the predominant processes and talk about convection- or diffusion-dominated systems. Convection-diffusion systems are also possible when both processes are relevant.

The Advective Flux

The advective flux is defined as the quantity of substance transported by mean drift

$$\mathbf{j}_{\text{adv}} = \rho(\omega)\omega\mathbf{u} . \quad (2.9)$$

The velocity \mathbf{u} can be readily obtained from Darcy's law.

The Dispersive Flux

The dispersive flux is obtained from Fick's second law

$$\mathbf{j}_{\text{disp}} = -\phi\rho(\omega)\mathbf{D} \cdot \nabla\omega , \quad (2.10)$$

where the dispersion tensor \mathbf{D} is composed of the diffusive and hydrodynamic parts and is second-order symmetric in one principal direction and another normal to it. The tensor is implemented according to Scheidegger's law:

$$\mathbf{D} = D_m \mathbf{I} + (\alpha_{\parallel} - \alpha_{\perp}) \frac{\mathbf{v} \otimes \mathbf{v}}{\|\mathbf{v}\|} + \alpha_{\perp} \|\mathbf{v}\| \mathbf{I} , \quad (2.11)$$

where \mathbf{I} is an identity matrix, D_m the molecular diffusion coefficient, $\alpha_{\parallel}, \alpha_{\perp}$ the respective longitudinal and transverse dispersion lengths and $\mathbf{v} = \mathbf{u}/\phi$ the velocity with the norm $\|\mathbf{v}\| = \sqrt{\mathbf{v} \cdot \mathbf{v}}$.

2.2 The Stability of Density-driven Systems

Variable density flows arise in many practical applications like thermally induced flows in deep aquifers for geothermal energy exploration, oil recovery from aquifers, contaminant migration at normal and nuclear waste disposal facilities and concentration gradient-induced saline water intrusion in coastal aquifers. In all these systems, salinity or temperature differences cause density stratification which drives the flow and transport processes.

The systems are non-linear due to the coupling in the fluid flow and solute transport, which makes them difficult to solve. Spatial and temporal density variations are fundamental because many different but physically correct flow patterns may arise (Diersch and Kolditz 2002). In particular, density-driven systems may show unstable behaviour. A prominent example is the salty and freshwater system. If the salty water is on top, unstable salty fingers intruding into the freshwater can be observed whereas the reverse configuration shows no fingering. The first configuration is physically unstable while the latter is stable. The derivation of criteria to predict stability behaviour transitions in density-driven systems is still a challenge (Simmons, Fenstermaker and Sharp 2001).

The phenomenon of instability can be explained physically by taking into account the forces that act on density driven fluids at rest or in motion. They may individually

have stabilising or destabilising effects to the system. A stable system is in general attained when the external forces like inertia, viscous stresses and buoyancy balance and a state of minimum energy is reached in which no states of lower energy are accessible. A perturbed system moves back to this stable state e.g. point A in Fig. 2.3. In contrast, the system shows unstable behaviour if states of lower energy are accessible and an infinitesimal perturbation causes it to evolve to a different state with lower energy e.g. point B in Fig. 2.3.

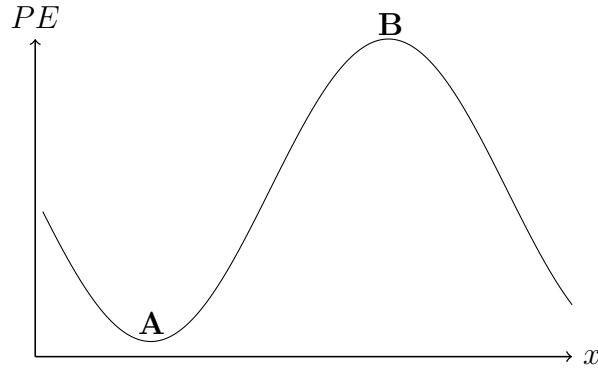


Fig. 2.3 Stable and unstable states

Viscosity dissipates the energy of a disturbance and stabilises the system. For this reason, any bounded flow is stable if viscosity is large enough (Drazin and Reid 2004). It can also diffuse momentum, thereby some systems like parallel shear flow show unstable behaviour although the same are stable in an inviscid fluid. Thermal conductivity and molecular diffusion smoothen out temperature and concentration gradients respectively and so have stabilising effects. Buoyancy forces have a destabilising effect when a denser liquid lies on top of a less dense one. Boundaries constrain the development of instabilities and the closer boundaries are the more stable a system becomes (Drazin and Reid 2004). Boundaries can however result into stronger shear in boundary layers, which leads to instabilities when diffused out by viscosity.

In principle, an unstable configuration results when a denser fluid overlays a less dense one as was already described above. However, such a system can still remain stable if the mobility (viscosity) term does not favour finger formation (Holzbecher

1998) or when the velocity, normal to the direction of finger development is so high that instabilities form but have no time to grow into fingers; or when mixing from dispersion and medium heterogeneities smoothes them out. This work attempts to combine a number of physical variables into a stability criterion and use it to predict the onset of fingering in density-driven systems.

In addition to physical instabilities, numerical instabilities may be introduced by inappropriate numerical schemes. The corresponding mathematical models often provide numerically non-unique solutions (Diersch and Kolditz 2002), which according to Oldenburg and Pruess (1995) and Frolkovič and De Schepper (2001) arise from insufficient grid refinement and extrapolation of the initial conditions if the grid is not aligned with the sides of the domain. In mathematical analysis the first step is to determine the original state of the system, which is referred to as the basic state. In density driven flows, the basic state involves velocities, pressures and solute concentrations. The numerical solution must satisfy the describing equations as well as the applicable boundary conditions.

Physically, one wishes to know whether the basic state can be observed or not. If it is disturbed even so slightly, the perturbation decays away or grows in magnitude. Growth continues infinitely or evolves to another steady-state, which thermodynamically means another state with lower energy.

2.2.1 Previous Stability Studies

Early stability studies are documented in Chang and Slattery (1986) where tribute is paid to the pioneering works of both Lord Rayleigh and Elder. It is also mentioned how some e.g. Wooding (1962) studied the stability of vertical miscible displacements in homogeneous media and concluded that the interface could be stable or unstable depending on the wavenumber. They also document how others like Perrine and Gay (1966) wrongly concluded that instabilities could not form in homogeneous media, while subsequent ones like Settari, Price and Dupont (1977) showed that instabilities could form in homogeneous media provided mixing effects were sufficiently small.

Experimental stability studies can be found in e.g. Schincariol and Schwartz (1990), Liu and Dane (1996a) and Wang (2002) while numerical studies are documented in Wooding (1962), Chang and Slattery (1986; 1988), Coskuner and Bentsen (1990), Coskuner (1993), Schincariol, Schwartz and Mendoza (1994), Schincariol et al. (1997), Kretz, Berest, Hulin and Salin (2003), Chao-Ying and Hoetzi (2004), Held, Attinger and Kinzelbach (2005) and Kuznetsov and Nield (2008). Gravity-driven flow was studied by Tan and Homsy (1986), Chikhliwala, Huang and Yortsos (1988), Ursino (2000), Eliassi and Glass (2001), Dautov, Egorov, Nieber and Sheshukov (2002), Egorov, Dautov, Nieber and Sheshukov (2003), Van-Duijn, Pieters and Raats (2004) and Brailovsky, Babchin, Frankel and Sivashinsky (2006) whereas Pieters (2004) investigated both.

No stability criteria were developed in most of the works listed above. However, a criterion was derived in Coskuner and Bentsen (1990) and was extended by Coskuner (1993) to investigate the effect of domain dimensions on flow stability. The effects of density and viscosity on macrodispersion were studied by Welty and Gelhar (1991) who derived an expression that was later used by Kretz et al. (2003) for stability analyses. Held et al. (2005) also derived a stability criterion for density-driven flow that is the basis of this work.

Apart from fluid properties mentioned previously, medium properties also play a crucial role in determining the stability of systems. Diffusion and small-scale dispersion are the main stabilising mechanisms (Landman, Johannsen and Schotting 2007). Figure 2.4 shows the origin of small-scale dispersion: variable size and orientation of pores and non uniformity of velocity within individual pores (Holzbecher 1998, Fetter 1999). The spreading causes a mixing zone to develop whose width increases

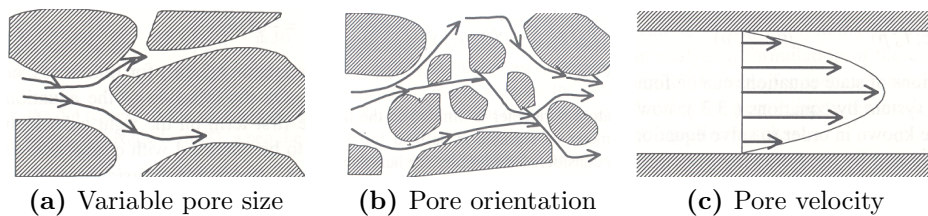


Fig. 2.4 The origin of dispersion (Holzbecher 1998)

with the prevailing diffusion/dispersion, in accordance with the scale-dependency of dispersion (Gelhar and Axness 1983, Dagan 1987; 1988; 1990, Kempers and Haas 1994, Kitanidis 1998). Flow is stable at the small scale only when the spreading (and therefore the mixing zone) is big enough to prevent the instabilities from growing into fingers. Even then instabilities with big enough wavelengths can still develop into fingers. The stability of a system is thereby controlled by the perturbation wavelength and the width of the mixing zone (Marle 1981, Simmons et al. 2001).

Most of the investigations here will be limited to downward flow, solely driven by density differences. The stability of such systems was initially studied by Lord Rayleigh and later by Elder (1967) whose inspirational work became a benchmark for studying convective systems. He used the Rayleigh and other dimensionless numbers to investigate the onset of convection in a system heated from below. Over the years, other researchers like Oldenburg and Pruess (1995), Diersch and Kolditz (1998), Holzbecher (1998), Kolditz et al. (1998), Oldenburg and Pruess (1998), Reeves and Ewiera (2000), Frolkovič and De Schepper (2001), Diersch and Kolditz (2002), Johannsen (2002; 2003) have used the haline equivalent of the original thermal Elder problem to study convection patterns caused by salinity stratification. Many of these reported differences in fingering patterns depending on the level of grid refinement and the density contrast. For sufficiently refined grids, Oldenburg and Pruess (1995), Diersch and Kolditz (1998) and Frolkovič and De Schepper (2001) observed comparable finger evolutions.

The solutal Rayleigh number Ra_s is the ratio of the destabilising buoyancy to the stabilising viscous and dispersive forces (Simmons et al. 2001) and is approximately 400 (Oldenburg and Pruess 1995, Diersch and Kolditz 1998, Holzbecher 1998, Kolditz et al. 1998, Oltean, Felder and Buès 2000, Johannsen 2002, Johannsen, Kinzelbach, Oswald and Wittum 2002). Only molecular diffusion is taken into account, which is erroneous considering the 20% density contrast and the evident convection patterns in most of the results. The entire domain height (150m for the classical Elder problem) is also used in the computation.

Alternative formulations for the Rayleigh number that take dispersion into account

can be found in e.g. Schincariol et al. (1997), Reeves and Ewiera (2000) and Diersch and Kolditz (2002). Schincariol et al. (1997) further proposed the use of a characteristic length instead of the entire domain size but also pointed out the problems pertaining to what it should actually be.

The *classical haline Elder problem* described above is subsequently referred to as the *Elder problem* and the subscript in Ra_s is dropped henceforth. For the Elder problem, Diersch and Kolditz (2002) identified 3 regimes and correspondingly 2 critical Rayleigh numbers:

- i. **The predominantly diffusive regime** for Rayleigh numbers smaller than the first critical, $Ra_{c_1} \approx 4\pi^2$
- ii. **The convective regime** with stable numerical solutions for $4\pi^2 \leq Ra \leq Ra_{c_2}$, with the second critical number Ra_{c_2} in the range $240 - 300$
- iii. **The unstable convective regime** for $Ra > Ra_{c_2}$.

Johannsen (2002) independently showed that the number of fingers evolved from one for very small Ra to three (in some solution branches) at $Ra > 300$, with the latter coinciding with the second critical number in Diersch and Kolditz (2002) for the onset of the unstable convective regime.

Natural porous media are heterogeneous with the hydraulic conductivity showing spatial variability. Schincariol (1998) studied the role of local scale heterogeneities in the initiation of perturbations: how perturbations could be stabilised in certain regions or developed into fingers in others. Swartz and Schwartz (1998) carried out flow-tank experiments with layered media and analysed the effects of flow rate, density contrast and permeability differences on mixing patterns of unstable flow configurations and were able to reasonably predict the wavelengths of the ensuing fingering patterns.

As a consequence of the conductivity heterogeneity, flow and transport processes show spatial variability as well. A stochastic modelling approach that treats hydraulic conductivity as a random variable in space (Welty and Gelhar 1991, Gelhar

1993, Kitanidis 1998, Dentz 2000, Rubin 2003, Welty, Kane III and Kauffman 2003) is usually employed to offset the data requirements. The spatially varying conductivity field in a given aquifer is identified with one single realisation of a spatial stochastic process defined by the ensemble of all possible realisations (Gelhar 1993, Dentz 2000, Rubin 2003). Spatial statistical invariance or second order stationarity is usually assumed so that the ensemble average does not depend on position but rather on the magnitude and orientation of the vector separating any two points.

Different degrees of heterogeneities exist at different scales in heterogeneous media and cause spreading effects similar to dispersive mixing. However unlike dispersive mixing which is always a stabilising mechanism, heterogeneities trigger instability formation at small scales but can promote or suppress finger formation at the larger scales. To this end, heterogeneities may cause spreading effects that stabilise unstable flow conditions on one hand but can also favour finger formation on the other. This leads to the central question: under which conditions do heterogeneities stabilise or destabilise density-driven flow?

In the case of conservative solute or tracer transport, heterogeneities cause mixing or increased dispersivity against the local values. Several methods exist for the determination of macrodispersion coefficients: volume averaging (Kitanidis 1998, Wang and Kitanidis 1999); stochastic theory (Gelhar and Axness 1983, Dagan 1986; 1987; 1988; 1990, Gelhar 1993); and homogenization theory (Held et al. 2005).

The scale-dependency (increase with the travel distance) of dispersion is documented in e.g. Gelhar and Axness (1983), Dagan (1987; 1988; 1990), Buès and Aachib (1991), Kempers and Haas (1994), Irwin, Botz and Greenkorn (1996), Kitanidis (1998), Attinger, Dentz, Kinzelbach and Kinzelbach (1999), Fetter (1999) and Hsu (2003). The earlier experimental work of Irwin et al. (1996) investigated the scale dependency of longitudinal dispersion and found that the coefficient reached an asymptotic limit after about 20-30 hydraulic units. That conclusion was consistent with the earlier work of Dagan (1988) who found that asymptotic behaviour was attained after travel distances of the order of tens of conductivity scales. Dagan (1987; 1988) and Kitanidis (1998) point out that solute transport does not neces-

sarily satisfy the advection-diffusion equation. Dagan (1988) and Kitanidis (1998) mention that the equation is only applicable in the asymptotic regime.

Fetter (1999) explains the scale dependence of dispersion as follows: as the flow path becomes longer, the transported solute samples more and more variations in conductivity. Consequently, the deviations of the velocity from the mean become bigger, resulting in increased dispersion. If the flow path is long enough so as to sample all possible conductivity variations, the dispersion reaches a maximum: the asymptotic limit mentioned above.

It is also documented in e.g. Tan and Homsy (1986), Dagan (1987) and Dentz (2000) that field-scale longitudinal coefficients are orders of magnitude larger than those determined from experimental samples. This is also explained by the larger heterogeneity scales encountered in natural formations.

In the numerical studies of flow and transport in heterogeneous media, the arrangement of permeability zones in the domain depends on how the permeability field is generated. Simmons et al. (2001) compared statistically random to periodic fields and showed how unrealistic fingers developed in the latter even for favourable density and viscosity contrasts. Hsu (2003) also investigated the influence of the log-conductivity auto-covariance structure on the macrodispersion coefficient. He compared the exponential, Gaussian, spherical and linear models and reported slight differences in the pre-asymptotic regions but no effect on the ultimate macrodispersion coefficients. He concluded that non-ergodicity effects are more significant than the log-conductivity auto-covariance functions. The stochastic method in which non-ergodicity is implied (Dagan 1988, Attinger et al. 1999, Dentz, Kinzelbach, Attinger and Kinzelbach 2003) would then be the most appropriate method by which to study dispersion.

Dentz et al. (2003) assumed a vanishing concentration at infinity and a normalised initial concentration distribution to derive the first and second moments of the solute distribution. The two moments can be used to characterise the solute distribution in the domain, giving respectively the position of the centre of mass of the plume and the squared width of the plume in a given direction at any time. The first

time-derivative of the second centred moment was used by e.g. Kitanidis (1998) and Dentz (2000) to obtain the effective dispersion coefficient.

Heterogeneous mixing has been studied by observing the transient evolution of the macrodispersion coefficients (Welty and Gelhar 1991, Kretz et al. 2003, Welty et al. 2003, Held et al. 2005). It was shown in Welty and Gelhar (1991) that flow configurations that favour finger formation give rise to infinitely large longitudinal mixing under conditions of large displacement. Kitanidis (1998) used a similar argument by imposing as boundary conditions that particles travel finite distances and square distances in finite times. Landman, Johannsen and Schotting (2007) and Landman, Schotting, Egorov and Demidov (2007) considered the effects of stable density contrasts and noted a reduction in dispersive mixing. Woumeni and Vauclin (2006) reported big ranges in dispersivities for stable configurations in the same aquifer due to heterogeneity and scale effects. The role of dispersion under unfavourable density contrasts can be found in e.g. Liu and Dane (1996b), Schincariol (1998) and Swartz and Schwartz (1998). Heterogeneity effects for viscous fingering can be found in e.g. Tan and Homsy (1986).

Adopting the conclusions from Welty and Gelhar (1991), Landman, Johannsen and Schotting (2007) and Landman, Schotting, Egorov and Demidov (2007), the temporal evolution of the longitudinal macrodispersion coefficient can be used to infer system stability: *a coefficient that continues to grow with time represents unstable systems while asymptotic coefficients represent stable systems.*

2.2.2 The Balance and State Equations²

The formulations derived in section 2.1.1 can be used to obtain the conservation equations for: fluid mass (2.12), solute mass (2.13) and fluid momentum or the Darcy equation (2.14) where the inertial effects have been neglected. The Darcy equation is in essence a balance between the driving forces due to gravity and pressure gradients

²This section is contained in Musuuza et al. (2009) doi 10.1010/adwatres.2009.01.012

and drag forces exerted by the solid phase on the fluid phase (Pieters 2004).

$$\frac{\partial(\phi\rho(\omega))}{\partial\hat{t}} + \nabla_{\mathbf{X}} \cdot (\rho(\omega)\mathbf{u}) = 0 \quad (2.12)$$

$$\frac{\partial(\phi\rho(\omega)\omega)}{\partial\hat{t}} + \nabla_{\mathbf{X}} \cdot (\rho(\omega)\omega\mathbf{u} - \phi\rho(\omega)\mathbf{D}\nabla_{\mathbf{X}}\omega) = 0 \quad (2.13)$$

$$\mathbf{u} = -\frac{\mathbf{k}}{\mu(\omega)} (\nabla_{\mathbf{X}}p - \rho(\omega)\mathbf{g}). \quad (2.14)$$

In the above equations, ω is the solute mass fraction [-], $\rho(\omega)$ the fluid density [$kg \cdot m^{-3}$], ϕ the porosity [-], \mathbf{D} the diffusion/dispersion tensor [$m^2 \cdot s^{-1}$], \mathbf{u} the Darcy velocity [$m \cdot s^{-1}$], \mathbf{k} the intrinsic permeability tensor [m^2], $\mu(\omega)$ the dynamic viscosity [$Pa \cdot s$], p the pressure [$N \cdot m^{-2}$], \mathbf{X}, \hat{t} the respective space and time variables and \mathbf{g} the gravitational acceleration [$m \cdot s^{-2}$]. The system is defined on $J \times \Omega$ where the domain $\Omega \subset \mathbb{R}^2$ and time $J = (0, T)$ with T the end time. Boundary and initial conditions complete the model.

The coupling through the density $\rho(\omega)$ makes density-driven systems difficult to solve. In fact analytical solutions for coupled systems are only known for simplified situations (Frolkovič and De Schepper 2001). In addition to boundary and initial conditions, state dependencies that describe the relationships $\rho(\omega)$ and $\mu(\omega)$ are required beforehand to close the system.

The available options are *constant* (Fein and Schneider 1999), *linear* (Frind 1982, Coskuner and Bentsen 1990, Holzbecher 1998, Kolditz et al. 1998, Ackerer, Younes and Mose 1999, Fein and Schneider 1999, Held et al. 2005, Bhadauria 2007), *real* (an exponential fit of experimental data) (Manickam and Homsy 1993, Holzbecher 1998, Kolditz et al. 1998, Fein and Schneider 1999, Diersch and Kolditz 2002, Kretz et al. 2003, Talon, Martin, Rakotomalala and Salin 2004, Ghesmat and Azaiez 2007) and *ideal* (derivation based on thermodynamic considerations) (Oldenburg and Pruess 1995, Holzbecher 1998, Fein and Schneider 1999, Johannsen 2002).

To allow for smooth continuity of the work by Held et al. (2005), the linear relation-

ships for density and viscosity were used in this work:

$$\rho(\omega) = \rho_0(1 + \alpha\omega) \quad (2.15)$$

$$\mu(\omega) = \mu_0(1 + \beta\omega) . \quad (2.16)$$

In the above, ρ_0 and μ_0 are the density and viscosity of pure water and α and β the coefficients defining the maximum relative density and viscosity respectively.

Other state dependencies would result in different stability numbers but simulations with linear and ideal implementations showed no significant difference in the fingering patterns.

The Oberbeck-Boussinesq Approximation

The variable-density system of equations is coupled through the dependency of ρ on ω . Its analysis is substantially simplified by applying the Oberbeck-Boussinesq approximation, which neglects all changes in density other than in the buoyancy term $\rho(\omega)\mathbf{g}$ of the Darcy equation (Nield and Bejan 1992, Holzbecher 1998, Diersch and Kolditz 2002, Johannsen 2003). The approximation results in divergence-free velocity ($\nabla \cdot \mathbf{u} = 0$) and incompressibility, which is a common assumption in most analytical and stability analyses. The Oberbeck-Boussinesq approximation remains valid if the density changes remain small compared to the reference density ρ_0 but becomes invalid for large contrasts (Nield and Bejan 1992) when the isobars are no longer orthogonal to the velocity vectors (Held et al. 2005). It was not clear what consequences resulted when full dependencies were incorporated (Diersch and Kolditz 2002). The full equations were implemented in this work and it will be shown that the assumption has a stabilising effect.

2.3 The Current Work and Contributions

This work is an extension to the ideas introduced by Held et al. (2005) that applied homogenization theory to relate mesoscale velocity and solute fluctuations. In this

sense, the approach is similar to local-averaging approaches as used by Chang and Slattery (1988) and similar to other scaling analyses as presented by Coskuner and Bentsen (1990). Pressure, solute concentration and velocity are assumed to be perturbed at the mesoscale. The system behaviour as a response to these small-scale perturbations is studied at the macroscale. A prerequisite for density-driven flow through a homogeneous porous medium to be stable at large spatial or temporal scales is the stability at small scales.

A stability criterion is derived via homogenization theory and the underlying two scale expansions, first for a homogeneous medium without dispersion and then extended to include dispersive and medium heterogeneity effects. The small-scale stability criterion for flow in a homogeneous medium stems from the small-scale evolution of the mass fraction, which has the form $\omega_1(t) = \omega_1(0) \exp(-\Lambda t)$, where $\omega_1(0)$ is the initial small-scale mass fraction, Λ the stability number and t the time. $\omega_1(t)$ decays to zero or grows indefinitely depending on whether Λ (a function of density, viscosity, concentration gradients and the large scale velocity) is negative or positive. Λ will be tested for the effects of density, viscosity and flow velocity in section 3.4 for flow aligned orthogonal to gravity.

The extension to dispersive effects essentially entails the analysis of how the mixing zone controls the spectrum of perturbation wavelengths that can develop into fingers. The dispersive contribution is a function of the perturbation wavelengths, the dispersivities and the characteristic length. A method of perturbing the inflow with sinus functions of different wavelengths will be proposed and presented. The wavelength at which fingering is first observed corresponds to the critical perturbation wavelength.

By following the ideas in Kempers and Haas (1994) and physical constraints, an analytical expression for the mixing zone is derived as a product of dispersivities. The dispersive contribution is then a function of the perturbation wavelength and the dispersivities.

To ease comparison with previous research, the stability number without dispersion was reformulated in form of a Rayleigh number Ra . Unlike previous researches, the

effects of dispersion were taken into account and the characteristic length, taken equal to the mixing zone width was used instead of the entire domain size. These in addition to the smaller density contrasts resulted into significantly smaller Ra than the traditional 400 widely reported in literature. However, the phenomena observed previously could still be reproduced.

As an example, the transition in the number of fingers documented in Johannsen (2002) was correlated with the three regimes in Diersch and Kolditz (2002). The two concepts were then extended to stability studies as explained in the following.

Upon reformulating the stability number Λ_p in terms of Ra and adding the dispersive part, a new number Λ_p^* was obtained. Λ_p^* was then used to predict stability according to the number of fingers present. Systems with one finger arise at small Ra (density contrasts) when transport is predominantly diffusive. The absence of convection means the systems are physically stable and are predicted with $\Lambda_p^* > 0$. Gradual increase in density contrast causes convection cells to develop. The cells result in the formation of two fingers and from the criterion $\Lambda_p^* < 0$. The change in sign of the stability number therefore predicts the onset of convection i.e. the change from one to two fingers. The system is however still in the stable convective regime (Diersch and Kolditz 2002).

Further increase in the density contrast reduces the stability number further. Increased density contrast leads to more convection cells (Frolkovič and De Schepper 2001) whose erratic interactions lead to the formation of further fingers (Frolkovič and De Schepper 2001). The formation of additional fingers marks the transition into the unstable convective regime. Diersch and Kolditz (2002) explain that the regime is characterised by many transient solutions that do not persist in time. However, the stability criterion does not predict a definite number where the transition occurs but rather a range.

Figure 2.5 summarises the three flow regimes from Diersch and Kolditz (2002) and the increase of Ra with density contrast (Diersch and Kolditz 2002, Johannsen 2002).

Those ideas were combined in this work whereby the computed stability number

Ra, Elder	0	$4\pi^2$	240-300
Regime	Diffusive	Stable convective	Unstable convective
Fingers	1	2	3
Λ_p^*	$\Lambda_p^* > 0$	$\Lambda_p^* < 0$	

Fig. 2.5 Demarcation of the flow regimes by the stability criterion

could be used to infer the number of fingers (prediction of flow regime) as shown in Fig. 2.6. The main interest was on the transition from two to three fingers: the onset

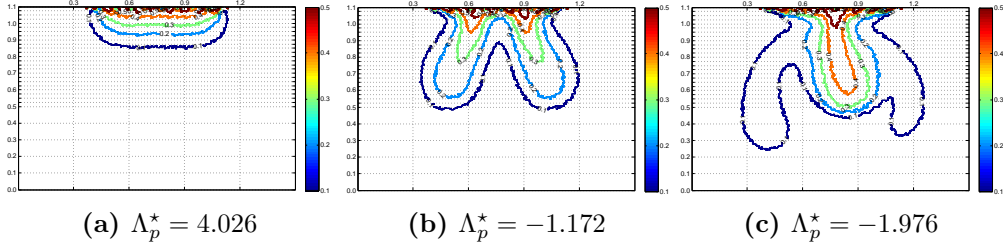


Fig. 2.6 The relation between Λ_p^* and the number of fingers

of the unstable convective regime. Stability is in the physical sense rather than the purely mathematical. We look at finger formation and development primarily as a consequence of changes in physical variables.

The expression for Λ_p^* was modified to accommodate heterogeneity effects. Mixing from heterogeneities increases the dispersivities against their local values. The effective heterogeneous-medium dispersivity is expressed in terms of the local homogeneous medium value α and the change $\delta(\alpha)$ induced by the heterogeneous medium: $\alpha^{\text{eff}} = \alpha + \delta(\alpha)$. The effective values are substituted into the previously derived criterion and the products evaluated with the products of $\delta(\alpha)$ terms neglected in consistency with the linear perturbation theory used elsewhere in this work.

One then obtains a new stability number Λ_p^{**} in terms of the previous Λ_p^* and an additional term which is a function of the longitudinal dispersivity in heterogeneous media. That dispersivity has been shown in e.g. Gelhar (1993) to be the product of the heterogeneity variance σ^2 and the correlation length λ_v . The final expression has the ratio $\sigma^2 : \lambda_v$ thus capturing the respective stabilising and destabilising effects of variance and correlation length that can be confirmed in numerical simulations. From the previous discussion a change in the number of fingers can be used to

indicate the direction of stability transition.

The reduction in the number of fingers with variables that cause stabilisation of systems was revisited. It will be shown that increasing the variance always leads to a reduction in the number of fingers while increasing the correlation length beyond a certain value eventually leads to the formation of the third finger. The cutoff correlation length appeared to be related to the critical perturbation wavelength that was obtained for the homogeneous medium.

The expression for Λ_p^{**} is valid under conditions of complete mixing at the small scale. If those conditions are not met, one has to study large-scale mixing by computing macrodispersion coefficients.

The large-scale transport equation (derived via homogenization theory and containing the macrodispersion tensor) (Held et al. 2005) was used to study mixing effects in heterogeneous media. The individual tensor elements initially evaluated to functions containing diffusion and averaged products of the solution to the cell problem (generalised small-scale equation) and the mesoscale velocity fluctuations. The solutions to the cell problem were expressed as definite time integrals. The mesoscale velocity was split into contributions from the fluctuations in the solute and medium heterogeneity, whose separate derivations are presented in Appendices A.1 and A.2.

Carrying out the averaging operations on the tensor elements was essentially the evaluation of integrals over the entire space and finite times. By expressing the respective terms as Gaussian functions and neglecting molecular diffusion, the integrals could be conveniently evaluated with the software **MAPLE**[®]: analytically over time and then completely by numerical techniques. The evaluation gave a symmetric tensor with zero off-diagonal elements, while the leading diagonal elements were functions of time and depicted the scale dependency mentioned in the preceding sections.

Passive tracers were “emulated” by setting the density and viscosity effects to zero and the trends in the computed coefficients were found to agree with those in literature. Favourable density contrasts were then investigated by arbitrarily choosing

positive stability numbers and studying the trend in the coefficients. Much as these scenarios were not of much interest, the following temporal evolutions of the coefficients were obtained: the longitudinal and transverse coefficients respectively decreased and increased asymptotically with increasing stability numbers. This meant that variables that stabilise like the heterogeneity variance were expected to produce a reduction in the longitudinal coefficient.

From the foregoing, the longitudinal coefficient increased with system instability. It will be shown that for moderately unfavourable density contrasts (negative stability numbers), asymptotic longitudinal coefficients could still be obtained. This physically indicated the range of unfavourable density contrasts that were stabilised by medium heterogeneity. With further increase in the density contrast, coefficients that grew indefinitely with time were obtained, which was consistent with the conclusions from previous researchers. Additionally, increasing the correlation length resulted in increased longitudinal coefficients, hence a reduction in system stability, while the reverse was true for the heterogeneity variance.

The foregoing discussion pertained to isotropic media. By defining the anisotropy ratio as $\xi = \lambda_h : \lambda_v$, longitudinal coefficients that reduced with the anisotropy ratio were obtained, which was consistent with physical expectations. However, ξ is not incorporated in the stability criterion.

In summary, homogenization theory was used to develop equations from which a stability criterion for density-driven systems was derived. The criterion quantifies the effects of density, viscosity, dispersion and medium heterogeneity. The criterion adequately predicted the stability transition for systems aligned orthogonal to gravity but also predicted the onset of convection in vertical systems. Previous results about the number of fingers and flow regimes were extended to study stability. The usual notion of unconditional instability of Elder-type systems was found not to be entirely true.

This work also answered the question regarding when medium heterogeneity stabilised or destabilised systems. Heterogeneities stabilise at large heterogeneity variances, small correlation lengths, and high medium anisotropies. The investigations

also revealed that the critical wavelengths in homogeneous medium and the heterogeneity correlation length do not have a one-to-one relation.

2.3.1 Overview of the Homogenization Theory

The homogenization theory is briefly presented in this section. The link between homogenization and stability studies is also developed and presented here. To analyse the stability of a flow pattern, one essentially analyses the temporal evolution of the small-scale interactions of the solute with the flow field and porous medium. Due to the strong coupling between fluid flow and solute transport, perturbations in the salt mass cause fluctuations in the flow field which may couple back and amplify or damp the salt mass fluctuations.

Homogenization theory is a two-scale expansion technique designed to quantify the impact of small perturbations on the large-scale behaviour of a system. This work proposes to employ homogenization techniques to derive equations that describe the large-scale density-driven flow and transport behaviour and to give an indication of the system's response to small-scale perturbations in the salt mass fraction. The presentation here is very basic and reference to standard textbooks like Hornung (1996), Cioranescu and Donato (1999) and Pavliotis and Stuart (2007) is recommended for details.

Two spatial scales are considered: the large scale L at which the processes are observed and the mesoscale l related to small-scale fluctuations in the properties. To do the analysis, two dimensionless spatial variables \mathbf{x} and \mathbf{y} are introduced such that $\mathbf{x} = \mathbf{X}/L$ and $\mathbf{y} = \mathbf{X}/l$, where \mathbf{X} is the unscaled spatial variable. The ratio between the two scales is further defined as $\epsilon = l/L$, leading to $\mathbf{y} = \mathbf{x}/\epsilon$. All spatially varying quantities (\mathbf{u}, p, ω) vary on \mathbf{x} and \mathbf{y} . Taking limits as $\epsilon \rightarrow 0$ and performing an asymptotic analysis enables the derivation of the small- and large-scale (homogenized) equations (Lunati, Attinger and Kinzelbach 2002, Held et al. 2005). The proofs of existence and uniqueness of solutions to the partial differential equations derived in that limit make homogenization theory superior to volume

averaging.

If D_{\parallel} and D_{\perp} are the respective longitudinal and transverse components of the diffusion/dispersion tensor, the tensor in two dimensions is usually written:

$$\mathbf{D} = \begin{pmatrix} D_{\parallel} & 0 \\ 0 & D_{\perp} \end{pmatrix} ,$$

with $D_{\perp}/D_{\parallel} \ll 1$. By scaling diffusively two dimensionless temporal variables are introduced: $t = D_{\parallel}\hat{t}/L^2$ and $\tau = D_{\parallel}\hat{t}/l^2$ corresponding to the macro- and meso-length scales respectively, where \hat{t} is the unscaled time. It follows that $\tau = t/\epsilon^2$. Using the chain rule of differentiation one obtains:

$$\nabla_{\mathbf{x}} = \frac{1}{L} \left(\nabla_{\mathbf{x}} + \frac{1}{\epsilon} \nabla_{\mathbf{y}} \right) , \quad (2.17)$$

$$\frac{\partial}{\partial \hat{t}} = \frac{D_{\parallel}}{L^2} \left(\frac{\partial}{\partial t} + \frac{1}{\epsilon^2} \frac{\partial}{\partial \tau} \right) . \quad (2.18)$$

The two equations express the space and time derivatives in the respective 2-scale dimensionless variables. In the subsequent, $\nabla_{\mathbf{x}}$ is written without the subscript to shorten the notation and the assumption of well-separated scales is used such that $L \gg l$ so that $\epsilon \ll 1$.

The 2-scale mass fraction variation, denoted by the ϵ superscript can be written as an asymptotic expansion in powers of ϵ (Auriault 2002, Lunati et al. 2002, Held et al. 2005):

$$\omega^{\epsilon}(\mathbf{x}, \mathbf{y}, t, \tau) = \omega_0(\mathbf{x}, t) + \epsilon \omega_1(\mathbf{x}, \mathbf{y}, t, \tau) + O(\epsilon^2) , \quad (2.19)$$

where $\omega_0(\mathbf{x}, t)$ is the large-scale mass fraction and the ϵ superscript indicates the variations on 2-scales. The function $\omega_1(\mathbf{x}, \mathbf{y}, t, \tau)$ is assumed to be periodic (of period $\mathbf{1}$) in the second variable. The homogenization of the transport equation will be presented in this work to derive the macrodispersion tensor. Homogenization of the pressure equation for the homogenized permeability tensor can be found in Held et al. (2005). To that end, the ω in (2.13) is expanded according to (2.19); and (2.17) and (2.18) applied to the respective derivatives to yield an equation containing terms with different powers of ϵ :

$$(\dots)\epsilon^{-2} + (\dots)\epsilon^{-1} + (\dots)\epsilon^0 = f \quad , \quad (2.20)$$

where f contains the source/sink terms if present. By letting $\epsilon \rightarrow 0$ and collecting terms with the same orders of ϵ , one obtains the following three equations:

- i) ϵ^{-2} : the compatibility condition stating the independency of large-scale solutions from small scales
- ii) ϵ^{-1} : the small-scale equation describing the variation of the quantity of interest at the mesoscale
- iii) ϵ^0 : the large-scale equation containing the homogenized tensor as a function of small-scale variations. Depending on whether homogenization theory is applied to the pressure, solute transport or heat transport equation, the homogenized permeability, macrodispersion or thermal diffusivity tensor results.

The coefficients of ϵ^{-2} and ϵ^{-1} must vanish to zero to avoid division by zero. A detailed application of the procedure to the transport equation is presented in section 3.1.

2.3.2 Overview of the d^3f Program

The program package d^3f (Fein and Schneider 1999) was used for the numerical simulations in this work. The program consists of three major parts (Johannsen et al. 2002): the *preprocessor* that designs the geometry and defines physical parameters interactively; the *simulator* that generates the grid and solves the variable-density system and the *postprocessor* that supports data extraction and visualisation.

The simulator is based on the UG software package (Bastian, Birken, Johannsen, Lang, Neuss and Rentz-Reichert 1997). The domain is discretised by means of unstructured meshes consisting of quadrilaterals in two dimensions. A fully implicit/fully coupled solution technique for the cell-centred finite volume discretisation with consistent velocity approximation is implemented (Johannsen et al. 2002).

The following is a brief description of the discretisation techniques for the respective derivatives in the flow and transport equations.

The Spatial Discretisation

The code uses the cell-centred finite volume technique for the spatial discretisation with continuous piecewise trilinear trial functions (Johannsen et al. 2002). Figure 2.7 shows a simplified construction for quadrilateral elements in 2-D. Mesh generation is furnished by connecting the midpoints x_{ij} of the quadrilateral element edge between nodes x_i and x_j with x^e , the centroid of the elements e . The line segment Γ_{ij}^e is then obtained while boundary segments Γ_{jk}^b are obtained by connecting the nodes and the midpoints of boundary edges (Frolkovič 1998a). It must be ensured that inner nodes are presented first followed by boundary nodes (Knabner 2003). The volume V_i is defined as the polygon enclosing discretisation node i . The cell-centred

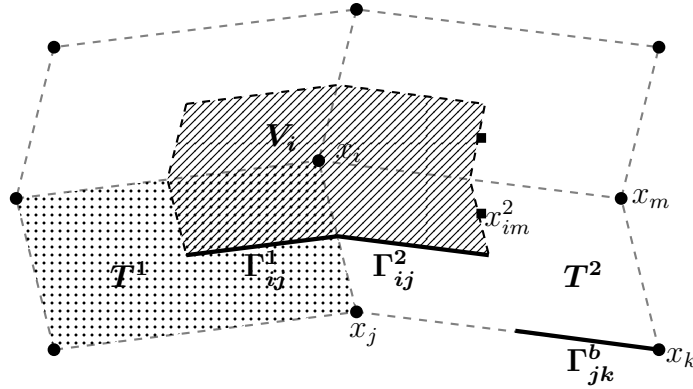


Fig. 2.7 Construction of the cell-centred finite volume elements

finite volume technique is locally mass-conserving (Frolkovič 1998b, Leveque 2002) and second-order consistent for the unknowns p and ω (Johannsen et al. 2002). The approximated solution changes only due to the boundary conditions (Reeves and Ewiera 2000).

The Temporal Discretisation

The implicit Euler method is used for the discretisation of the time derivatives:

$$\frac{\partial \omega}{\partial t} \approx \frac{\omega^m - \omega^{m-1}}{\tau^m} . \quad (2.21)$$

$\omega^m = \omega(t^m)$ denotes the mass fraction at any discrete time. The time is such that $0 = t^0 < t^1 < \dots < t^m < t^{m+1} < \dots$, with the time step denoted by $\tau^m = t^m - t^{m-1}$, which need not be uniform (Frolkovič 1998a). An equation similar to (2.21) can analogously be written for the pressure.

The Numerical Solution Strategy

Let for each time step t^m and grid node x_i the unknown mass fraction and pressure are associated with the respective approximate values: $\omega_i^m \approx \omega(x_i, t^m)$ and $p_i^m \approx p(x_i, t^m)$. A nonlinear system of algebraic equations can be derived of the form (Frolkovič 1998a)

$$F^m(\dots, \omega_i^m, \dots, p_i^m, \omega_i^{m-1}, \dots, p_i^{m-1}, \dots) = 0 . \quad (2.22)$$

Typically the nodal values are solved by using the respective known values from previous time steps with values at $m = 0$ given by the initial and boundary conditions. To have a solution that is defined for each point in the domain at all times, the nodal values need to be interpolated using the finite element techniques (Leveque 2002). The Galerkin Finite Element Method is implemented in the d^3f program. Please see Frolkovič (1998a) for more specific details while general discretisation techniques and solutions to partial differential equations can be found in standard textbooks on the subject like Knabner (2003).

Implementation of a BVP in d^3f

The program package offers the possibility to implement problems using either the graphical user interface GUI or script files. In the following, implementation using

script files will be described. After a successful compilation of the module, the simulator is started by invoking the `tstep` script. For successful execution, the subdirectories `config`, `data`, `logfiles`, `metas` and `scripts` must exist and reside in the path where the script is invoked. Their contents are briefly described now.

scripts This folder contains the script `init.scr` that controls the simulation. Whether to create a new grid or use an existing one, use full equations or invoke the Boussinesq approximation, the level of grid refinement, the time stepping, the end time, upwind technique, the treatment of diffusion, type of smoother, the linear, nonlinear and multi-grid solvers, the heap allocation and output-control parameters are all set there. One has the choice to output the pressure, velocity and concentration to the `screen`, `ppm`, `ps`, `bwps` and `meta` devices. The generated mesh is written in the `xdr` file format (see Bastian et al. (1997)) and can be viewed with the `GRAPE` application. When saved, the `meta` files can be used to make a video by specifying the start and end files as well as the interval. Other parameters offer total control over frame translation.

data This contains the mesh generation files named `mesh.xx.gn` giving access to the grid levels and the multigrid file `mg.ug.mg.xdr`. When the parameter in the `init.scr` file is set to generate a new grid, these files are overwritten, otherwise the existing ones are used.

logfiles This is where the output from the simulator is written in the file `logfile` but is also printed on the screen. Among the logged items are the properties of the created grid: at each level of refinement the number of vertices, nodes, edges, elements, sides, connections and the minimum and maximum edges. The amount of memory used from the allocated heap is also printed. Errors are also reported if encountered.

At each time step, the pressure and mass fraction solutions, the Nusselt, Péclet and Courant numbers, the times required to solve the defect, Jacobi and linear matrices as well as the total time, time step and the number of iterations for the linear and nonlinear solvers are also logged.

config The 5 configuration files reside here. The **hydrogeology** file contains data about the physical properties of the liquid phase, the state dependencies and the number and properties of the hydrogeological units. The file **geometry** contains the geometrical description of all the units named in **hydrogeology**. In 2-D, the points defining line segments and the lines segments describing polygons have to be given in a chronological order to ensure closure. The file **boundary** contains data regarding the boundary conditions for the flow and transport equations. It is possible to define either time-dependent or independent boundary conditions.

The files **source** and **initial** provide information regarding the location of sources and sinks and initial conditions respectively.

metas The graphic outputs are saved in this directory.

It is possible to implement boundary conditions, permeability distributions, etc as functions defined in the file `$d3fROOT/df/gen/problems/lgm_funcs.c`. If additional functions are required, they should be defined in that file and the module recompiled.

There is also a possibility to have the solution vectors for pressure, velocity and mass fraction as well as the generated permeability field along with the grid coordinates written as matrices in text files. That is particularly important when one requires to use an external program like **MATLAB**[®] that provide superior visualisation capabilities to the default postprocessor.

In that case, one writes a c-file containing numerical procedure macros that create, initialise and execute the vector-writing function, places the file in the path `$UGROOT/np` and adapts the **makefile** in that directory to build the required objective. Additionally, the three numerical procedures have to be called in the file `$UGROOT/pm/df.pm`. The function is finally called in the **tstep** script, as often as required and the path where the files should be written specified. A recompilation of the module is again required to make the new functions available.

The output graphic files specified in the **init.scr** file are saved by the simulator at every time step. After long simulation times, quite big storage is used up. The

default behaviour can be modified by specifying in the `tstep` script the number of computation time steps after which data is to be saved.

This work expanded the functionality of the program by defining the sinus boundary condition function and saving the solutions in every point at every time step.

2.3.3 Model Set-up and Simulation Parameters

This section gives the model set-ups and simulation parameters used in the stability studies. Two configurations will be considered: the *horizontal* in which the solute enters at the side of the domain and the *vertical* system in which the solute travels downwards under the action of gravity. The two occur in practice in saltwater intrusion into coastal aquifers and at the vicinity of waste repositories respectively.

The Horizontal Flow System

The initial stability criterion for the homogeneous medium was tested on the problem defined in Schincariol et al. (1997), which was itself based on experimental results documented in Schincariol and Schwartz (1990). Figure 2.8 shows the problem setup in which water flowed from left to right. Pressure heads were maintained across the domain to achieve an initial velocity of $2.75 \times 10^{-6} m/s$.

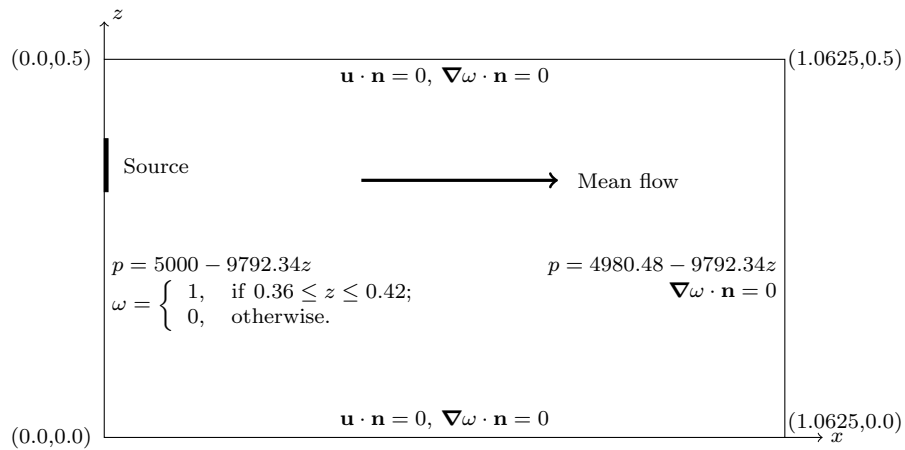


Fig. 2.8 Model set-up for the orthogonal system

The Vertical Flow System

A vertical setup shown in Fig. 2.9 was used to study dispersive and heterogeneity effects. The domain was increased to allow the salt more time and also achieve a Rayleigh number of 300 computed in the traditional way, at which some solutions in Johannsen (2002) showed three fingers. The sinus function in the figure

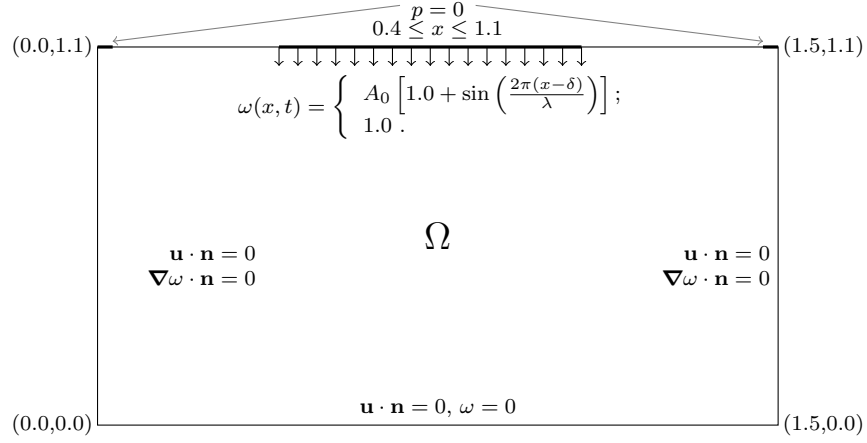


Fig. 2.9 Model set-up for vertical systems

was required to initiate perturbations in the homogeneous medium. The medium heterogeneities initiate perturbations in heterogeneous media, hence the constant boundary condition.

Simulation Parameters

The simulation parameters, also adopted from Schincariol et al. (1997) are shown in Table 2.1. The same were used for the vertical systems apart from the maximal density was reduced to ensure moderate fingering. The starred domain size and the longitudinal and transverse dispersion lengths were also changed from the values used in Schincariol et al. (1997).

Table 2.1 Simulation parameters

Parameter	Notation	Value	Unit
Porosity	n	0.38	–
Molecular diffusion coefficient of NaCl	D_m	1.61×10^{-9}	$m^2 \cdot s^{-1}$
Longitudinal dispersivity	α_{\parallel}	1.0×10^{-3}	m
Transverse dispersivity	α_{\perp}	2.0×10^{-4}	m
Domain Length in flow direction	L	1.0625	m
Viscosity of pure water at $20^{\circ}C$	μ_0	1.002×10^{-3}	$Pa \cdot s$
Density of pure water at $20^{\circ}C$	ρ_0	998.2	$kg \cdot m^{-3}$
Maximal density of solution (2000mg/l NaCl at $20^{\circ}C$)	ρ_{max}	999.7	$kg \cdot m^{-3}$
Gravity vector	\mathbf{g}	-9.81	$m \cdot s^{-2}$
Maximal density of NaCl at $20^{\circ}C^*$	ρ_{max}	998.5	$kg \cdot m^{-3}$
Longitudinal dispersivity*	α_{\parallel}	1.5×10^{-3}	m
Transverse dispersivity*	α_{\perp}	1.0×10^{-4}	m
Domain Length in flow direction*	L	1.1	m
Vertical correlation length	λ_v	0.0075	m
Horizontal correlation length	λ_h	0.0075	m
Permeability	$k\mathbf{I}_2$	$5.7 \times 10^{-11}\mathbf{I}_2$	m^2
Heterogeneity variance	σ^2	0.60	–

* values used for the vertical configuration.

Chapter 3

Stability Analyses for a Homogeneous Medium¹

In this chapter the homogenization theory ideas are applied to the solute transport equation. Following the procedure outlined in section 2.3.1, three equations result namely the *compatibility condition*, which is a statement of the independency of macroscopic quantities from small scales and the *small-* and *large-scale* equations. The small-scale equation expresses the variations of the solute at the mesoscale and will be used to derive the stability criterion: first for a homogeneous medium without dispersion and subsequently extended to include the dispersive and heterogeneity effects.

The large-scale equation contains the homogenized macrodispersion tensor. The equation will be used to derive the entries in the tensor. The temporal evolution of the tensor elements will be studied in detail in response to changes in several physical variables.

¹Published in Musuuza et al. (2009) doi 10.1010/adwatres.2009.01.012

3.1 Homogenization of the Transport Equation

In this section we derive the equations mentioned in the preceeding section. We proceed by substituting the 2-scale expansion for the mass fraction

$$\omega^\epsilon(\mathbf{x}, \mathbf{y}, t, \tau) = \omega_0(\mathbf{x}, t) + \epsilon\omega_1(\mathbf{x}, \mathbf{y}, t, \tau) + O(\epsilon^2)$$

into the solute transport equation

$$\frac{\partial(\phi\rho(\omega)\omega)}{\partial\hat{t}} + \nabla_{\mathbf{x}} \cdot (\rho(\omega)\omega\mathbf{u} - \phi\rho(\omega)\mathbf{D}\nabla_{\mathbf{x}}\omega) = 0 \quad .$$

We then apply the respective 2-scale expansions for the derivatives in space

$$\nabla_{\mathbf{x}} = \frac{1}{L} \left(\nabla_{\mathbf{x}} + \frac{1}{\epsilon} \nabla_{\mathbf{y}} \right)$$

and time

$$\frac{\partial}{\partial\hat{t}} = \frac{D_{\parallel}}{L^2} \left(\frac{\partial}{\partial t} + \frac{1}{\epsilon^2} \frac{\partial}{\partial\tau} \right)$$

to the appropriate terms in the transport equation.

It is necessary to additionally assume steady states and neglect the medium specific storativity: $\partial(\phi\rho(\omega))/\partial\hat{t} = 0$. By using the fluid flow equation

$$\frac{\partial(\phi\rho(\omega))}{\partial\hat{t}} + \nabla_{\mathbf{x}} \cdot (\rho(\omega)\mathbf{u}) = 0$$

one also obtains the incompressibility condition $\nabla \cdot (\rho(\omega)\mathbf{u}) = 0$. The Darcy flux $\rho(\omega)\mathbf{u}$ is therefore divergence-free. Using these in the transport equation (2.13) and writing $\mathbf{v}^\epsilon = \rho(\omega)\mathbf{u}/\phi$ for the linear momentum of the flow, which we call the modified two-scale groundwater velocity, one obtains:

$$\rho(\omega) \frac{\partial\omega^\epsilon}{\partial\hat{t}} + \mathbf{v}^\epsilon \cdot \nabla\omega^\epsilon - \nabla \cdot (\rho(\omega)\mathbf{D}\nabla\omega^\epsilon) = 0 \quad . \tag{3.1}$$

The velocity \mathbf{v}^ϵ is split into the mean \mathbf{v}_0 and fluctuation $\tilde{\mathbf{v}}$ according to:

$$\mathbf{v}^\epsilon = \mathbf{v}_0 + \tilde{\mathbf{v}} . \quad (3.2)$$

Scaling of velocity that shows a non-vanishing mean drift into two scales is complicated by its interactions with the two-scale mass fraction, precisely because the time scales associated with advective and diffusive processes are different (Pavliotis 2002). According to Lunati et al. (2002), if time is scaled diffusively, there are three parts in the advective term of the two-scale transport equation:

- i) the large scale concentration gradient times the mean drift
- ii) the large scale concentration gradient times local variations in the velocity field
- iii) the small scale concentration gradient times the total drift.

Only the first term is a purely macroscopic quantity whereas the last two are not and are thus multiplied with $1/\epsilon$, as shown and explained in Lunati et al. (2002). It is possible to employ a different scaling technique in which the transport equation is written in terms of the large- and small-scale Péclet numbers (see e.g. Pavliotis (2002)). The method however leads to different results.

The accumulation, advective and dispersive terms of (3.1) are considered separately in the following. The two-scale expansion for the mass fraction and the expressions for the space and time derivatives on page 40 are then used.

The accumulation term $\rho(\omega) \frac{\partial \omega^\epsilon}{\partial \hat{t}}$.

$$\rho(\omega) \frac{\partial \omega^\epsilon}{\partial \hat{t}} = \frac{\rho(\omega) D_{\parallel}}{L^2} \left(\frac{\partial \omega_0}{\partial t} + \epsilon \frac{\partial \omega_1}{\partial t} + \frac{1}{\epsilon^2} \frac{\partial \omega_0}{\partial \tau} + \frac{1}{\epsilon} \frac{\partial \omega_1}{\partial \tau} \right) + O(\epsilon) . \quad (3.3)$$

The advective term $\mathbf{v}^\epsilon \cdot \nabla \omega^\epsilon$.

$$\begin{aligned}
\mathbf{v}^\epsilon \cdot \nabla \omega^\epsilon &= \frac{1}{L} \left(\mathbf{v}_0 + \frac{1}{\epsilon} \tilde{\mathbf{v}} \right) \cdot \nabla_{\mathbf{x}} \omega^\epsilon + \frac{1}{L} \left(\frac{1}{\epsilon} \mathbf{v}_0 + \frac{1}{\epsilon} \tilde{\mathbf{v}} \right) \cdot \frac{1}{\epsilon} \nabla_{\mathbf{y}} \omega^\epsilon + O(\epsilon) \\
&= \frac{1}{L} \left(\mathbf{v}_0 + \frac{1}{\epsilon} \tilde{\mathbf{v}} \right) \cdot (\nabla_{\mathbf{x}} \omega_0 + \epsilon \nabla_{\mathbf{x}} \omega_1) \\
&\quad + \frac{1}{L\epsilon^2} (\mathbf{v}_0 + \tilde{\mathbf{v}}) \cdot (\nabla_{\mathbf{y}} \omega_0 + \epsilon \nabla_{\mathbf{y}} \omega_1) + O(\epsilon) .
\end{aligned} \tag{3.4}$$

The expansion techniques from Lunati et al. (2002) that were briefly explained above have been used to obtain (3.4).

The diffusive/dispersive term $\nabla \cdot \mathbf{D} \nabla \omega^\epsilon$.

$$\begin{aligned}
\nabla \cdot \rho(\omega) \mathbf{D} \nabla \omega^\epsilon &= \frac{1}{L^2} \nabla_{\mathbf{x}} \cdot \rho(\omega) \mathbf{D} \left(\nabla_{\mathbf{x}} \omega_0 + \epsilon \nabla_{\mathbf{x}} \omega_1 + \frac{1}{\epsilon} \nabla_{\mathbf{y}} \omega_0 + \nabla_{\mathbf{y}} \omega_1 \right) \\
&\quad + \frac{1}{L^2} \frac{1}{\epsilon} \nabla_{\mathbf{y}} \cdot \rho(\omega) \mathbf{D} \left(\nabla_{\mathbf{x}} \omega_0 + \frac{1}{\epsilon} \nabla_{\mathbf{y}} \omega_0 + \epsilon \nabla_{\mathbf{x}} \omega_1 + \nabla_{\mathbf{y}} \omega_1 \right) + O(\epsilon) \\
&= \frac{1}{L^2} \nabla_{\mathbf{x}} \cdot \rho(\omega) \mathbf{D} \left(\nabla_{\mathbf{x}} \omega_0 + \nabla_{\mathbf{y}} \omega_1 + \frac{1}{\epsilon} \nabla_{\mathbf{y}} \omega_0 \right) \\
&\quad + \frac{1}{L^2} \frac{1}{\epsilon} \nabla_{\mathbf{y}} \cdot \rho(\omega) \mathbf{D} \left(\frac{1}{\epsilon} \nabla_{\mathbf{y}} \omega_0 + \nabla_{\mathbf{y}} \omega_1 + \nabla_{\mathbf{x}} \omega_0 + \epsilon \nabla_{\mathbf{x}} \omega_1 \right) .
\end{aligned} \tag{3.5}$$

To shorten the notation, \mathbf{v}^ϵ and ω^ϵ are subsequently written without the ϵ superscript. Terms from (3.3), (3.4) and (3.5) having the same powers of ϵ are now collected and divided through by D_{\parallel}/L^2 .

Terms in ϵ^{-2} .

$$\rho(\omega) \frac{\partial \omega_0}{\partial \tau} + \frac{L}{D_{\parallel}} (\mathbf{v}_0 + \tilde{\mathbf{v}}) \cdot \nabla_{\mathbf{y}} \omega_0 - \nabla_{\mathbf{y}} \cdot \mathbf{D}^* \nabla_{\mathbf{y}} \omega_0 = 0 , \tag{3.6}$$

where $\mathbf{D}^* = \rho(\omega) \mathbf{D} / D_{\parallel}$. The relation (3.6) evidently satisfies the compatibility condition due to $\partial \omega_0 / \partial \tau = 0$ and $\nabla_{\mathbf{y}} \omega_0 = 0$: the large scale solution is independent of small scales (i.e. $\omega_0 = \omega_0(\mathbf{x}, t)$).

Terms in ϵ^{-1} .

$$\rho(\omega) \frac{\partial \omega_1}{\partial \tau} + \frac{L}{D_{\parallel}} \tilde{\mathbf{v}} \cdot \nabla_{\mathbf{x}} \omega_0 + \frac{L}{D_{\parallel}} (\mathbf{v}_0 + \tilde{\mathbf{v}}) \cdot \nabla_{\mathbf{y}} \omega_1 - \nabla_{\mathbf{y}} \cdot \mathbf{D}^* \nabla_{\mathbf{x}} \omega_0 - \nabla_{\mathbf{y}} \cdot \mathbf{D}^* \nabla_{\mathbf{y}} \omega_1 = 0 \quad .$$

The term $\nabla_{\mathbf{y}} \cdot \mathbf{D}^* \nabla_{\mathbf{x}} \omega_0$ drops out because $\omega_0 = \omega_0(\mathbf{x}, t)$ to give

$$\rho(\omega) \frac{\partial \omega_1}{\partial \tau} + \frac{L}{D_{\parallel}} \mathbf{v} \cdot \nabla_{\mathbf{y}} \omega_1 + \frac{L}{D_{\parallel}} \tilde{\mathbf{v}} \cdot \nabla_{\mathbf{x}} \omega_0 - \nabla_{\mathbf{y}} \cdot \mathbf{D}^* \nabla_{\mathbf{y}} \omega_1 = 0 \quad . \quad (3.7)$$

Equation (3.7) relates the small-scale rate of change of mass fraction to velocity fluctuations: the link between homogenization theory and stability. This relation will be used to derive the stability criterion for a homogeneous medium in chapters 3 and 4 and for a heterogeneous medium in chapter 5. It requires homogeneous Dirichlet boundary conditions.

Terms in ϵ^0 .

$$\rho(\omega) \frac{\partial \omega_0}{\partial t} + \frac{L}{D_{\parallel}} \mathbf{v}_0 \cdot \nabla_{\mathbf{x}} \omega_0 + \frac{L}{D_{\parallel}} \tilde{\mathbf{v}} \cdot \nabla_{\mathbf{x}} \omega_1 - \nabla_{\mathbf{x}} \cdot \mathbf{D}^* \nabla_{\mathbf{x}} \omega_0 - \nabla_{\mathbf{x}} \cdot \mathbf{D}^* \nabla_{\mathbf{y}} \omega_1 - \nabla_{\mathbf{y}} \cdot \mathbf{D}^* \nabla_{\mathbf{x}} \omega_1 = 0 \quad (3.8)$$

When present, sink and source terms appear in the right hand side. From (3.8) the large-scale transport equation is sought, whose solution is $\omega_0(\mathbf{x}, t)$. To do this one has to first solve (3.7) for ω_1 (depends on ω_0). Following Held et al. (2005), assume a solution of the form $\omega_1 = \chi^{\omega} \cdot \nabla_{\mathbf{x}} \omega_0$. By introducing this in (3.7), one obtains a cell problem which has to be solved for $\chi^{\omega}(\tau, \mathbf{y})$, together with periodic or homogeneous Dirichlet boundary conditions on $Y = [0, 1]^d$ (eventually rescaled), with d the number of spatial dimensions. The cell problem is given explicitly in chapter 5 where it is used to derive the elements of the macrodispersion tensor. Now, by integrating (3.8) with respect to the variable \mathbf{y} over the cell domain Y , the last two terms drop out because of the $\mathbf{1}$ -periodicity of ω_1 to yield:

$$\rho(\omega) \frac{\partial \omega_0}{\partial t} + \frac{L}{D_{\parallel}} \mathbf{v}_0 \cdot \nabla_{\mathbf{x}} \omega_0 - \nabla_{\mathbf{x}} \cdot \mathbf{D}^* \nabla_{\mathbf{x}} \omega_0 + \frac{L}{D_{\parallel}} \nabla_{\mathbf{x}} \cdot \overline{\tilde{\mathbf{v}} \otimes \chi^{\omega}} \nabla_{\mathbf{x}} \omega_0 = 0 \quad , \quad (3.9)$$

where generally $\bar{f} = \int_Y f(\mathbf{y}) d\mathbf{y}$. The divergence-free velocity assumption has also been used. The integration is actually an averaging of that function over the mesoscale. Further, by defining the macrodispersion tensor $\mathbf{D}^{\text{eff}} = \mathbf{D}^* - \frac{L}{D_{\parallel}} \tilde{\mathbf{v}} \otimes \overline{\boldsymbol{\chi}^\omega}$, (3.9) can be written as

$$\rho(\omega) \frac{\partial \omega_0}{\partial t} + \frac{L}{D_{\parallel}} \mathbf{v}_0 \cdot \nabla_{\mathbf{x}} \omega_0 - \nabla_{\mathbf{x}} \cdot \mathbf{D}^{\text{eff}} \nabla_{\mathbf{x}} \omega_0 = 0 \quad , \quad (3.10)$$

which is the macroscale equation for the mass fraction. The entries of the macrodispersion tensor in 2-dimensions ($d = 2$) can be evaluated explicitly as

$$\mathbf{D}^{\text{eff}} = \begin{pmatrix} \rho - \frac{L}{D_{\parallel}} \overline{\tilde{v}_1 \chi_1^\omega} & -\frac{L}{D_{\parallel}} \overline{\tilde{v}_1 \chi_2^\omega} \\ -\frac{L}{D_{\parallel}} \overline{\tilde{v}_2 \chi_1^\omega} & \rho \frac{D_{\perp}}{D_{\parallel}} - \frac{L}{D_{\parallel}} \overline{\tilde{v}_2 \chi_2^\omega} \end{pmatrix} . \quad (3.11)$$

The macrodispersion tensor relates the small-scale velocity fluctuations to large-scale mixing effects. This relation will be used to derive formulations for the mixing coefficients in heterogeneous media in section 5.3.

Making use of homogenization theory one expects to see the impact of small scale instabilities on the

small scale: in homogenization theory, large-scale parameters are usually evaluated by first solving the so called auxiliary equations (3.7) defined on the small scale. These solutions are then inserted in and averaged over formulas for the large scale parameters. If these auxiliary equations show unstable behaviour, the system behaviour is unstable on the small and large scales.

large scale: scaling up conservative solute concentration, usually small-scale perturbations in the flow field result in large-scale spreading effects. If the density-driven flow is unstable on small scales, diverging spreading effects should be found on larger scales too, unless there are large-scale stabilising mechanisms.

3.2 The Small-Scale Stability Criterion

A stability criterion for flow in a homogeneous medium without dispersion is derived in this section. The derivation is accomplished by transforming the small-scale equation

$$\rho(\omega) \frac{\partial \omega_1}{\partial \tau} + \frac{L}{D_{\parallel}} \mathbf{v} \cdot \nabla_{\mathbf{y}} \omega_1 + \frac{L}{D_{\parallel}} \tilde{\mathbf{v}} \cdot \nabla_{\mathbf{x}} \omega_0 - \nabla_{\mathbf{y}} \cdot \mathbf{D}^* \nabla_{\mathbf{y}} \omega_1 = 0$$

into Fourier space. The solution ω_1 to the equation is assumed to depend on the large-scale mass fraction and have the form $\omega_1(\mathbf{x}, \mathbf{y}, t, \tau) = \chi^{\omega} \cdot \nabla_{\mathbf{x}} \omega_0(\mathbf{x}, t)$, with χ^{ω} the solution to the cell problem. By assuming the large-scale concentration gradient $\nabla_{\mathbf{x}} \omega_0$ to be constant on small scales (Held et al. 2005), one has $\omega_1 = \omega_1(\mathbf{y}, \tau)$. This allows the small-scale equation to be solved directly using the Fourier transform method without expressing it explicitly in terms of χ^{ω} as was done in Held et al. (2005).

Generally, the Fourier transform of a variable r is defined as

$$r(\mathbf{y}, \tau) = \frac{1}{(2\pi)^d} \int_{\mathbb{R}^d} e^{i\mathbf{q} \cdot \mathbf{y}} \hat{r}(\mathbf{q}, \tau) d\mathbf{q} , \quad (3.12)$$

where \mathbf{q} denotes the Fourier space variable and d the number of spatial dimensions. One then has:

$$\begin{aligned} \mathbf{v} \cdot \nabla_{\mathbf{y}} \omega_1(\mathbf{y}, \tau) &= \mathbf{v} \cdot \nabla_{\mathbf{y}} \frac{1}{(2\pi)^d} \int_{\mathbb{R}^d} e^{i\mathbf{q} \cdot \mathbf{y}} \hat{\omega}_1(\mathbf{q}, \tau) d\mathbf{q} \\ &= \frac{1}{(2\pi)^d} \int_{\mathbb{R}^d} i\mathbf{v} \cdot \mathbf{q} \hat{\omega}_1(\mathbf{q}, \tau) e^{i\mathbf{q} \cdot \mathbf{y}} d\mathbf{q} . \end{aligned}$$

Similarly,

$$\nabla_{\mathbf{y}} \cdot \mathbf{D}^* \nabla_{\mathbf{y}} \omega_1(\mathbf{y}, \tau) = -\frac{1}{(2\pi)^d} \int_{\mathbb{R}^d} \mathbf{D}^* \mathbf{q} \cdot \mathbf{q} \hat{\omega}_1(\mathbf{q}, \tau) e^{i\mathbf{q} \cdot \mathbf{y}} d\mathbf{q} .$$

To shorten the notation, ω_1 is subsequently written everywhere for $\hat{\omega}_1$. The possibility of confusion is minimal because $\hat{\omega}_1$ is a function of \mathbf{q} , whereas ω_1 is a function of \mathbf{y} and these dependencies are always written explicitly. Using the above results,

the small-scale equation can be written in Fourier space as:

$$\rho(\omega) \frac{\partial \omega_1(\mathbf{q}, \tau)}{\partial \tau} + i \frac{L}{D_{\parallel}} \mathbf{q} \cdot \mathbf{v} \omega_1(\mathbf{q}, \tau) + \mathbf{D}^* \mathbf{q} \cdot \mathbf{q} \omega_1(\mathbf{q}, \tau) = -\frac{L}{D_{\parallel}} \tilde{\mathbf{v}}(\mathbf{q}) \cdot \mathbf{G} , \quad (3.13)$$

with \mathbf{G} the Fourier transform of $\nabla_{\mathbf{x}} \omega_0$, which is supposed to be constant (Held et al. 2005). The velocity fluctuations $\tilde{\mathbf{v}}(\mathbf{q})$ are generally caused by fluctuations in the mass fraction and the permeability field. In the following we assume $\tilde{\mathbf{v}}(\mathbf{q})$ to be caused by fluctuations in the mass fraction ω_1 only. One can then write

$$\tilde{\mathbf{v}}(\mathbf{q}, \tau) = \mathbf{M}(\mathbf{q}) \omega_1(\mathbf{q}, \tau) , \quad (3.14)$$

where $\mathbf{M}(\mathbf{q})$ is the contribution of the mass fraction to the velocity fluctuations. Explicit formulas for $\mathbf{M}(\mathbf{q})$ are derived in appendix A.1 for the case of a divergence-free velocity field.

Using (3.14) in (3.13) one obtains

$$\begin{aligned} \rho(\omega) \frac{\partial \omega_1(\mathbf{q}, \tau)}{\partial \tau} + i \frac{L}{D_{\parallel}} \mathbf{v} \cdot \mathbf{q} \omega_1(\mathbf{q}, \tau) + \mathbf{D}^* \mathbf{q} \cdot \mathbf{q} \omega_1(\mathbf{q}, \tau) \\ = -\frac{L}{D_{\parallel}} \mathbf{M}(\mathbf{q}) \cdot \mathbf{G} \omega_1(\mathbf{q}, \tau) . \end{aligned} \quad (3.15)$$

Equation (3.15) clearly has the form

$$\frac{\partial \omega_1}{\partial \tau} + b \omega_1 = 0 \quad (3.16)$$

with $b = \frac{1}{\rho(\omega)} \left(i \frac{L}{D_{\parallel}} \mathbf{v} \cdot \mathbf{q} + \mathbf{D}^* \mathbf{q} \cdot \mathbf{q} + \frac{L}{D_{\parallel}} \mathbf{M}(\mathbf{q}) \cdot \mathbf{G} \right)$. Its solution is $\omega_1 = \omega_1(0) e^{-bt}$. If one is interested in the long-time behaviour of the system, a stability criterion can easily be formulated:

If the real part of b is positive, then the solution is stable.

In our case, this means the solution is stable if

$$\Lambda(\mathbf{q}) := \mathbf{D}^* \mathbf{q} \cdot \mathbf{q} + \frac{L}{D_{\parallel}} \mathbf{M}(\mathbf{q}) \cdot \mathbf{G} \geq 0 . \quad (3.17)$$

In other words, the solution is unstable if there exists \mathbf{q} such that $\Lambda(\mathbf{q}) < 0$. Physically, it means that the solution grows indefinitely with time in the point \mathbf{q} . When dispersion is not considered, one can derive from (3.17) a stability criterion which does not depend on \mathbf{q} . The quantity $\mathbf{M}(\mathbf{q})$ is used in sections 3.2.1 and 3.2.2 to derive stability criteria for flow processes aligned parallel and orthogonal to gravity.

3.2.1 The Small-scale Criterion for Flow Parallel to Gravity

The mean flow \mathbf{v}_0 and the gravity force \mathbf{g} are assumed to be parallel. Thus, we assume \mathbf{v}_0 and \mathbf{g} to point against the vertical \mathbf{e}_2 -direction: $\mathbf{v}_0 = v_0 \mathbf{e}_2$ and $\mathbf{v}_0^g = v_0^g \mathbf{e}_2$, with $v_0, v_0^g < 0$. The mean velocity, the gravity-driven velocity and concentration gradient then read:

$$\mathbf{v}_0 = \begin{pmatrix} 0 \\ v_0 \end{pmatrix}, \mathbf{v}_0^g = \begin{pmatrix} 0 \\ v_0^g \end{pmatrix}, \mathbf{G} = \begin{pmatrix} 0 \\ G_2 \end{pmatrix}.$$

Equation (3.15) then becomes

$$\rho \frac{\partial \omega_1(\mathbf{q}, \tau)}{\partial \tau} + i \frac{L}{D_{\parallel}} q_2 v_0 \omega_1(\mathbf{q}, \tau) + \mathbf{D}^* \mathbf{q} \cdot \mathbf{q} \omega_1(\mathbf{q}, \tau) = - \frac{L}{D_{\parallel}} \mathbf{M}(\mathbf{q}) \cdot \mathbf{G} \omega_1(\mathbf{q}, \tau) , \quad (3.18)$$

where $\mathbf{M}(\mathbf{q}) \cdot \mathbf{G}$ is given by

$$\begin{aligned} \mathbf{M}(\mathbf{q}) \cdot \mathbf{G} &= M_2(\mathbf{q}) G_2 \\ &= (\alpha - \beta) \left[\left(1 - \frac{q_2^2}{\|\mathbf{q}\|^2} \right) v_0 G_2 \right] + \alpha \left[\left(1 - \frac{q_2^2}{\|\mathbf{q}\|^2} \right) v_0^g G_2 \right] . \end{aligned} \quad (3.19)$$

To isolate the dominant contribution of $\mathbf{M}(\mathbf{q}) \cdot \mathbf{G}$, it is expanded around $q_2 = 0$:

$$M_2(\mathbf{q}) G_2 = (\alpha - \beta) v_0 G_2 + \alpha v_0^g G_2 + O(q_2) , \quad (3.20)$$

which gives together with (3.17)

$$\Lambda_p = \frac{L}{D_{\parallel}} G_2 ((\alpha - \beta) v_0 + \alpha v_0^g) . \quad (3.21)$$

The diffusion/dispersion effects have been neglected in (3.21). A positive Λ_p in-

icates stable flow while a negative Λ_p indicates unstable behaviour. The various parameters appearing in the expression affect Λ_p differently: increasing the density of the displacing fluid would increase its tendency to “sink” into the displaced water and thus destabilise the system while increasing the viscosity of the displacing fluid increases stability by dissipating the energy of the instabilities. Increased velocity (in the direction of finger growth) on the other hand favours finger propagation and thus destabilises the system. When orthogonal to the direction of finger development, high velocity offers less time to instabilities to grow into fingers, thereby stabilising the system.

3.2.2 The Small-scale Criterion for Flow Orthogonal to Gravity

We need to define the following three vectors for the mean velocity due to external pressure, the gravity-driven velocity and concentration gradient respectively as follows:

$$\mathbf{v}_0 = \begin{pmatrix} v_0^p \\ v_0^g \end{pmatrix}, \mathbf{v}_0^g = \begin{pmatrix} 0 \\ v_0^g \end{pmatrix}, \mathbf{G} = \begin{pmatrix} G_1 \\ G_2 \end{pmatrix}.$$

Equation (3.15) then reads

$$\begin{aligned} \rho(\omega) \frac{\partial \omega_1(\mathbf{q}, \tau)}{\partial \tau} + i \frac{L}{D_{\parallel}} (q_1 v_0^p + q_2 v_0^g) \omega_1(\mathbf{q}, \tau) + \mathbf{D}^* \mathbf{q} \cdot \mathbf{q} \omega_1(\mathbf{q}, \tau) \\ = - \frac{L}{D_{\parallel}} (M_1(\mathbf{q}) G_1 + M_2(\mathbf{q}) G_2) \omega_1(\mathbf{q}, \tau) . \end{aligned} \quad (3.22)$$

Analogous to section 3.2.1 we now expand the product $\mathbf{M}(\mathbf{q}) \cdot \mathbf{G}$ around

$q_1 v_0^p + q_2 v_0^g = 0$, which results in $q_1 = -q_2 \frac{v_0^g}{v_0^p}$. We further define the ratio

$$a = \frac{q_1}{q_2} = - \frac{v_0^g}{v_0^p} \quad (3.23)$$

and use the ratio q_1/q_2 in evaluating the vector products in Appendix A.1 leading

to the explicit form of $\mathbf{M}(\mathbf{q})$:

$$\mathbf{M}(\mathbf{q}) = \begin{pmatrix} M_1(\mathbf{q}) \\ M_2(\mathbf{q}) \end{pmatrix} = \frac{1}{a^2 + 1} \begin{pmatrix} (\alpha - \beta)v_0^p - a(2\alpha - \beta)v_0^g \\ a^2(2\alpha - \beta)v_0^g - a(\alpha - \beta)v_0^p \end{pmatrix}. \quad (3.24)$$

We use the ratio of the velocities from (3.23) in (3.24) to further obtain:

$$\mathbf{M}(\mathbf{q}) \cdot \mathbf{G} = (v_0^g G_2 + v_0^p G_1) \left[(\alpha - \beta) + \left(\frac{a^2}{a^2 + 1} \right) \alpha \right] + O(q_1 v_0^p + q_2 v_0^g). \quad (3.25)$$

Equation (3.25) together with (3.17) give the stability number (3.26) in which the diffusion/dispersion effects are neglected:

$$\Lambda_o = \frac{L}{D_{\parallel}} (v_0^g G_2 + v_0^p G_1) \left[(\alpha - \beta) + \left(\frac{a^2}{a^2 + 1} \right) \alpha \right]. \quad (3.26)$$

L is the macroscopic length taken equal to the domain size in mean flow direction, D_{\parallel} the longitudinal dispersion, α and β are the maximum relative density and viscosity coefficients computed from the respective state dependencies; v_0^p the large scale pressure-driven velocity component; v_0^g the gravity-driven velocity component; a the ratio $-v_0^g/v_0^p$ and G_1, G_2 the respective concentration gradients in the directions orthogonal and parallel to gravity respectively. As noted before, *flow is stable for positive Λ_o* .

Λ_o and Λ_p are dimensionless due to the density terms contained in the velocities.

3.3 The Large-scale Stability Criterion

Investigating the stability on larger scales requires the evaluation of the macrodispersion coefficients (3.11). Generally, the macrodispersion coefficients depend on \tilde{v}_i and χ_j^ω . If \tilde{v}_i and χ_j^ω show indefinite temporal growth independent of \mathbf{q} (in the direction of finger development), the flow behaviour is unstable on small scales. Consequently, D_{ij}^{eff} (in the same direction) also grows indefinitely with time and in the absence of other stabilising mechanisms, unstable behaviour at small scales

results in unstable behaviour at larger scales. Large-scale heterogeneous effects are presented in section 5.3

3.4 Numerical Results

The criterion for systems aligned orthogonal to gravity (see Fig. 2.8 on page 35) is tested and the results presented in this section. The parameters given in Table 2.1 on page 37 were used. The choice was motivated by experimental work in Schincariol and Schwartz (1990), from which the research to analyse the effect of numerical effects on stability (Schincariol et al. 1994) was based. The authors also undertook similar studies to analyse heterogeneous effects among others.

The study of numerical effects in Schincariol et al. (1994) was particularly important in obtaining an optimum grid refinement capable of delivering a solution free from numerical artifacts. With a stable solution ensured, it was unnecessary to apply upwind techniques, which would otherwise have introduced *artificial diffusion* that in turn would have distorted the actual stability states.

3.4.1 The Schincariol Problem

As stated above, the problem was initially introduced in experimental work by Schincariol and Schwartz (1990). Schincariol et al. (1994) studied numerical instabilities by successively refining the mesh and time steps until a numerically stable solution was obtained. They then induced physical instabilities in the numerically stable solution by repeatedly changing the width of the solute inlet.

We study the effect of increasing grid refinement (subsequently reducing the Péclet number) and present the results in the following. A problem was implemented using similar Péclet and Courant numbers, simulation parameters, domain size, boundary conditions and state dependencies as those in Schincariol et al. (1994). Dispersion

was treated according to Scheidegger's law:

$$\mathbf{D} = D_m \mathbf{I}_d + (\alpha_{\parallel} - \alpha_{\perp}) \frac{\mathbf{v} \otimes \mathbf{v}}{\|\mathbf{v}\|} + \alpha_{\perp} \|\mathbf{v}\| \mathbf{I}_d$$

where $\alpha_{\parallel}, \alpha_{\perp}$ are the longitudinal and transverse dispersivities respectively, D_m the molecular diffusion coefficient, \mathbf{I}_d the identity matrix and \mathbf{v} the velocity with the norm $\|\mathbf{v}\| = \sqrt{\mathbf{v} \cdot \mathbf{v}}$. The results are shown in the Fig. 3.1. The clear improvement

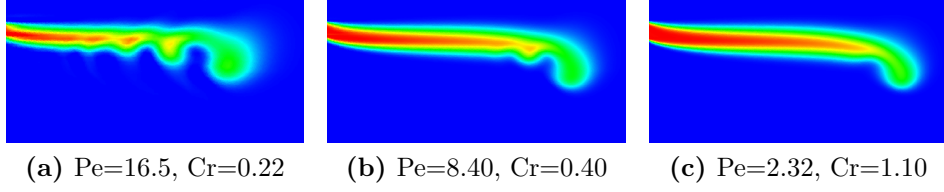


Fig. 3.1 A reproduction of Schincariol results with full equations

in the numerical solution with grid refinement is also documented in Oldenburg and Pruess (1995), Frolkovič and De Schepper (2001) and Diersch and Kolditz (2002). These results were not part of the stability analyses but simply a means to achieve an optimum grid free from numerical errors. Finer mesh and time refinements than in Fig. 3.1c were adopted as standard in all subsequent simulations. Next, we study physical instabilities by varying the density, viscosity and flow velocity, one at a time on a numerically stable configuration. The results are then compared to the predictions from the computed stability numbers.

3.4.2 Stability Investigations

For the reference problem from Schincariol et al. (1994), v_0^p and the component G_2 of the vector \mathbf{G} are positive while the component G_1 and v_0^g are negative. We apply the stability number (3.26) for flow orthogonal to gravity:

$$\Lambda_o = \frac{L}{D_{\parallel}} (v_0^g G_2 + v_0^p G_1) \left[(\alpha - \beta) + \left(\frac{a^2}{a^2 + 1} \right) \alpha \right] .$$

When the pressure-driven velocity component v_0^p is very small, a becomes very large and the term $a^2/(a^2 + 1) \rightarrow 1$, reducing the square bracket to $(2\alpha - \beta)$. We also

have $v_0^g G_2 + v_0^p G_1 < 0$ in this case and flow remains stable as long as $(2\alpha - \beta) < 0$ or $\alpha < \beta/2$. The other possibility is a large pressure-driven velocity component that makes $a^2/(a^2 + 1) \rightarrow 0$ but that could not be simulated.

The diffusive scaling results in a dimensionless stability number, which is accomplished by multiplication with L/D_{\parallel} where L is the domain length in mean flow direction and D_{\parallel} the longitudinal dispersion. With negligible molecular diffusion, $D_{\parallel} \approx \|\mathbf{v}\|\alpha_{\parallel}$.

Before the results of the numerical simulations are presented, we need to clarify the decision regarding stable and unstable simulations. The distinction was not very easy since for most flow configurations a salt finger evolves at the tip of the plume. The lobe at the tip is caused by the action of the horizontal velocity component sweeping away small-wavelength perturbations, causing salt to accumulate in the tip and form the lobe. In stable configurations it is assumed that after a certain time the finger evolution stabilises with only the tip and nearly no additional undulations.

Figure 3.2 shows the computations for the 2nd and 3rd entries in Table 3.1, predicted as stable and unstable respectively.

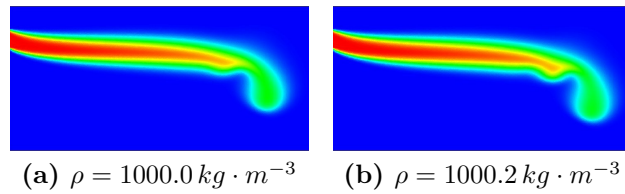


Fig. 3.2 Density effects: $\beta = 3.992 \times 10^{-3}$

To investigate the stability of the systems in Fig. 3.2 further, the fingers were allowed more evolution time in a domain twice the length of the test problem. The respective results are shown in figures 3.3 and 3.4.

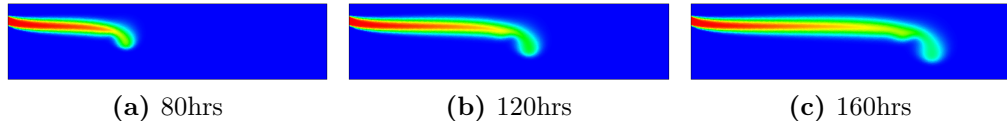


Fig. 3.3 Finger evolution in a bigger domain, $\rho = 1000 \text{ kg} \cdot \text{m}^{-3}$

The differences became more pronounced: more fingers formed and the tip of the

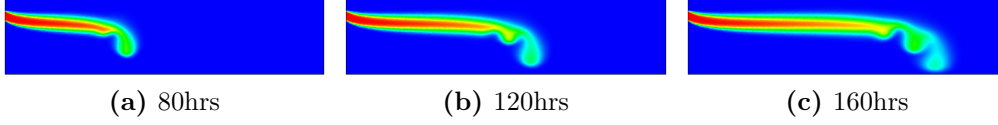


Fig. 3.4 Finger evolution in a bigger domain, $\rho = 1000.2 \text{ kg} \cdot \text{m}^{-3}$

plume sank through a bigger vertical distance in Fig. 3.4, the unstable case. One can therefore hypothesise that there exists a critical horizontal plane that separates stable and unstable flows. If the front travels beyond that plane, the system is unstable, otherwise it is stable.

A maximum grid diameter of 0.00281 ($\text{Pe}=1.614$ and $\text{Cr}=0.157$) was used as the standard discretisation for figures 3.2 through 3.7. The stability number was computed using (3.26) with the parameters in Table 2.1. The effects of density and viscosity on stability were investigated separately at an end time of 90 hours, while flow velocity required different end times mentioned in section 3.4.2.3.

3.4.2.1 Density Effects

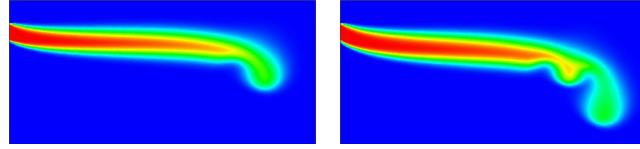
At a constant maximal viscosity of $1.006 \times 10^{-3} \text{ Pa} \cdot \text{s}$ ($\beta = 0.00399$) and $v_0^p = 2.75 \times 10^{-6} \text{ m} \cdot \text{s}^{-1}$, the maximum density was gradually increased and the computed stability numbers and simulated flow patterns are shown in Table 3.1 and figures 3.2 and 3.5. The bold face entries in Table 3.1 correspond to the grey-area cases in Fig. 3.2 that were clarified in a bigger domain.

Table 3.1 Stability results for variable density at constant viscosity $\beta = 0.00399$

Maximal Density [$\text{kg} \cdot \text{m}^{-3}$]	α ($\times 10^{-3}$)	β ($\times 10^{-3}$)	stability no. Λ_o ($\times 10^{-3}$)	Simulation stable?
999.70	1.5027	3.99	5.8377	Yes
1000.00	1.8032	3.99	2.2813	Yes
1000.20	2.0036	3.99	-0.0896	No
1000.40	2.2040	3.99	-2.4606	No

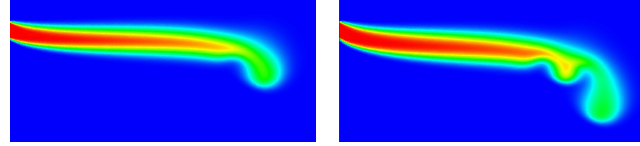
The foregoing analysis was made without the Boussinesq approximation. Figure 3.6 shows the finger evolution with the approximation invoked in the simulator.

The results showed no significant differences at a maximum density contrast of 0.22%. However, all subsequent analyses were made without the approximation. A



(a) $\rho = 999.7 \text{ kg} \cdot \text{m}^{-3}$ (b) $\rho = 1000.4 \text{ kg} \cdot \text{m}^{-3}$

Fig. 3.5 Density effects: $\beta = 3.992 \times 10^{-3}$



(a) $\rho = 999.7 \text{ kg} \cdot \text{m}^{-3}$ (b) $\rho = 1000.4 \text{ kg} \cdot \text{m}^{-3}$

Fig. 3.6 Density effects with the Oberbeck-Boussinesq approximation

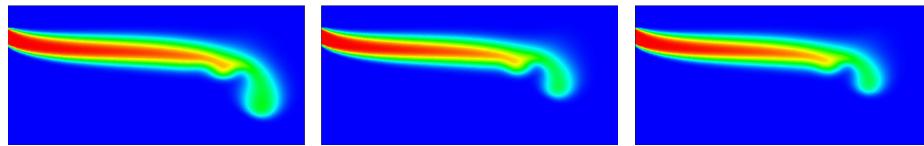
comparison with stability numbers computed with equations in which the approximation had been invoked presented in section 3.5.

3.4.2.2 Viscosity Effects

To study the effect of viscosity, an attempt was made to stabilise the unstable flow configuration in Fig. 3.2b by increasing viscosity. The results are shown in Table 3.2 and Fig. 3.7.

Table 3.2 Variable viscosity effects at constant density $\alpha = 0.0020036$

Viscosity [Pa.s]	β ($\times 10^{-3}$)	α ($\times 10^{-3}$)	stability no. Λ_o ($\times 10^{-3}$)	Simulation stable?
0.001006	3.992	2.0036	-0.09	No
0.001200	197.605	2.0036	1145.50	Yes
0.001250	247.505	2.0036	1440.70	Yes



(a) $\mu = 0.001006$ (b) $\mu = 0.001200$ (c) $\mu = 0.001250$

Fig. 3.7 Viscosity effects: $\alpha = 2.1038 \cdot 10^{-3}$

Again, the simulated results in Fig. 3.7 are in reasonable agreement with the theory in Table 3.2. Viscosity dissipates the energy of instabilities and the successive energy

deficiencies result in reduced finger growth as Fig. 3.7 clearly shows. Another visible effect of increasing viscosity is the reduction in the horizontal distance covered by the plume, caused by increased viscous drag.

3.4.2.3 Flow velocity Effects

The following are the results for the effect of the pressure-driven velocity component v_0^p . The respective criteria for stability at low and high flow are $(\alpha < \beta/2)$ and $(\alpha - \beta) + a^2/(a^2 + 1)\alpha < 0$ as was explained on page 51.

With a maximum grid diameter of 0.00281, the velocity was set to $1.5 \times 10^{-6} \text{ m} \cdot \text{s}^{-1}$ (Pe=1.25, Cr=0.086) and the stability condition at low flow tested. Low flow velocity offers enough time for instabilities to develop into fingers, thus destabilising the system. High velocity on the other hand hinders the growth of instabilities: a velocity of $1.9 \times 10^{-4} \text{ m} \cdot \text{s}^{-1}$ (Pe=2.466, Cr=10.82) was used to test if the criterion could capture the phenomena. The α and β combinations for the computations and simulations were set to the values in Table 3.3 and the results are given in Fig. 3.8: figures 3.8a (after 180hrs) and 3.8b (after 100hrs) show the respective stable and unstable cases at low velocity while Fig. 3.8c (after 90min) shows stable flow at high velocity.

Table 3.3 Flow velocity effects at various densities and viscosities

Velocity ($\times 10^{-6}$) $\text{m} \cdot \text{s}^{-1}$	Maximal		α ($\times 10^{-3}$)	β ($\times 10^{-3}$)	Stability Number Λ_o ($\times 10^{-3}$)	Simulation Stable?
	Density $\text{kg} \cdot \text{m}^{-3}$	Viscosity ($\times 10^{-3}$) $\text{Pa} \cdot \text{s}$				
1.5 (Low)	999.0	1.0060	0.8014	3.9920	14.1252	Yes
1.5 (Low)	1000.0	1.0050	1.8032	2.9920	-3.6211	No
190 (High)	1000.3	1.0060	2.1040	3.9960	0.0230	Yes

The stability predictions at low flow were in good agreement with simulations but came very late at high flow. The simulations stabilised at $v_0^p = 5 \times 10^{-6} \text{ m} \cdot \text{s}^{-1}$ while the earliest that the criterion could predict was $1.9 \times 10^{-4} \text{ m} \cdot \text{s}^{-1}$, at which velocity the flow was advection-dominated. The use of upwind schemes is recommended by Frolkovič and De Schepper (2001) for advection-dominated flow but we did not apply any such techniques.

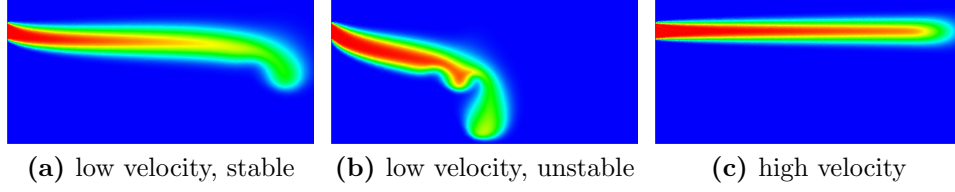


Fig. 3.8 Velocity effects

3.5 Discussion of Results

In contrast to the approach presented here, most other investigations like the one of Welty and Gelhar (1991) and Coskuner (1993) applied the Oberbeck-Boussinesq assumption. Since both do not explicitly state a stability criterion of flow orthogonal to gravity, we could not compare different criteria directly. The following can be derived from an expression in Welty and Gelhar:

$$\Lambda_o^{Welty} = (v_0^g G_2 + v_0^p G_1) \left[-\beta + \left(\frac{a^2}{a^2 + 1} \right) (\alpha - \beta) \right] , \quad (3.27)$$

where the formalisms and notations introduced earlier are still valid.

We assumed that the most important difference between the results developed here and Welty and Gelhar's is the Boussinesq assumption. In the following, the assumption with its underlying disregard of density variations except in the buoyancy term is taken as the sole basis for the comparison. Table 3.4 compares the respective stability numbers computed using (3.26) and (3.27) against numerical simulations. The stabilising effect of the Boussinesq assumption becomes evident in the stable predictions from (3.27) at fairly big density contrasts.

Table 3.4 A comparison between the current and Welty's results

Max. density ($kg \cdot m^{-3}$)	Stability number $\Lambda_o \times 10^{-3}$		Numerical Simulation Stable?
	Flow orthogonal to gravity		
	Current work	Welty's	
999.7	5.8377	38.3478	Yes
1000.0	2.2813	36.5697	Yes
1000.4	-2.4606	34.1988	No
1002.0	-21.4280	24.7152	No
1006.0	-68.8465	1.0062	No
1006.5	-74.7738	-1.9574	No

Next are numerical simulations at $\rho_{max} = 1000.4$ and $1002 \text{ kg} \cdot \text{m}^{-3}$, a sample pair of densities where the criteria conflicted. The criterion from Welty and Gelhar predicted that flow remains stable at densities well beyond $1002.0 \text{ kg} \cdot \text{m}^{-3}$ (Table 3.4) whereas the one derived here predicted instabilities at $1000.2 \text{ kg} \cdot \text{m}^{-3}$. Figures 3.9a and 3.9b show the evolution of fingers at $1000.4 \text{ kg} \cdot \text{m}^{-3}$ and $1002.0 \text{ kg} \cdot \text{m}^{-3}$ respectively with $\text{Pe}=1.614$ and $\text{Cr}=0.157$ after 90 and 85 hours respectively.

At $1000.4 \text{ kg} \cdot \text{m}^{-3}$, the initial instabilities do not develop into a distinctive finger until after 80 hours. At $1002.0 \text{ kg} \cdot \text{m}^{-3}$, a distinctive finger that was visible after 40 hours continued to grow and hit the bottom of the domain after 50 hours indicating a very unstable system. That is contrary to the stable prediction from Welty and Gelhar. Therefore, the current criterion with its limitations was able to make superior predictions at a smaller density contrast.

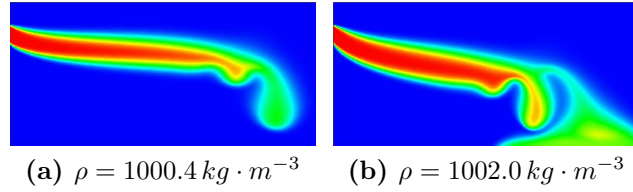


Fig. 3.9 Evolution of fingers at conflicting stability predictions

The derived criterion which utilises the full equations was able to predict the onset of instabilities much earlier at 0.20% density contrast while Welty and Gelhar's first predicted instabilities at a density contrast of 0.83% and produced bigger stability numbers at any given density contrast. The effect of invoking the Boussinesq assumption therefore results in stabilisation of the system.

The stability predictions with increasing flow velocity came very long after the numerical simulations had stabilised. This failure was attributed to the dispersive effects that were not included in the criterion, yet dispersion was implemented in the simulator according to Scheidegger's law where it varies as a function of the velocity to the power 2.

Chapter 4

Homogeneous Medium: Extension to Dispersion¹

The previously derived stability numbers neglected the effects of dispersion and medium heterogeneity. The stability number

$$\Lambda_p = \frac{LG_2}{D_{\parallel}}((\alpha - \beta)v_0 + \alpha v_0^g)$$

for systems parallel to gravity is extended in this chapter to include dispersion. The impact of small-scale dispersion on stability can be accounted for by analysing the spectrum of perturbation wavelengths that the dispersive mixing can damp out and prevent from growing into fingers. Another important factor is the characteristic region or the *dispersion mixing zone* within which the dispersive effects are felt. Perturbations with different wavelengths will be induced by a sinus function imposed as a boundary condition at the solute inflow region. An expression for the mixing zone width will also be derived and presented here. The earlier stability number will be rewritten in form of a Rayleigh number to enable comparison with other works. The stability is related to the Rayleigh number and the number of fingers present.

¹Published in Musuuza et al. (2011) doi:10.1016/j.advwatres.2010.11.008

4.1 Stabilising Effects of Small-Scale Dispersion

Small-scale dispersion is the main stabilising mechanism in homogeneous media. It initiates the exchange of solute between regions with different concentrations, leading to the formation of a mixing zone. The mechanism is analogous to capillary effects in multiphase systems that cause fluid exchange between regions of different saturations. The width of the zone grows with time and is proportional to the prevailing mixing (Marle 1981). The zone retards the growth of instabilities and can completely smooth out perturbations with wavelengths below a certain critical value.

The inclusion of dispersion in the earlier criterion is in essence an account for the action of the mixing zone hindering the growth of fingers for a certain range of instability wavelengths. To that end, the method of normal modes (Coskuner and Bentsen 1990, Farber 1997, Drazin and Reid 2004) is used to postulate the solution of the homogenization theory small-scale equation

$$\rho(\omega) \frac{\partial \omega_1}{\partial \tau} + \frac{L}{D_{\parallel}} \mathbf{v} \cdot \nabla_{\mathbf{y}} \omega_1 + \frac{L}{D_{\parallel}} \tilde{\mathbf{v}} \cdot \nabla_{\mathbf{x}} \omega_0 - \nabla_{\mathbf{y}} \cdot \mathbf{D}^* \nabla_{\mathbf{y}} \omega_1 = 0$$

as a product

$$\omega_1(\mathbf{y}, \tau) = \omega_1(y_2, \tau) \exp \left(-\frac{iy_1}{\frac{\lambda}{\zeta}} \right) , \quad (4.1)$$

where λ is the perturbation wavelength and ζ the characteristic length, whose inclusion maintains the dimensionless form of (4.1). For vertical flow $v_1 = 0$ so we have $\mathbf{v} \cdot \nabla_{\mathbf{y}} \omega_1(\mathbf{y}, \tau) = v_2 \frac{\partial \omega_1(\mathbf{y}, \tau)}{\partial y_2}$ and the term $\frac{L}{D_{\parallel}} \tilde{\mathbf{v}}(\mathbf{y}, \tau) \cdot \nabla_{\mathbf{x}} \omega_0$ can be approximated to $\Lambda_p \omega_1(\mathbf{y}, \tau)$. The small-scale equation then becomes

$$\exp \left(-i \left(\frac{\zeta}{\lambda} \right) y_1 \right) \left[\rho(\omega) \frac{\partial \omega_1(y_2, \tau)}{\partial \tau} + \frac{L}{D_{\parallel}} v_2 \frac{\partial \omega_1(y_2, \tau)}{\partial y_2} + \Lambda_p \omega_1(y_2, \tau) - \mathbf{D}^* \left(\frac{\partial^2 \omega_1(y_2, \tau)}{\partial y_2^2} - 2i \left(\frac{\zeta}{\lambda} \right) \frac{\partial \omega_1(y_2, \tau)}{\partial y_2} - \left(\frac{\zeta}{\lambda} \right)^2 \omega_1(y_2, \tau) \right) \right] = 0 . \quad (4.2)$$

The ω_1 and $\partial \omega_1$ terms scale with ϵ^0 and ϵ^{-1} respectively (Held et al. 2005). If we

stick to the linear perturbation theory, the $\partial\omega_1$ and higher derivative terms drop out to leave $\Lambda_p + \left(\frac{\zeta}{\lambda}\right)^2 \mathbf{D}^\star = 0$. Using the expression for the modified dispersion tensor

$$\mathbf{D}^\star = \rho(\omega) \frac{\mathbf{D}}{D_\parallel}$$

and concentrating on the stabilising transverse component of the tensor one obtains the new stability number in which dispersive effects are included:

$$\Lambda_p^\star = \Lambda_p + \frac{D_\perp}{D_\parallel} \left(\frac{\zeta}{\lambda}\right)^2, \quad (4.3)$$

where D_\perp, D_\parallel are respectively the transverse and longitudinal dispersion. It is not necessary to write the $\rho(\omega)$ from \mathbf{D}^\star because a similar term from the velocity fluctuations $\tilde{\mathbf{v}}$ is embedded in the Λ_p that appears in (4.2) and the density terms cancel out. Therefore (4.3) is dimensionless.

According to Swartz and Schwartz (1998), there exists a critical perturbation wavelength below which fingers do not develop i.e. a threshold perturbation wavelength below which small-scale mixing can sufficiently reduce the concentration gradients and damp out instabilities. Thus for some unfavourable density contrasts ($\Lambda < 0$), inclusion of dispersion shifts the system towards stability.

The second term in the right-hand side of (4.3) always evaluates to a positive quantity. The dispersive contribution therefore always stabilises, with the effects increasing with the transverse dispersion and the characteristic length while it reduces with the longitudinal dispersion and the perturbation wavelength.

By definition there is an inverse relationship between λ and the wavenumber γ (Schincariol et al. 1997, Swartz and Schwartz 1998). An expression similar to (4.3) but with $\gamma [m^{-1}]$ was derived in e.g. Coskuner and Bentsen (1990). The biggest wavelength for which flow is stable corresponds to the smallest wavenumber at which unstable flow becomes stable.

The Rayleigh number gives the ratio of the destabilising gravity and buoyancy effects to the stabilising viscous and dispersive effects. For solute-induced convection (Old-

enburg and Pruess 1995, Schincariol et al. 1997, Holzbecher 1998, Kolditz et al. 1998, Reeves and Ewiera 2000, Diersch and Kolditz 2002, Johannsen 2002) the Rayleigh number is given as

$$Ra = \frac{k\Delta\rho H|g|}{D_m\phi\mu_0} , \quad (4.4)$$

where k is the permeability, $\Delta\rho$ the density contrast, H the domain height, ϕ the porosity, μ_0 the pure water viscosity and D_m the molecular diffusion coefficient. Previous stability studies evolved at establishing the critical Rayleigh number Ra_c for the onset of convection. For the Elder problem, $Ra \approx 400$ (Elder 1967, Johannsen 2003, Oldenburg and Pruess 1995; 1998, Diersch and Kolditz 2002, Kolditz et al. 1998, Meca, Alhama and González-Fernández 2007) and $Ra_c = 4\pi^2$ (Elder 1967, Coskuner and Bentsen 1990, Kolditz et al. 1998, Diersch and Kolditz 2002). They use the entire domain height and consider only diffusion, which is unrealistic considering the big density contrast of 20%.

We now reformulate the stability number (without dispersion)

$$\Lambda_p = \frac{L}{D_{\parallel}} G_2((\alpha - \beta)v_0 + \alpha v_0^g)$$

in terms of Ra to enable a direct comparison with what others did. In the absence of external pressure, the total downward velocity v_0 is purely gravity-driven and is given according to Held et al. (2005) as

$$v_0^g = \frac{k\rho_0 g}{\phi\mu_0} . \quad (4.5)$$

The stability number then becomes $\Lambda_p = \frac{k\zeta G_2 \rho_0 g}{D_{\parallel}\phi\mu_0}(2\alpha - \beta)$. From the equation of state for density

$$\rho(\omega) = \rho_0(1 + \alpha\omega)$$

one can write the changes in density as $\Delta\rho(\omega) = G_2\rho_0\alpha$. By denoting $\frac{k\zeta\Delta\rho g}{D_{\parallel}\phi\mu_0}$ as the longitudinal solutal Rayleigh number Ra_{\parallel} , the stability number becomes

$$\Lambda_p = Ra_{\parallel} \left(\frac{2\alpha - \beta}{\alpha} \right) . \quad (4.6)$$

A transverse solutal Rayleigh number Ra_{\perp} can similarly be defined by using D_{\perp} (Schincariol et al. 1997, Diersch and Kolditz 2002). The ratio $\eta = Ra_{\perp} : Ra_{\parallel}$ was reported in Schincariol et al. (1997) to provide useful information regarding stability transition.

The argument in Schincariol et al. (1997) has been followed: the characteristic length and dispersion are used instead of the domain size and molecular diffusion respectively (see also Oldenburg and Pruess (1995), Reeves and Ewiera (2000) and Diersch and Kolditz (2002)).

The reformulation of Λ_p in terms of a Rayleigh number dependent on the characteristic length required the replacement of the domain size L with the characteristic length ζ . That affects the magnitude of Λ_p but not the sign. The use of ζ is plausible because the criterion was derived from the small-scale rather than the macroscopic equation and secondly we are seeking an intermediate scale (an aggregation of several small scales) at which to study the dispersive effects.

4.1.1 The Perturbation Wavelength λ

The perturbation wavelength is fundamental in existing stability criteria (Schincariol 1998). Perturbations with small wavelengths have closely spaced troughs and crests as shown in Fig. 4.1.

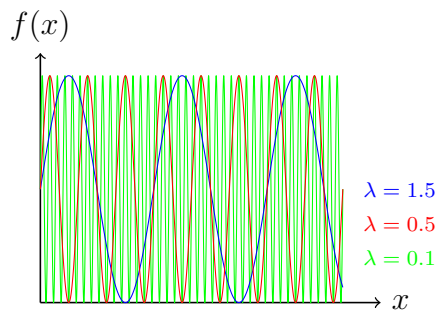


Fig. 4.1 Trough/Crest spacing for different wavelengths

The troughs at low wavelengths can easily be merged into an almost continuous front by fluid exchange arising from dispersion. That phenomenon is similar to the

stabilising effect of capillary forces in multiphase flow systems with small perturbation wavelengths (Marle 1981). However, the crests provide numerous motions in the opposite direction that reduce the quantity of solute entering the domain and retards the overall advance of the front, thus hindering finger development.

The distance between adjacent troughs and crests is increased at bigger wavelengths and fluid exchange by dispersion might fail to merge them. The troughs can then individually or aggregatively initiate and propagate fingers. This phenomenon is again similar to the failure by capillary forces to stabilise systems with large perturbation wavelengths (Marle 1981).

Marle (1981) also documents the existence of a critical wavelength in perturbations with regular spatial periodicity. We propose to perturb the inflow with sinus functions of varying wavelengths (see also Schincariol et al. (1994; 1997)), from which λ_{crit} can be obtained as the biggest stable wavelength. The following function was used as the inflow boundary condition:

$$\omega(x, t) = A_0 \left[1.0 + \sin \left(\frac{2\pi(x - \delta)}{\lambda} \right) \right] . \quad (4.7)$$

$A_0 = 0.5$ is the amplitude chosen such that the maximum mass fraction was 1 when the sinus function attained its peak. $\delta = 0.4$ the abscissa of the start of the inflow zone (see Figure 2.9), x the horizontal distance into the inflow region and λ the wavelength of the perturbation. 1.0 was added to avoid unphysical negative mass fractions i.e. constrained the minimum mass fraction to zero. A similar function was used in Marle (1981) to perturb the position of the interface between two fluids.

4.1.2 The Characteristic Scaling Length

There are several possibilities for the characteristic length ζ : the homogenization theory cell size, the discretisation mesh diameter and the width of the mixing zone. The latter is adopted because the cell size cannot be precisely quantified while a big mesh diameter increases numerical instabilities and destabilises the system. The characteristic length can be taken equal to the width of the mixing zone (Buès and

Aachib 1991). The width of the dispersion zone was shown in Kempers and Haas (1994) to be $\zeta = (\alpha_{\parallel} X)^{\frac{1}{2}}$, where X is an average displacement that depends on both fluid and medium properties.

It was necessary at this point to investigate the requirement that $\zeta(\alpha_{\parallel})$ should stabilise the system, which is shown in section 4.2.3.2. When (4.3) is written in an equivalent form (4.8), further credence is given to the supposition that ζ is a function of a stabilising quantity α_{\parallel} .

$$\Lambda_p^* = \frac{1}{D_{\parallel}} \left[LG_2 ((\alpha - \beta)v_0 + \alpha v_0^g) + \frac{\zeta^2 D_{\perp}}{\lambda^2} \right] > 0 , \quad (4.8)$$

$$\zeta^2 = \alpha_{\parallel} X . \quad (4.9)$$

In the subsequent, the average displacement X is assumed as a function of the medium properties (dispersivities) only:

$$X = \alpha_{\parallel}^m \alpha_{\perp}^n , \quad (4.10)$$

where m, n are some real numbers. Substituting (4.10) and the approximations $D_{\parallel} \approx \|\mathbf{v}\| \alpha_{\parallel}$ and $D_{\perp} \approx \|\mathbf{v}\| \alpha_{\perp}$ in (4.3) gives

$$\Lambda_p^* = \Lambda_p + \frac{\alpha_{\parallel}^m \alpha_{\perp}^{n+1}}{\lambda^2} . \quad (4.11)$$

Dimensional consistency of (4.10) requires $m + n = 1$ from which (4.11) becomes

$$\Lambda_p^* = \Lambda_p + \frac{\alpha_{\parallel}^m \alpha_{\perp}^{2-m}}{\lambda^2} . \quad (4.12)$$

It was again necessary to check whether α_{\perp} stabilised the system, which is shown in section 4.2.3.3. The stabilising effects of α_{\parallel} and α_{\perp} require that their respective indices in (4.12) be bigger than zero i.e. ($m > 0$) and ($2 - m > 0$), which leads to $0 < m < 2$ as an additional constraint. The value of m can be estimated by computing Λ_p^* at constant ρ_{max}, μ, λ and various α_{\parallel} and noting the range for which all α_{\parallel} give $\Lambda_p^* > 0$. The procedure is repeated for various α_{\perp} and the second range

of stable m obtained. Intersecting the two regions gives the approximate m .

4.2 Numerical Results

Johannsen (2002) showed the existence of 11 steady-state solutions for the Elder problem: *1 stable and 3 unstable with one finger, 1 stable and 4 unstable with two fingers; and 1 stable and 1 unstable with three fingers*. Both the numbers of possible solutions and fingers depended on and increased with the prevailing Ra . For the domain in Fig. 2.9 and the reference parameters we have $Ra \approx 300$ (computed with molecular diffusion and domain height), which would capture all the 11 possible solutions.

Frolkovič and De Schepper (2001) mention that Elder-type problems usually show unstable behaviour. They attribute the usually-observed 2 fingers to convective transport of brine, which causes recirculation cells (Fig. 4.2). The density differences in the vicinity of the cells can lead to the formation of other fingers while the interactions between neighbouring fingers can cause them to merge at later times. They obtained patterns with one, two or three fingers corresponding to different levels of mesh refinement.

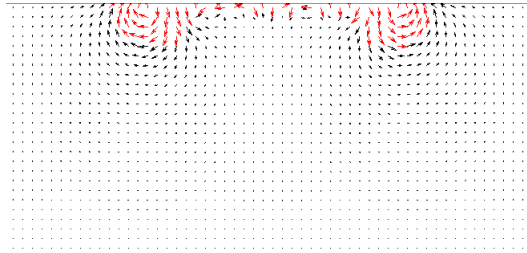


Fig. 4.2 The recirculation cells

In our simulations the number of fingers increased from one to three with increasing density contrast. One finger could be observed for very small density contrasts or after very long times when the fingers merged due to the impervious bottom boundary. The Rayleigh number increases with density contrast (Fig. 4.3) and following the ideas of Johannsen (2002) the system stability can be deduced: the transition from stable to unstable is generally indicated by an increase in the number

of fingers.

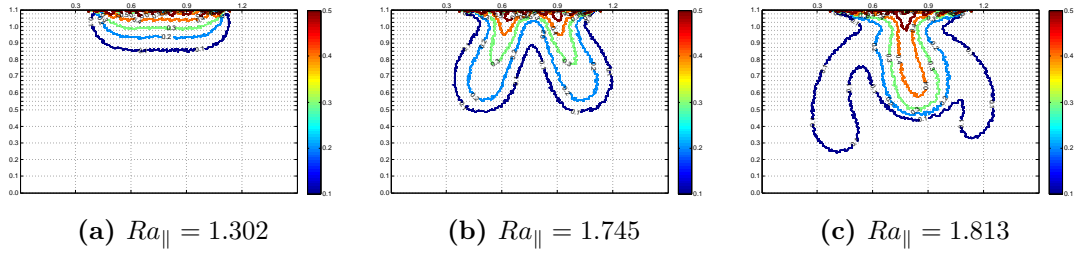


Fig. 4.3 The dependency of the number of fingers on Ra_{\parallel}

The different regimes documented in Diersch and Kolditz (2002) can be incorporated as follows: the small Rayleigh numbers result from very small density contrasts when gravity effects are negligible. Increasing the density results in the formation of two convective cells in which the local velocity vectors change direction as shown in Fig 4.2. The cells can lead to finger formation, which corresponds to the onset of the two-finger regime in simulations. Further increase in density creates stronger recirculation that can lead to formation of additional fingers e.g. the third and possibly more.

Figure 4.4 summarises the previous results from Diersch and Kolditz (2002)[†] and Johannsen (2002)[§] and the application of the two in this work[‡] into a stability criterion that predicts the flow regime (indication of system stability) as a function of the number of fingers formed.

[†] Ra	0	$4\pi^2$	240-300
[†] Regime	Diffusive	Stable convective	Unstable convective
^{†,§,‡} Fingers	1	2	3
[‡] Λ_p^*	$\Lambda_p^* > 0$	$-1.172 < \Lambda_p^* < 0$	$\Lambda_p^* < -1.976$

Fig. 4.4 Relating the previous and current results

The current work concisely predicted the transition from one to two-finger regimes through the change of sign of the stability number but there were some instances where the predicted stability number was positive but there were visible remnants of the second finger in numerical simulations. That overlap is represented with the first hatching in Fig. 4.4. Holzbecher (1998), Diersch and Kolditz (2002) report that the onset of convection can be accurately predicted with the first critical Rayleigh

number $Ra_{cr_1} \approx 4\pi^2$.

The transition from two to three fingers can be clearly shown in numerical simulations but cannot be pinpointed from the stability criterion. The transition with $\Lambda_p^* < 0$ is thus indicated with a gradual colour change from yellow to red. We hypothesise that there is a definite range of Λ_p^* over which the transition occurs and we indicate that with the second hatching in Figure 4.4. Diersch and Kolditz (2002) also reported a wide range of the second critical Rayleigh numbers ($240 < Ra_{cr_2} < 300$) over which the second transition occurred.

4.2.1 Determination of the Critical Wavelength

This section presents the simulations performed at the reference parameters with varying wavelengths of the perturbing sinus function to estimate the cutoff wavelength. The two fingers were always observed for $\lambda \leq 1.0 \times 10^{-3}m$ (Fig. 4.5a) but a third appeared at $\lambda = 2.0 \times 10^{-3}m$ (Fig. 4.5b) and more appeared at bigger wavelengths e.g. $\lambda = 4.0 \times 10^{-3}m$ in Fig. 4.5c.

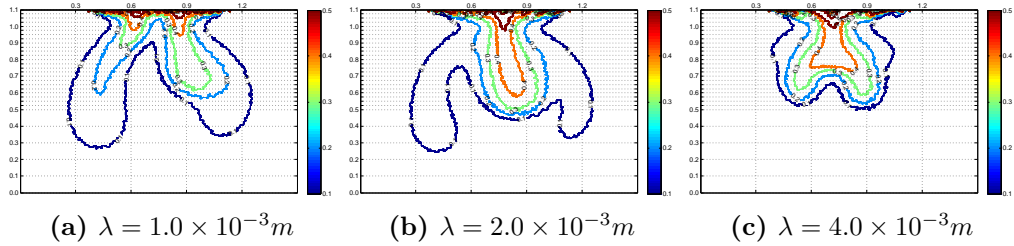


Fig. 4.5 Estimation of the critical wavelength

Following the foregoing discussion $\lambda = 2.0 \times 10^{-3}m$ was adopted as the reference wavelength. Attempts will be made in the subsequent analyses to increase stabilising variables at that perturbation wavelength so as to smooth out the third finger. That would mean shifting the system from the unstable into the stable-convective regime.

4.2.2 Derivation and Testing of the Proposed Mixing Zone Width

In this section the proposed expression for the width of the mixing zone is derived and tested. An attempt was made to capture the transition from one to two fingers i.e. the onset of convection. The density contrast was therefore reduced to 998.35 kgm^{-3} , at which two fingers were first observed.

The procedure outlined in section 4.1.2 to estimate m was followed. Figures 4.6a and 4.6b are for varying α_{\parallel} and α_{\perp} respectively while the red and blue parts of the curves indicate the regions corresponding to $\Lambda_p^* < 0$ and $\Lambda_p^* > 0$ respectively.

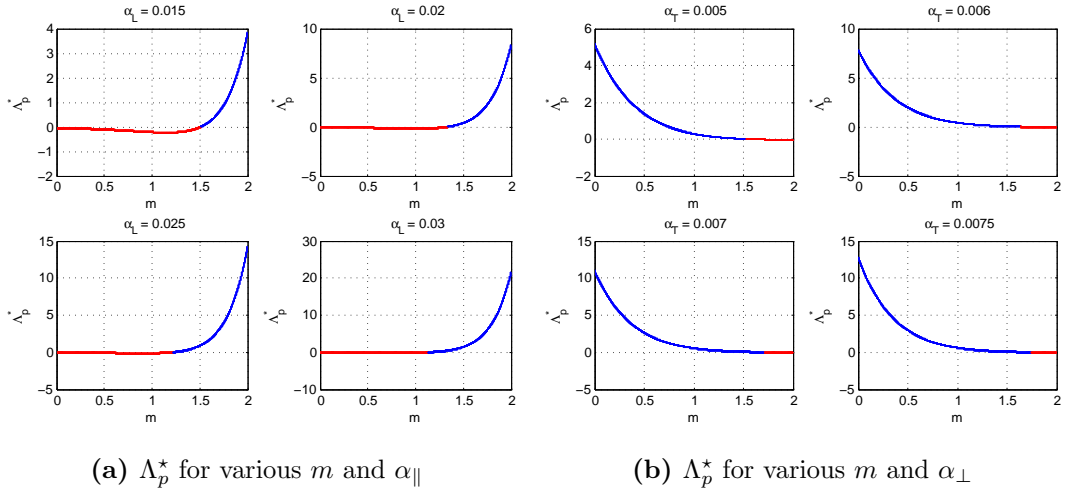


Fig. 4.6 Fitting the proposed dispersion zone width

The sub-plots in Fig. 4.6a satisfy the condition $\Lambda_p^* > 0$ for $m \geq 1.49$ while in Fig. 4.6b the condition is satisfied for $m \leq 1.51$. Intersecting the two regions gives $m \approx 1.5$. Figure 4.6b additionally shows that α_{\perp} in (4.10) has a negative index, which is physically consistent because the longitudinal mixing zone reduces as the transverse dispersivity increases.

Figures 4.7 and 4.8 show the simulations at the parameter sets used in Fig. 4.6. The transition from two to one finger is captured reasonably well. With $m = \frac{3}{2}$ and $n = -\frac{1}{2}$, the approximate mean displacement from (4.10) becomes

$$X = \alpha_{\parallel}^{\frac{3}{2}} \alpha_{\perp}^{-\frac{1}{2}}. \quad (4.13)$$

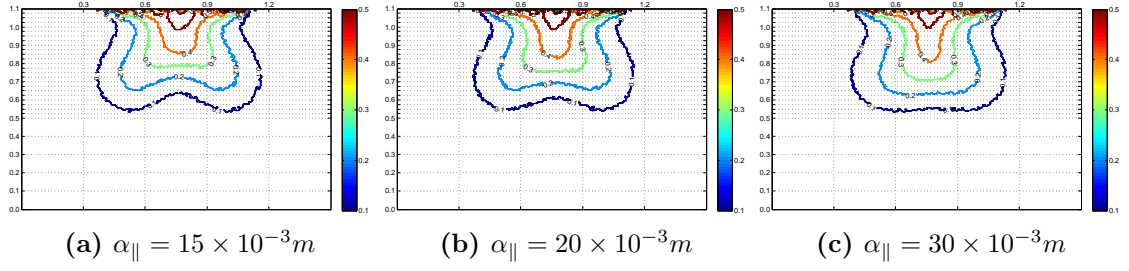


Fig. 4.7 α_{\parallel} for Figure 4.6a

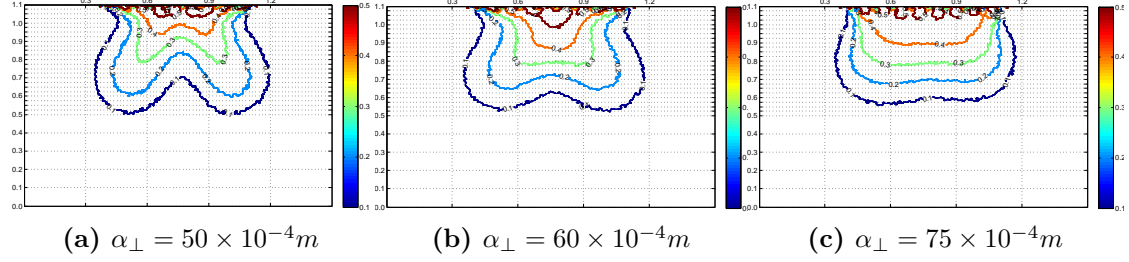


Fig. 4.8 α_{\perp} for Figure 4.6b

The width of the mixing zone consequently becomes

$$\zeta = \left(\frac{\alpha_{\parallel}^5}{\alpha_{\perp}} \right)^{\frac{1}{4}}. \quad (4.14)$$

The new stability number from (4.6) and (4.12) then becomes:

$$\Lambda_p^* := Ra_{\parallel} \left(\frac{2\alpha - \beta}{\alpha} \right) + \frac{\alpha_{\parallel}^{\frac{3}{2}} \alpha_{\perp}^{\frac{1}{2}}}{\lambda^2}. \quad (4.15)$$

To test the validity of (4.15) the dispersivities therein were varied in such a way as to preserve their product constant. Table 4.1 shows the stability numbers obtained with $\rho_{max} = 998.5 kg \cdot m^{-3}$, $\lambda = 0.002m$ and various combinations of the dispersivities.

Table 4.1 Testing the dispersion zone width

Dispersivities (m)		Λ_p^*	Figure Number
$\alpha_{\parallel} = 1.5 \times 10^{-3}$	$\alpha_{\perp} = 1.0 \times 10^{-4}$		
α_{\parallel}	α_{\perp}	-1.976	4.9a
$8\alpha_{\parallel}$	$8^{-3} \cdot \alpha_{\perp}$	-1.452	4.9b
$10\alpha_{\parallel}$	$10^{-3} \cdot \alpha_{\perp}$	-1.265	4.9c

The stability numbers increased down the table indicating a shift towards stability.

The numerical computations at the parameters used in the tabulation are shown in Fig. 4.9.

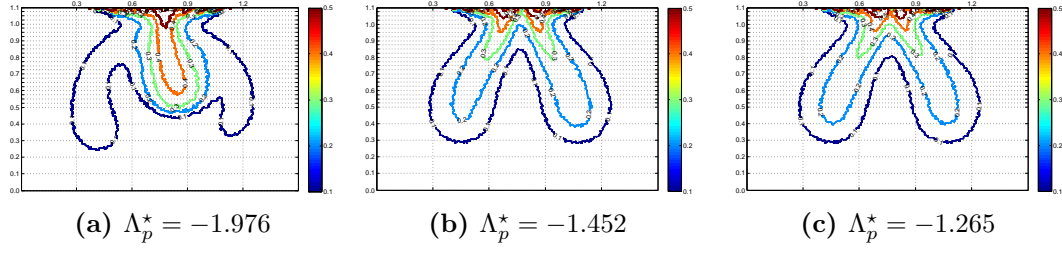


Fig. 4.9 Testing the dispersion width

Figure 4.9a has three fingers which reduce to two in figures 4.9b and 4.9c. The transition from 3 to 2 fingers indicates a shift from an unstable state towards a relatively more stable one. The proposed formulation of the mixing zone could therefore capture the stability transition. With large enough dispersivities, the concentration gradients might be reduced sufficiently so that transport becomes nearly diffusive and a single finger results. However due to the selected domain size, the stability numbers remained negative for all reasonable combinations of α_{\parallel} and α_{\perp} .

4.2.3 Testing the Proposed Criterion

In this section stability numbers are computed using the derived expression (4.15) and numerical simulations performed to test it for density and dispersivity effects.

4.2.3.1 Density Effects

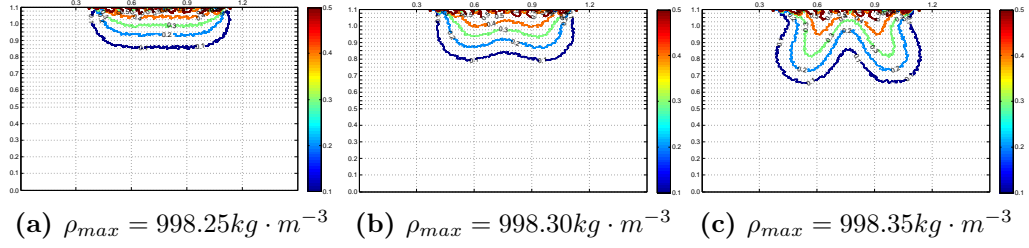
Table 4.2 shows Λ_p^* computed from (4.15) at various density contrasts alongside the old Λ_p with $\alpha_{\parallel} = 1.50 \times 10^{-3}m$, $\lambda = 0.002m$ and $\alpha_{\perp} = 1 \times 10^{-4}m$.

The simulations with only one finger (Fig. 4.10a) and with two not fully developed fingers (Fig. 4.10b) were predicted with positive stability numbers (stable). These cases had very small density contrasts and transport was nearly diffusive.

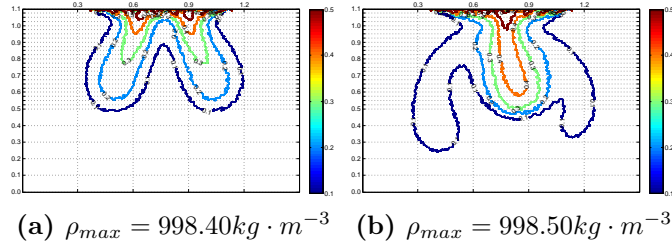
With subsequent density increments, the stability numbers changed sign between

Table 4.2 The new stability numbers for various densities

Max. Density $\rho_{max} (kg \cdot m^{-3})$	Stability Numbers		Figure Number
	Λ_p	Λ_p^*	
998.25	3.881	4.026	4.10a
998.30	0.769	0.914	4.10b
998.35	-0.571	-0.426	4.10c
998.40	-1.317	-1.172	4.11a
998.50	-2.121	-1.976	4.11b

**Fig. 4.10** The onset of convection

$\rho_{max} = 998.30$ and $998.35 kg \cdot m^{-3}$. The transition was matched in numerical simulations with the appearance of two clearly developed fingers (Fig. 4.10c), which physically corresponds to the onset of convection. A further increase in density resulted in more pronounced two fingers that persisted with time (Fig. 4.11a): the stable convective regime in Diersch and Kolditz (2002).

**Fig. 4.11** Fingering at higher densities

High density contrast results in random alterations in the rotation of the local velocity vectors that interact erratically Frolkovič and De Schepper (2001). The interactions give rise to the development of the third finger (Fig. 4.11b) and that corresponds to the onset of the unstable convective regime documented in Diersch and Kolditz (2002).

We have thus reconciled the earlier findings by Johannsen (2002) that the Rayleigh number and the observed number of fingers increase with the density contrast and

by Diersch and Kolditz (2002) regarding the existence of three regimes related to the number of fingers present. In the following, we attempt to stabilise the system in Fig. 4.11b by increasing dispersivities. The stabilising effect is expected to result in a reduction in the number of fingers.

4.2.3.2 Longitudinal Dispersivity Effects

In this section we present the investigations for the effect of α_{\parallel} . Table 4.3 shows the stability numbers computed with different α_{\parallel} at $\lambda = 2 \times 10^{-3}m$, $\alpha_{\perp} = 1.0 \times 10^{-4}m$ and $\rho_{max} = 998.5kg \cdot m^{-3}$.

Table 4.3 The effect of α_{\parallel}

Dispersivity $\alpha_{\parallel} (\times 10^{-3})m$	Stability Number Λ_p^*	Figure number
1.5	-1.976	4.12a
7.5	-1.761	4.12b
10.0	-1.153	4.12c

The criterion predicted an increase in stability with increasing longitudinal dispersivity. Increased stability is due to a reduction in the concentration gradient arising from increased smearing of the solute. Figure 4.12 shows the evolution of fingers at the various α_{\parallel} .

Figure 4.12a is the reference simulation, which is in the unstable convective regime. The increase in stability predicted by the criterion is shown in the reduction of the number of fingers from three to two with increasing dispersivity. The difference in

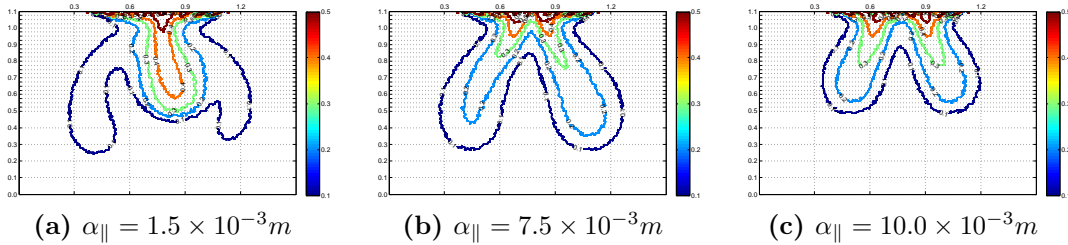


Fig. 4.12 The effect of α_{\parallel}

the distances travelled in figures 4.12b and 4.12b can be accounted for as follows: The rotation of the local velocity vectors inside the recirculation cells (Fig. 4.2) cause

solute transport towards the middle of the front. That results in up-welling (Diersch and Kolditz 2002), which suppressed the middle finger that initially formed. Parts of the two cells merge at later times and cause the middle part of the front to move further down (downwell) at the expense of the outer fingers. Up-welling followed by down-welling were also reported in Frolkovič and De Schepper (2001) and Diersch and Kolditz (2002) and are said to occur at convergent grids only.

4.2.3.3 Transverse Dispersivity Effects

The transverse dispersivity increases mixing in the transverse direction thereby retarding finger growth. Table 4.4 shows the stability numbers computed with different α_{\perp} at $\alpha_{\parallel} = 1.5 \times 10^{-3}m$, $\rho_{max} = 998.5kg \cdot m^{-3}$ and $\lambda = 2 \times 10^{-3}m$.

Table 4.4 The effect of α_{\perp}

Dispersivity $\alpha_{\perp} (\times 10^{-4})m$	Stability Number Λ_p^*	Figure number
1.0	-1.976	4.13a
10.0	-0.734	4.13b
30.0	-0.111	4.13c

The stability numbers predicted an increase in the stability with increasing α_{\perp} . A reduction in the number of fingers was therefore expected. The evolution of fingers for the parameters given above and various α_{\perp} is shown in Fig. 4.13.

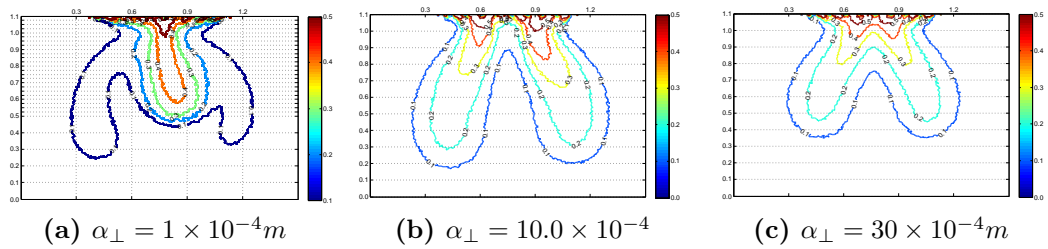


Fig. 4.13 The effect of α_{\perp}

Figure 4.13a has clearly formed three fingers indicating a highly unstable system. The stabilising tendency is shown by the reduction in the number of fingers and the vertical distance travelled by the fingers in figures 4.13b and 4.13c. The vertical distance travelled by the solute front was not significantly affected by the increasing

transverse dispersivity in the first two sub-figures although the enhanced spreading manifested itself in wider outer fingers.

The investigations have shown that the longitudinal dispersivity is more stabilising than the transverse. To capture the effects of the transverse dispersivity it was necessary to increase α_{\perp} beyond α_{\parallel} , which is practically unrealistic. However the proposed criterion predicted the stability transition at the unreasonably high transverse dispersivities.

4.2.4 Discussion of Results

The fingers in figures 4.5a through 4.13c are generally asymmetric, save for very small density contrasts. Asymmetric fingering was documented in Kolditz et al. (1998) and attributed to insufficient grid refinement (numerical errors). However, symmetric patterns could be achieved with the same grid refinement but a different boundary condition. Figure 4.14a shows the symmetric pattern after 2000hrs at $\rho_{max} = 998.7 \text{ kg} \cdot \text{m}^{-3}$ with the unperturbed $\omega = 1.0$ boundary condition while Fig. 4.14b is the asymmetric pattern at identical parameters but a sinus boundary condition.

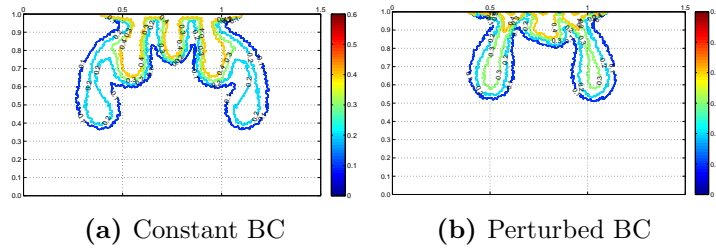


Fig. 4.14 Effect of boundary condition on finger symmetry

The symmetry in Fig. 4.14a indicates sufficient grid refinement ($Pe = 1.4 \times 10^{-2}$). We therefore attribute the asymmetric behaviour in Fig. 4.14b to the boundary condition. Marle (1981) also documented the asymmetric evolution of an interface initially perturbed by symmetric sinusoidal functions while Frolkovič and De Schep- per (2001) showed very big variations in the numerical solution caused by very slight perturbations in the solute initial condition.

Figure 4.14 additionally shows that the concentration front in the unperturbed system travels through a bigger vertical distance. This is due to a reduction in solute mass and hence in the propagation velocity caused by the fluctuating sinus function at the inflow. It is possible that comparable distances are travelled with sufficiently large wavelengths.

The constant inflow boundary condition in Fig. 4.14a corresponds to an infinite perturbation wavelength and the numerous fingers indicate a highly unstable configuration. This is consistent with equation 4.3 on page 61 that stability diminishes with increasing perturbation wavelength.

The proposed stability criterion produced satisfactory results for density and longitudinal dispersivity but was hypersensitive to changes in the transverse dispersivity. We have shown that all simulations with more than one finger were predicted with $\Lambda_p^* < 0$. Considering the predictions from density and longitudinal dispersivity, it appears that the transition from two to three fingers occurred over the range $-1.976 \leq \Lambda_p^* \leq -1.172$.

The stability criterion can be thus stated that predicts the various flow regimes (number of fingers) using the stability numbers:

- I: **1 finger**: nearly diffusive system $\Lambda_p^* > 0$,
- II: **2 fingers**: stable convective system $-1.172 < \Lambda_p^* < 0$,
- III: **3 fingers**: unstable convective system $\Lambda_p^* < -1.976$.

The transition from 2 to 3 fingers occurred over the range $-1.976 < \Lambda_p^* < -1.172$ indicated by the second hatched region in Fig. 4.4 on page 67.

We neglected diffusion and assumed the mixing zone width to be a function of the dispersivities only. This is not entirely true because molecular diffusion is responsible for transport across streamlines, and therefore contributes to the mixing zone. The expression for the mixing zone could be improved by explicitly taking into account the dependency on density (see e.g. Kempers and Haas (1994)) and the contribution from molecular diffusion.

The effects of velocity were not explicitly studied. The flow systems considered here are purely density-driven without external pressures. The velocity effects are therefore implicitly included within the density investigations.

We have shown that α_{\parallel} has a stabilising effect, a fact that is not widely documented. What is available in literature is the uncontrolled mixing resulting from very big longitudinal dispersion coefficients D_{\parallel} (Welty and Gelhar 1991, Held et al. 2005, Landman, Johannsen and Schotting 2007, Landman, Schotting, Egorov and Demidov 2007). The dispersion coefficients in density-driven systems depend on the density contrast (Kempers and Haas 1994, Held et al. 2005) and are therefore a combination of two factors with opposing effects. Kempers and Haas (1994) mention that the destabilising density effects override the stabilising dispersivity thus the widely documented uncontrolled mixing resulting from big dispersion coefficients.

As was the case in chapter 3, the intensity of fingering cannot be precisely inferred from the magnitude of the stability number. This is again the case for the patterns at $\rho_{max} = 998.40$ (Fig. 4.11a on page 72) and $\alpha_{\parallel} = 10.0 \times 10^{-3}$ (Fig. 4.12c on page 73), which are significantly different but predicted with $\Lambda_p^* = -1.176$ and -1.153 respectively. Only the sign of Λ_p^* can indicate whether there is one or more fingers. The magnitude can distinguish between 2 and 3 fingers using the ranges in Fig. 4.4.

For the destabilising density effects, the fingers become thinner and longer in figures 4.10a through 4.11b, while they become broader and shorter for the stabilising effects of longitudinal and transverse dispersivity in Fig. 4.12 and 4.13 respectively. This suggests that in addition to the horizontal plane hypothesised in chapter 3, there might exist a critical finger width demarcating stable and unstable configurations.

The width of the dispersion zone first increases with time then attains an asymptotic value (Marle 1981, Buès and Aachib 1991). Consequently, it is possible that a system that appears unstable at very early times owing to insufficient dispersive mixing becomes stabilised at later times. Therefore it was necessary to let the simulations run for reasonably long times of up to 7000 hours to achieve stationarity in the evolutions.

Chapter 5

Stability Analyses for a Heterogeneous Medium¹

The stability criterion developed and tested in the preceding chapters is extended here to include medium heterogeneity effects. Additionally, the elements in the macrodispersion tensor derived via homogenization theory are derived and presented. Their temporal evolution for various heterogeneity parameters is also evaluated and presented.

5.1 The Stochastic Permeability Field

Deterministic models are of limited value to model natural formations because of the underlying complexity and uncertainty. A stochastic model is used to formalise the uncertainty in space functions by regarding them as random spatial variables characterised statistically (Dagan 1986). A random function is characterised by a joint probability density function *p.d.f.* of its values at arbitrary points and the p.d.f. is characterised by the various moments, the first two being the expected value and the 2-point covariance (Gelhar 1993). The output is only part of the many possible outcomes from all points (Fetter 1999), the ensemble.

¹Manuscript submitted to Advances in Water Resources

The spatially varying permeability field k can be conveniently expressed as a function of the position vector \mathbf{x} by taking the natural logarithm: $f(\mathbf{x}) = \ln k(\mathbf{x})$ where f is the natural log permeability (Gelhar and Axness 1983, Dagan 1988, Welty and Gelhar 1991). $f(\mathbf{x})$ is split into the constant average $\bar{f}(\mathbf{x})$ and randomly fluctuating part $\tilde{f}(\mathbf{x})$ according to $f(\mathbf{x}) = \bar{f}(\mathbf{x}) + \tilde{f}(\mathbf{x})$, which imposes the condition that $\overline{\tilde{f}(\mathbf{x})} = 0$. The over-bar quantity denotes the ensemble average but statistical stationarity enables the use of one realisation to represent the ensemble (Dagan 1987, Gelhar 1993) and infer statistical moments. If the logarithm of the permeability values is normally distributed, the log-normal permeability model is obtained. The model yields a smooth distribution of permeability about the mean value while avoiding the unphysical situation of negative values (Drummond and Horgan 1987, Gelhar 1993).

The stationarity (statistical homogeneity) assumption is usually adopted in stochastic studies (Gelhar and Axness 1983, Dagan 1986; 1988, Welty and Gelhar 1991, Gelhar 1993, Fetter 1999) and asserts that the average permeability is independent of location in the domain and the covariance corresponding to 2 points only depends on the length and orientation of the vector separating the points. If statistical isotropy is further assumed, the covariance is then independent of the vector orientation. As a consequence the covariance of the fluctuations around the mean value only depends on the difference between their arguments.

Heterogeneous fields were generated using the spectral techniques developed by Robin, Gutjahr, Sudicky and Wilson (1993). We assumed the log-normal probability density function, statistical stationarity and isotropy (Dagan 1987; 1988, Schincariol and Schwartz 1990, Schincariol 1998) and a Gaussian auto-covariance function (Held et al. 2005). Such an auto-covariance function in 2 spatial directions reads:

$$w_f(\mathbf{x}) = \sigma_f^2 \exp \left(- \sum_{j=1}^2 \frac{|x_j|^2}{2\lambda_j^2} \right) . \quad (5.1)$$

σ_f^2 is the distribution variance and x_j and λ_j are the respective components of the space vector and correlation length in direction j . For the exponential auto-

covariance function, please see Gelhar and Axness (1983), Dagan (1988), Fetter (1999) and Rubin (2003).

5.2 Stability Analyses in Heterogeneous Media

A stability criterion was derived in chapter 4 for a homogeneous medium including dispersive effects. The effects of dispersion and medium heterogeneity are similar in that they result in the spreading (mixing) of the solute in the domain. The previous analysis can thereby be extended to heterogeneous media with minimal changes.

We take the net medium heterogeneity effect as the effects of the small-scale dispersion occurring over several pores coupled with the large-scale spreading caused by the heterogeneities. To that end, the heterogeneous-medium dispersivity is considered as the effective composed of the local from the homogeneous medium and an increment $\delta(\alpha)$ arising from the medium heterogeneity: $\alpha^{\text{eff}} = \alpha + \delta(\alpha)$. With this, a new stability number $\Lambda_p^{\star\star}$ for a heterogeneous medium can be written as the total of the contributions from the homogeneous medium Λ_p^{\star} and the part from the medium heterogeneity. Substituting α^{eff} in the homogeneous medium stability number

$$\Lambda_p^{\star} := \Lambda_p + \frac{\alpha_{\parallel}^{\frac{3}{2}} \alpha_{\perp}^{\frac{1}{2}}}{\lambda^2} ,$$

one can write: $\Lambda_p^{\star\star} = \Lambda_p + \frac{\alpha_{\parallel}^{\text{eff}\frac{3}{2}} \alpha_{\perp}^{\text{eff}\frac{1}{2}}}{\lambda_v^2}$, which upon further substitution gives

$$\Lambda_p^{\star\star} = \Lambda_p + \frac{[(\alpha_{\parallel} + \delta(\alpha_{\parallel}))^3 (\alpha_{\perp} + \delta(\alpha_{\perp}))]^{\frac{1}{2}}}{\lambda_v^2} . \quad (5.2)$$

The correlation length λ_v plays the role previously played by the perturbation wavelength in the homogeneous medium to filter out instabilities that grow into fingers. The dispersivity terms are then multiplied out and in accordance with the linear

perturbation theory, the products of $\delta(\alpha)$ terms are neglected. We then obtain

$$\Lambda_p^{**} \approx \Lambda_p + \frac{\left(\alpha_{\parallel}^3 \alpha_{\perp} + \alpha_{\parallel}^3 \delta(\alpha_{\perp}) + 3\alpha_{\parallel}^2 \delta(\alpha_{\parallel})\right)^{\frac{1}{2}}}{\lambda_v^2} . \quad (5.3)$$

We now assume that the change of dispersivity in the transverse direction is very small and can be neglected (see also Dagan (1988)) to obtain

$$\Lambda_p^{**} \approx \Lambda_p + \frac{\left(\alpha_{\parallel}^3 \alpha_{\perp}\right)^{\frac{1}{2}}}{\lambda_v^2} \left[1 + 3 \left(\frac{\delta(\alpha_{\parallel})}{\alpha_{\parallel}}\right)\right]^{\frac{1}{2}} . \quad (5.4)$$

Expanding the square bracket as a series up to the linear term gives

$$\Lambda_p^{**} \approx \Lambda_p + \frac{\left(\alpha_{\parallel}^3 \alpha_{\perp}\right)^{\frac{1}{2}}}{\lambda_v^2} + \frac{3\delta(\alpha_{\parallel}) \left(\alpha_{\parallel}^3 \alpha_{\perp}\right)^{\frac{1}{2}}}{2\alpha_{\parallel} \lambda_v^2} . \quad (5.5)$$

At this point we consider a simple linear relationship: $\lambda_v = n\lambda$ relating the heterogeneous medium correlation length and the homogeneous medium perturbation wavelength. The asymptotic longitudinal dispersivity for heterogeneous media is given by $\delta(\alpha_{\parallel}) = \sigma^2 \lambda_v$ (Gelhar and Axness 1983, Gelhar 1993, Kempers and Haas 1994), where σ^2 is the heterogeneity variance. The second term on the right hand side of (5.5) can be rewritten in terms of the homogeneous medium perturbation wavelength consequently allowing the introduction of Λ_p^* . The following expression then results for the new stability number:

$$\Lambda_p^{**} \approx \Lambda_p^* - (n^2 - 1) \frac{\left(\alpha_{\parallel}^3 \alpha_{\perp}\right)^{\frac{1}{2}}}{\lambda_v^2} + \frac{3\sigma^2 \left(\alpha_{\parallel}^3 \alpha_{\perp}\right)^{\frac{1}{2}}}{2\lambda_v} . \quad (5.6)$$

The value of n can be estimated via numerical simulations by varying the correlation length and noting when fingering starts. Equation (5.6) shows that in addition to the dispersivities, σ^2 also stabilises while λ_v destabilises the system.

It should be noted that (5.6) is only meaningful if mixing on the cell problem level is ergodic. This might only happen if the problem on the cell problem level is stable. If the problem is already unstable on the cell-problem level, no stabilisation occurs

due to heterogeneities.

5.2.1 Hypothesis

For homogeneous media, the small-scale problem was stable for perturbation wavelengths smaller than the critical. If diffusion and small-scale dispersion, the main stabilising mechanisms are insufficient to limit the growth of perturbations into fingers, the system becomes unstable at the small scale and the fingers are observed at the large scale as well.

Medium heterogeneities on the other hand control the formation and growth of instabilities. An unstable problem at the small scale might be stable at larger scales if the spreading caused by heterogeneities can arrest the growth of instabilities. In that case, the macroscopic transverse dispersion coefficient exceeds the local dispersion. It is also possible that heterogeneities cannot smooth out the instabilities making unstable small scale systems unstable at the large scales as well.

A third possibility is when the perturbation wavelengths are smaller than the critical thus a stable small scale problem, which in the presence of heterogeneities should also be stable at large scales. However when the heterogeneities are distributed in such a way as to offer preferential flow paths, they can promote finger growth and destabilise systems that were stable at small scales.

The question of whether heterogeneities have stabilising or destabilising effects leads us to the following hypothesis: *within a certain range of density contrasts, increasing σ^2 sufficiently can result into stable behaviour if the correlation length lies in a certain range. In particular, there also exists a critical correlation length $\lambda_{v,crit}$ below which configurations are stable. It might also be that a favourable density contrast in a homogeneous medium leads to fingering in a heterogeneous medium.* From the hypothesis, it is expected that by increasing σ^2 , both the density contrast and $\lambda_{v,crit}$ at which fingering occurs increase.

5.3 Large-scale Mixing in Heterogeneous Media

The small-scale stability criterion in chapter 3 was based on the assumption that velocity fluctuations were caused by the small-scale variations of solute only. The formulations used were general and can be extended to heterogeneous media by incorporating the (previously neglected) heterogeneity effects. The expression for the mesoscale velocity fluctuations is modified in the following to include the contributions from the medium heterogeneity. Held et al. (2005) suggested the following relationship:

$$\tilde{\mathbf{v}}(\mathbf{q}, \tau) = \mathbf{M}(\mathbf{q})\omega_1(\mathbf{q}, \tau) + \mathbf{L}(\mathbf{q})\tilde{k}(\mathbf{q}) . \quad (5.7)$$

Where $\tilde{k}(\mathbf{q})$ is the fluctuation of the log-transformed permeability and $\mathbf{L}(\mathbf{q})$ the contribution of the permeability heterogeneity to the mesoscale velocity fluctuations (see appendix A.2 for derivation). We then obtain the following small-scale equation (in Fourier space)

$$\begin{aligned} \rho(\omega) \frac{\partial \omega_1(\mathbf{q}, \tau)}{\partial \tau} + i \frac{L}{D_{\parallel}} \mathbf{v} \cdot \mathbf{q} \omega_1(\mathbf{q}, \tau) + \mathbf{D}^* \mathbf{q} \cdot \mathbf{q} \omega_1(\mathbf{q}, \tau) \\ = - \frac{L}{D_{\parallel}} \left(\mathbf{M}(\mathbf{q}) \cdot \mathbf{G} \omega_1(\mathbf{q}, \tau) + \mathbf{L}(\mathbf{q}) \tilde{k}(\mathbf{q}) \right) , \end{aligned} \quad (5.8)$$

where i is the imaginary unit $\sqrt{-1}$, \mathbf{v} the total velocity, and \mathbf{G} the large scale concentration gradient.

In order to evaluate the elements in the macrodispersion tensor, the cell problem has to be written explicitly and solved. First the solution to (5.8), which depends on the large-scale mass fraction is assumed to have the form

$$\omega_1(\mathbf{q}, \tau) = \boldsymbol{\chi}^\omega(\mathbf{q}, \tau) \cdot \mathbf{G} , \quad (5.9)$$

where the vector $\boldsymbol{\chi}^\omega$ is the solute distribution in the reference homogenization theory cell. Substitution of (5.9) into (5.8) gives the cell problem (Held et al. 2005)

$$\rho(\omega) \frac{\partial \chi_n^\omega}{\partial \tau} + i \frac{L}{D_{\parallel}} \mathbf{v} \cdot \mathbf{q} \chi_n^\omega + \mathbf{D}^* \mathbf{q} \cdot \mathbf{q} \chi_n^\omega + \frac{L}{D_{\parallel}} \mathbf{M}(\mathbf{q}) \cdot \mathbf{G} \chi_n^\omega = - \frac{L}{D_{\parallel}} \mathbf{L}(\mathbf{q}) \cdot \mathbf{G} \tilde{k}(\mathbf{q}) , \quad (5.10)$$

with $\chi_n^\omega(\mathbf{q}, \tau)$, $n = 1, 2$. Solving the cell problem with the boundary condition $\chi_n^\omega(0, \tau) = 0$ yields (see also Held et al. (2005)):

$$\begin{aligned} & \chi_n^\omega(\mathbf{q}, \tau) \\ &= -\kappa \int_0^\tau d\tau' L_n(\mathbf{q}) \tilde{k}(\mathbf{q}) \exp \left(- \left(i \frac{L}{\rho(\omega) D_\parallel} \mathbf{v} \cdot \mathbf{q} + \frac{\mathbf{D}^* \mathbf{q} \cdot \mathbf{q}}{\rho(\omega)} + \frac{\Lambda}{\rho(\omega)} \right) \tau' \right) , \end{aligned} \quad (5.11)$$

where Λ is the stability number. Vertical systems are considered here so we adopt Λ_p computed from (3.21). The notation $\kappa = \frac{L G_n}{D_\parallel \rho(\omega)}$ has been introduced to shorten the expression and will be used subsequently.

The large-scale transport equation from homogenization theory (see chapter 3 for derivation) reads

$$\rho(\omega) \frac{\partial \omega_0}{\partial t} + \frac{L}{D_\parallel} \mathbf{v}_0 \cdot \nabla_{\mathbf{x}} \omega_0 - \nabla_{\mathbf{x}} \cdot \mathbf{D}^{\text{eff}} \nabla_{\mathbf{x}} \omega_0 = 0 , \quad (5.12)$$

where the 0 subscript indicates macroscopic quantities and \mathbf{D}^{eff} is the macrodispersion tensor defined as

$$\mathbf{D}^{\text{eff}} = \mathbf{D}^* - \overline{\tilde{\mathbf{v}} \otimes \chi^\omega} . \quad (5.13)$$

In 2 dimensions, the elements of the tensor in (5.13) evaluate to

$$\mathbf{D}^{\text{eff}} = \begin{pmatrix} \rho - \frac{L}{D_\parallel} \overline{\tilde{v}_1 \chi_1^\omega} & -\frac{L}{D_\parallel} \overline{\tilde{v}_1 \chi_2^\omega} \\ -\frac{L}{D_\parallel} \overline{\tilde{v}_2 \chi_1^\omega} & \rho \frac{D_\perp}{D_\parallel} - \frac{L}{D_\parallel} \overline{\tilde{v}_2 \chi_2^\omega} \end{pmatrix} . \quad (5.14)$$

5.3.1 Macrodispersion Coefficients for Flow Parallel to Gravity

In this section the expressions used to compute the respective entries in the macrodispersion tensor are presented. The full derivations are given in appendix A.3. We consider vertical flow with $v_1 = v_0$ aligned parallel to the gravity vector and no flow in the transverse direction i.e. $v_2 = 0$. $\mathbf{L}(\mathbf{q})$ (see appendix A.2 for derivation) then becomes

$$\mathbf{L}(\mathbf{q}) = \begin{pmatrix} L_1(\mathbf{q}) \\ L_2(\mathbf{q}) \end{pmatrix} = \frac{1}{\bar{k}} \begin{pmatrix} 1 \\ \frac{1}{q_1^2 + q_2^2} \end{pmatrix} \begin{pmatrix} q_2^2 v_0 \\ -q_1 q_2 v_0 \end{pmatrix}. \quad (5.15)$$

The appropriate components of $\mathbf{L}(\mathbf{q})$ from (5.15) have to be substituted into (5.11).

5.3.1.1 The Diagonal Elements

The longitudinal macrodispersion coefficients (see appendix A.3.1 for derivation) takes the form

$$D_{11}^{\text{eff}} = \Theta \int_s^\infty d\eta \int_0^\infty ds \frac{3\pi}{4\kappa^3(\xi^2 + \eta)^{5/2}} \cdot \left[A \left(2\Lambda_p^2(1 + \eta)(2\text{erf}(C) - \text{erf}(B) - \text{erf}(D)) + \kappa^2(2\Lambda_p\tau(\text{erf}(C) - \text{erf}(D)) + \text{erf}(C) - \text{erf}(B)) \right) - 2\Lambda_p\kappa\sqrt{(1 + \eta)}(1 - 2F + G) \right]. \quad (5.16)$$

Where,

$$\begin{aligned} A &= \sqrt{\pi} \exp\left(\frac{\Lambda_p^2(1 + \eta)}{\kappa^2}\right), & B &= \frac{\Lambda_p\sqrt{1 + \eta}}{\kappa}, & \Theta &= \frac{4\pi\kappa\varepsilon_1\xi v_0\sigma_f^2}{\bar{k}^2}, \\ C &= \left(\frac{(\tau\kappa^2 + 2\Lambda_p + 2\Lambda_p\eta)}{2\kappa\sqrt{(1 + \eta)}}\right), & D &= \frac{\Lambda_p\eta + \tau\kappa^2 + \Lambda_p}{\kappa\sqrt{1 + \eta}}, & \kappa &= \frac{LG_n}{D_{\parallel\rho}}, \\ F &= \exp\left(-\frac{\tau(\tau\kappa^2 + 4\Lambda_p + 4\Lambda_p\eta)}{4(1 + \eta)}\right) \text{ and } & G &= \exp\left(-\frac{\tau(\tau\kappa^2 + 2\Lambda_p + 2\Lambda_p\eta)}{1 + \eta}\right) \end{aligned}$$

The transverse macrodispersion coefficient (evaluated in appendix A.3.2) takes the form

$$\begin{aligned} D_{22}^{\text{eff}} &= \Theta \int_s^\infty d\eta \int_0^\infty ds \frac{\pi}{4\kappa^5(\xi^2 + \eta)^{3/2}(1 + \eta)^{3/2}} \\ &\times \left\{ A^* 2\Lambda_p^2(\eta + 1) \left[2\Lambda_p^2(\eta + 1)(\text{erf}(D) - 2\text{erf}(C) + \text{erf}(B)) \right. \right. \\ &\quad \left. \left. + \kappa^2((\tau\Lambda_p + 1)\text{erf}(D) - (2\tau\Lambda_p + 5)\text{erf}(C) + 3\text{erf}(B)) \right] \right. \\ &\quad \left. + 2\Lambda_p\kappa(\eta + 1) \left[2\Lambda_p^2(\eta + 1)(G - 2F + 1) \right. \right. \\ &\quad \left. \left. + \kappa^2(G - 3F + 2) \right] + \kappa^5\tau F \right\}, \quad (5.17) \end{aligned}$$

where in addition to the above definitions, $A^* = A\sqrt{1+\eta}$.

5.3.1.2 The Off-diagonal Elements

The off-diagonal elements evaluate to zero (see appendix A.3.3), resulting in a symmetric macrodispersion tensor.

There are no closed-form analytical solutions for (5.16) and (5.17), therefore the equations had to be solved numerically using **MAPLE**[®].

5.3.2 The Temporal Evolution of the Coefficients

In this section we present the temporal evolution of the macrodispersion coefficients computed by evaluating the integrals in (5.16) and (5.17) using the software **MAPLE**[®]. First we consider a system without density and viscosity contrasts and compare the results to those found in literature. We then include favourable and unfavourable density and viscosity contrasts and compare the results to what is expected from physical considerations.

5.3.2.1 Macrodispersion Coefficients without Density Effects.

Passive tracer scenarios were achieved by using $\Lambda_p = 0$ in (5.16) and (5.17). Figure 5.1 shows the evolutions of the dispersion coefficients for such tracers at different anisotropy ratios, defined as $\xi = \lambda_h/\lambda_v$, where λ_h and λ_v are respectively the horizontal and vertical correlation lengths. For the longitudinal coefficients plotted in Fig. 5.1a, there is a remarkable reduction in magnitude with increasing anisotropy ratio. However, the transverse coefficients in Fig. 5.1b show no observable change.

The anisotropy ξ was increased by decreasing the vertical correlation length. Small vertical correlation lengths make the medium very heterogeneous in the vertical direction, which impedes vertical transport. The reduced transport in turn reduces dispersion and thus the smaller longitudinal coefficients.

Dagan (1988) considered flow orthogonal to gravity for a passive tracer and defined

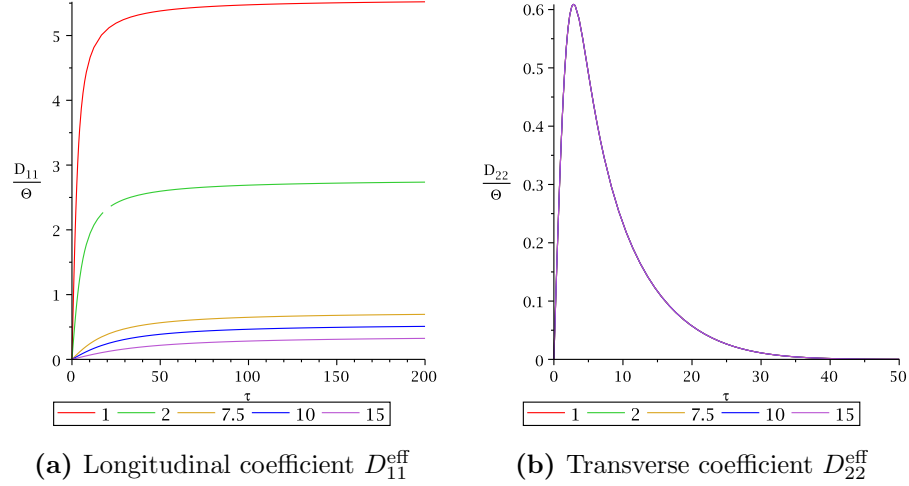


Fig. 5.1 Macrodispersion coefficients for passive tracers

the anisotropy ratio as $\xi^* = \lambda_v / \lambda_h$. He presented longitudinal (in our case the transverse) coefficients that were unaffected by ξ^* and the transverse (in our case the longitudinal) coefficients that increased with increasing ξ^* . Due to the inverse relationship between ξ and ξ^* , our results are in agreement with his. He also presented for his configuration longitudinal dispersion coefficients that vanished to zero after long times, which is again consistent with those in Fig. 5.1b.

5.3.2.2 Macrodispersion Coefficients with Density Effects.

In this section we consider favourable and unfavourable density contrasts and compute the corresponding macrodispersion coefficients and study their temporal evolution.

Favourable Density and Viscosity Contrasts

A stabilised system can be as a result of very small density contrasts or increased transverse mixing. A reduction in density contrast reduces the downward plume propagation and hence the longitudinal dispersion. Increased heterogeneity and/or transverse dispersivity on the other hand increase transverse spreading thus increasing transverse dispersion. We therefore expect the combined effect of a stabilised system to be a reduction and an increase in the longitudinal and transverse macrodis-

persion coefficients respectively.

Figure 5.2 shows the evolution of the longitudinal and transverse macrodispersion coefficients for various arbitrarily chosen positive stability numbers (stable density contrasts).

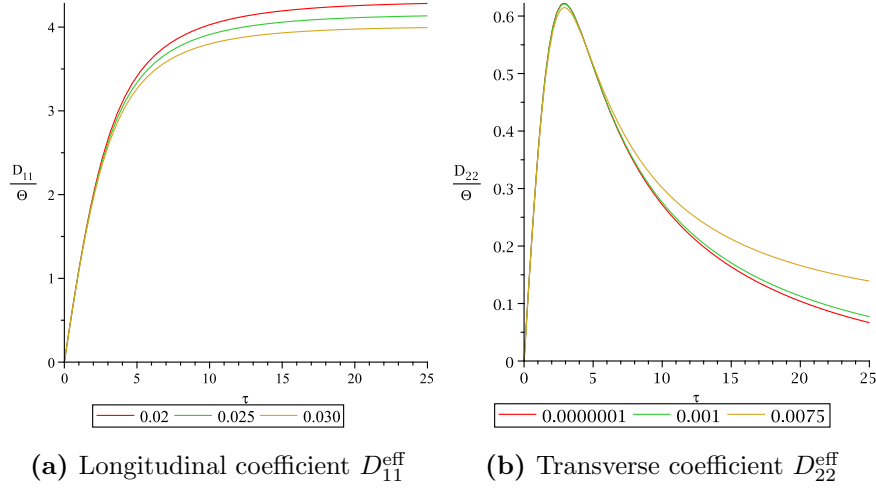


Fig. 5.2 Coefficients for favourable density and viscosity contrasts

As expected, the longitudinal coefficient reduces with stability while the transverse coefficient increases.

Unfavourable Density and Viscosity Contrasts

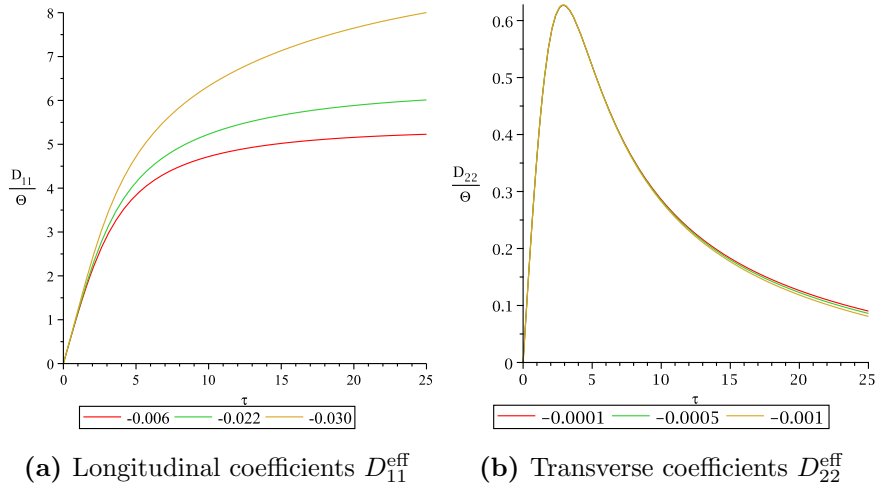
A destabilised system can be achieved by opposite effects to those mentioned above: an increase in density contrast, reduction in transverse dispersivity or a decrease in medium heterogeneity. These cause a respective reduction and increase in the transverse and longitudinal macrodispersions. In the following we present the evolution of the dispersion coefficients for various unstable density contrasts, permeability heterogeneity variance, vertical correlation lengths, dispersivity and medium anisotropy.

Macrodispersion Coefficients for Different Λ_p .

Small variations in density contrast were shown to have big effects on stability in chapter 3. We use various $\Lambda_p < 0$ to compute the dispersion coefficients and attempt

to infer the system stability from the temporal evolution and boundedness of the longitudinal coefficient.

Figure 5.3 shows such evolutions for different values of Λ_p computed using the parameters from Schincariol et al. (1994) in an isotropic medium. Figure 5.3a is the longitudinal coefficient that increases as Λ_p decreases (increase in density contrast) while Fig. 5.3b is the transverse coefficient which decreases marginally with decreasing Λ_p . Systems with $\Lambda_p \ll 0$ have high energy that successively becomes harder to dissipate. Gravity effects predominate over mixing and the longitudinal coefficient grows uncontrollably.



(a) Longitudinal coefficients D_{11}^{eff} (b) Transverse coefficients D_{22}^{eff}
Fig. 5.3 Coefficients for unfavourable density and viscosity contrasts

In Fig. 5.3a the heterogeneities stabilised the system at $\Lambda_p = -0.006$ (red curve) as shown from the asymptotic behaviour. Subsequent increments in density resulted in steeper curves until $\Lambda_p = -0.03$, when the growth became unlimited. Mixing from the prevailing heterogeneity was then insufficient to prevent fingering. Therefore density contrasts with asymptotic (finite) D_{11}^{eff} had been stabilised by medium heterogeneity while those showing infinite growth of the coefficient remained unstable. Comparable results can be found in Welty and Gelhar (1991) but unlike here, the coefficients grew indefinitely with time for all $\Lambda_p < 0$ and boundedness was only for $\Lambda_p \geq 0$.

Longitudinal Coefficients for Different λ_v .

The pre-factor Θ in (5.16) can be modified such that $\Theta = \lambda_v \Theta^*$. We then expect longitudinal coefficients that increase with λ_v . That is physically meaningful because increasing λ_v reduces the vertical heterogeneity and enhances solute transport in the vertical direction, hence bigger longitudinal coefficients. Figure 5.4 shows the evolution of the longitudinal coefficient at $\Lambda_p = -0.006$ and arbitrary λ_v values.

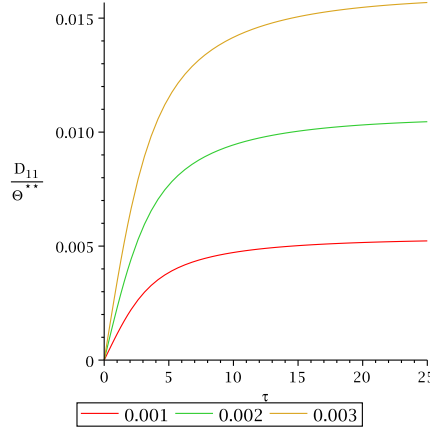


Fig. 5.4 D_{11}^{eff} for various λ_v

Variations in λ_v shifted the curves upwards, increased the slopes of the curves and shifted the time required to reach equilibrium to the right but the asymptotic behaviour almost persisted. It was shown in figures 5.2a and 5.3a that an upward shift and increased slope of the longitudinal coefficient indicate reduced system stability. Very large correlation lengths might cause the unbounded coefficients obtained with density but the restrictions by the computing infrastructure never permitted that to be realised. The shift of the time-to-equilibrium to the right is due to instabilities with big amplitudes requiring longer times to be smoothed out.

Transverse Coefficients for Different σ^2 .

It was mentioned previously that increasing variance means including more heterogeneities in the distribution and results in a more heterogeneous medium. High heterogeneity enhances mixing which shifts the instability wavelengths towards the stable range. We therefore expect the stability of the large-scale system to increase

with σ^2 .

If the pre-factor in (5.17) is modified such that $\Theta = \Theta^{**}\sigma^2$ we obtain a transverse macrodispersion coefficient shown in Fig. 5.5 that increases with σ^2 . It was demonstrated in Fig. 5.2b that an upward shift in the transverse dispersion coefficient indicates increased system stability, thus the stabilising effect of σ^2 is captured in a way consistent with physical expectations.

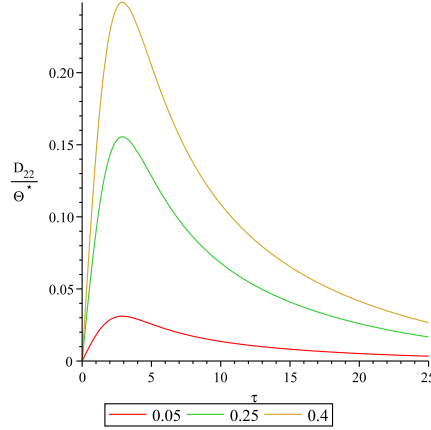
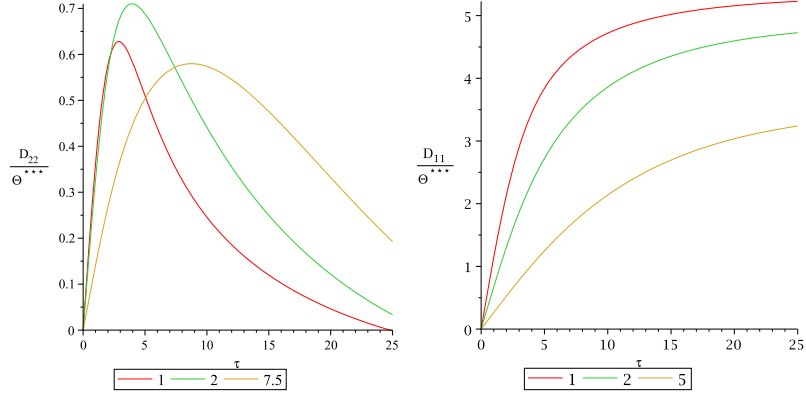


Fig. 5.5 D_{22}^{eff} for various σ^2

Macrodispersion Coefficients for Different ξ .

The anisotropy ξ was defined as the ratio of correlation lengths λ_h/λ_v . Increasing ξ can arise from either increasing λ_h or decreasing λ_v . The medium would respectively become more homogeneous in the horizontal direction (increased D_{22}^{eff}) or more heterogeneous in the vertical direction (reduced D_{11}^{eff}).

If the pre-factor in (5.17) is modified such that $\Theta = \xi\Theta^{***}$, a transverse coefficient that increases with ξ is obtained. Figure 5.6a shows such transverse coefficients that capture the enhanced stability. Figure 5.6b also shows a D_{11}^{eff} that reduces with ξ , thus also capturing the practical phenomenon. A long time should however be considered for D_{22}^{eff} .



(a) Transverse coefficient D_{22}^{eff} (b) Longitudinal coefficient D_{11}^{eff}

Fig. 5.6 Macrodispersion coefficients for various ξ

Finite Péclet numbers.

The foregoing results were obtained on the assumption of infinite Péclet numbers, which made the term containing the dispersivities vanish to zero. Studying the effect of dispersivity on the evolution of the coefficient required the relaxation of that assumption to use finite Péclet numbers. That could however not be done with the available computing resources.

5.4 Numerical Stability Analysis Results

The stability numbers computed from the proposed expression for Λ_p^{**} are presented in this section and compared against numerical simulations. The investigations are limited to a downward vertical displacement of a less dense fluid by a denser one (Fig. 2.9).

For the case of a homogeneous medium with dispersion, the transition between different regimes could be predicted from the magnitude of the stability number. The regimes were the *nearly diffusive* with one finger and predicted with a positive stability number, the *stable-convective* regime with two fingers predicted with $-1.172 < \Lambda_p^* < 0$ and the *unstable-convective* regime with three fingers predicted with $\Lambda_p^* < -1.976$. The interest here is the transition from two to three fingers. The

stabilisation from medium heterogeneity is expected to increase the density contrasts at which fingers appear. That in effect shifts the two-to-three-finger transition zone to the right i.e. towards smaller stability numbers.

It is not necessary to perturb the inflow region as was done in chapter 4 because the medium heterogeneities accomplish the task of initiating perturbations. The relative mass fraction $\omega = 1.0$ is used as the transport equation Dirichlet boundary condition at the inflow region. It is defined as ω/ω_{max} but we simply refer to it as *mass fraction* without loss of generality.

The software package d^3f (Fein and Schneider 1999) was still used for the numerical simulations with 831488 elements and a time step of 0.125 hours. These fine grid and time steps ($Pe \approx 1.4 \times 10^{-4}$ and $Cr \approx 3.2 \times 10^{-6}$) ensured stability of the numerical solution without upwind (Frolkovič 1998b, Frolkovič and De Schepper 2001).

The parameters used in the simulations are given in Table 2.1, the same adopted from Schincariol et al. (1997). The maximal density, domain length and dispersivities used in chapter 4 were again used here.

5.4.1 Relation Between λ and λ_v : Effects of the Correlation Length

To fully develop the stability number, the n in (5.6) needs to be estimated. For that, simulations were performed at various λ_v and σ^2 to determine when fingers first formed (see similar procedure for λ_{crit} in chapter 4). The results are shown in figures 5.7 through 5.9 .

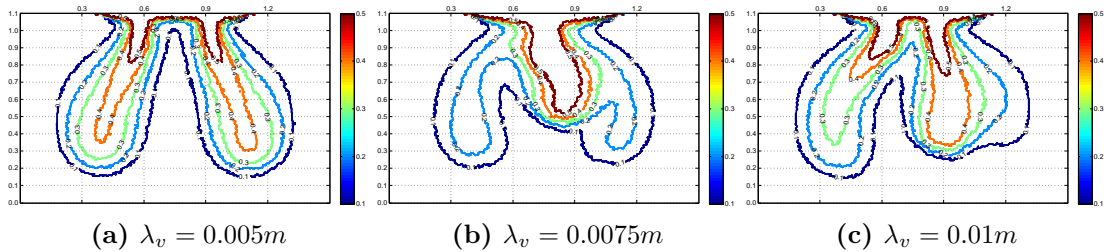


Fig. 5.7 Different λ_v , $\sigma^2 = 0.30$ and $\rho_{max} = 998.5 \text{ kg} \cdot \text{m}^{-3}$

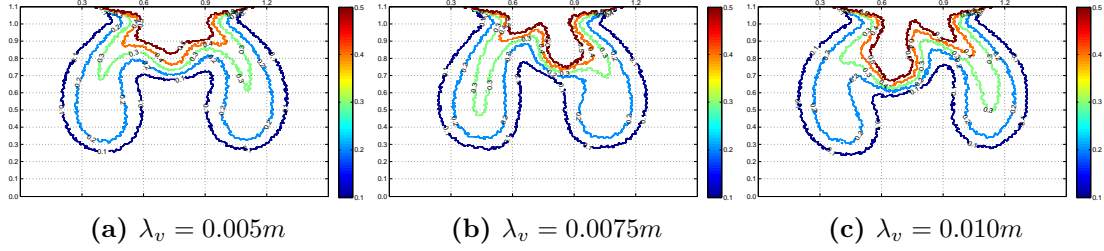


Fig. 5.8 Different λ_v , $\sigma^2 = 0.40$ and $\rho_{max} = 998.5 \text{ kg} \cdot \text{m}^{-3}$

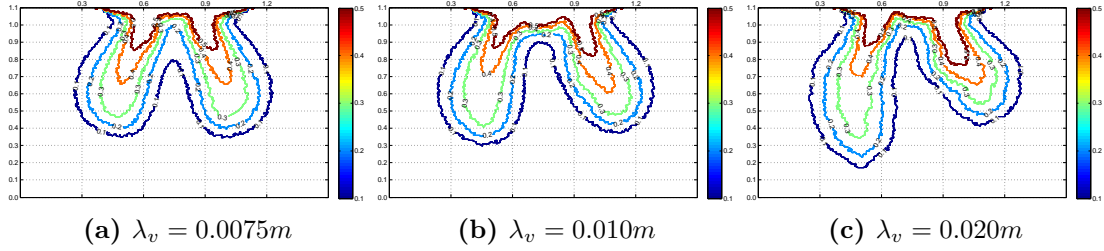


Fig. 5.9 Different λ_v , $\sigma^2 = 0.50$ and $\rho_{max} = 998.5 \text{ kg} \cdot \text{m}^{-3}$

From the figures, $\lambda_v = 7.5 \times 10^{-3}m$ was the smallest correlation length at which the third finger appeared, marking the transition into the unstable-convective regime. Analogous to the work for the homogeneous medium, that is taken as the critical correlation length resulting in the relation $\lambda_v \approx 3.5\lambda$. Increasing the medium heterogeneity requires bigger correlation lengths to offset the mixing, as shown in figures 5.8 and 5.9. Table 5.1 shows the stability numbers computed using (5.6) with $n = 3.5$, the highlighting indicates stability transition from 2 to 3 fingers.

Table 5.1 Effect of λ_v

$\lambda_v (\times 10^{-3})$ m	σ^2		
	0.30	0.40	0.50
5.0	-1.529	-1.441	-1.363
7.5	-1.859	-1.819	-1.785
10.0	-1.975	-1.952	-1.930
20.0	-2.083	-2.079	-2.079

The decreasing stability numbers down the columns in Table 5.1 correctly matched the stability transition in the figures. The simulation in Fig. 5.9 did not return a third finger but rather a distortion in finger symmetry due to channelling effects and therefore an indication of instability. The transition to three fingers suggests that if the correlation length could be sufficiently reduced, heterogeneous mixing could be

so much that no convection would take place and one finger would result. However, resolving such small heterogeneities was not possible with the available computing infrastructure.

5.4.2 Density Effects

The effect of density contrast is investigated next by estimating the density contrast required to induce fingering at different degrees of medium heterogeneity. Table 5.2 shows the stability numbers computed at $\lambda_v = 7.0 \times 10^{-3}m$ and various maximal densities and σ^2 . The correlation length was chosen slightly smaller than the smallest critical obtained in the previous section to avoid unstable starting configurations.

Table 5.2 Density effects

ρ_{max}	σ^2		
	0.40	0.60	0.65
998.4	-0.967	-0.893	-0.877
998.5	-1.771	-1.699	-1.682
998.6	-2.200	-2.125	-2.108
998.7	-2.467	-2.397	-2.375

The evolution of fingers at the same parameters and maximal densities up to the onset of fingering are shown in figures 5.10 through 5.12. The stabilising effect of medium heterogeneity is shown by the increased density contrasts required to induce fingering at high variances.

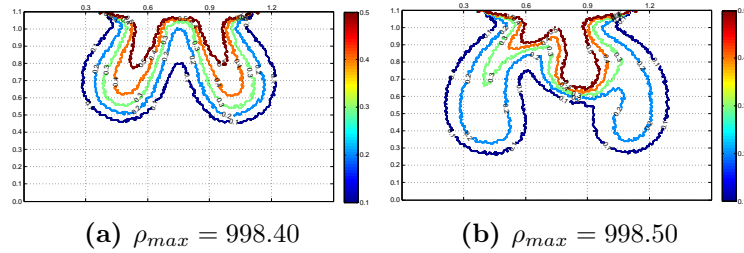


Fig. 5.10 Onset of fingering at $\sigma^2 = 0.40$

A density of 998.5 resulted in three fingers in a homogeneous medium (previous chapter) whereas only two are formed here when $\sigma^2 \geq 0.6$. At $\rho_{max} = 998.6$ a

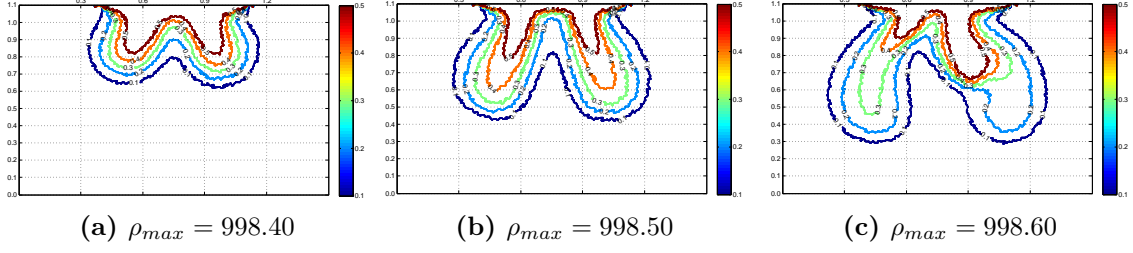


Fig. 5.11 Onset of fingering at $\sigma^2 = 0.60$

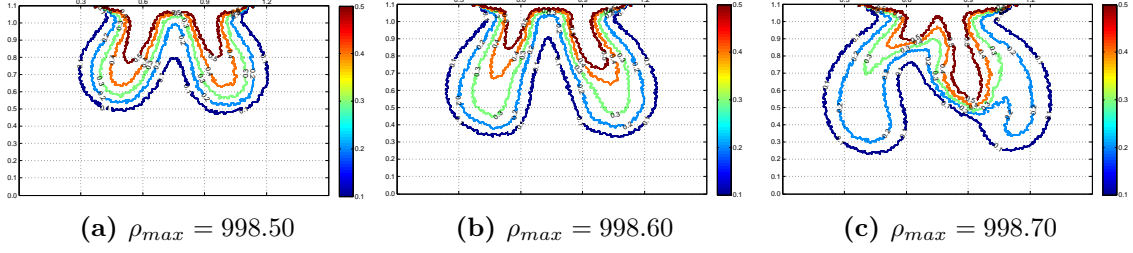


Fig. 5.12 Onset of fingering at $\sigma^2 = 0.65$

third finger just begins to form at $\sigma^2 = 0.60$ in Fig. 5.11c and does not form at all at $\sigma^2 = 0.65$ in Fig. 5.12b. The two fingers at $\rho_{max} = 998.4$ are also significantly stunted compared to what they were in the homogeneous medium. The increase in density contrast required to produce three fingers is an indication of stabilisation by medium heterogeneity.

5.4.3 Medium Heterogeneity Effects

The effects of varying the medium heterogeneity at a fixed density contrast are presented in this section. The heterogeneity variance increases transverse mixing and hence stabilises while anisotropy in the form defined here also stabilises. The vertical correlation length increases the homogeneity of the medium and was already shown to destabilise beyond a certain cutoff.

5.4.3.1 Effects of σ^2

Table 5.3 shows the stability numbers computed at the reference parameters in Table 2.1 and $\lambda_v = 7.5 \times 10^{-3}$ with various σ^2 . The stabilising effect of the medium

heterogeneity is indicated by the increasing stability numbers.

Table 5.3 Effect of σ^2

σ^2	Λ_p^{**}
0.40	-2.200
0.60	-2.125
0.65	-2.108

Figure 5.13 shows the evolution of fingers at the σ^2 in Table 5.3. The increase in stability is indicated by the middle finger in Fig. 5.13a that is smoothed out at higher σ^2 in Fig. 5.13c and the difference in the vertical distances travelled by the solute.

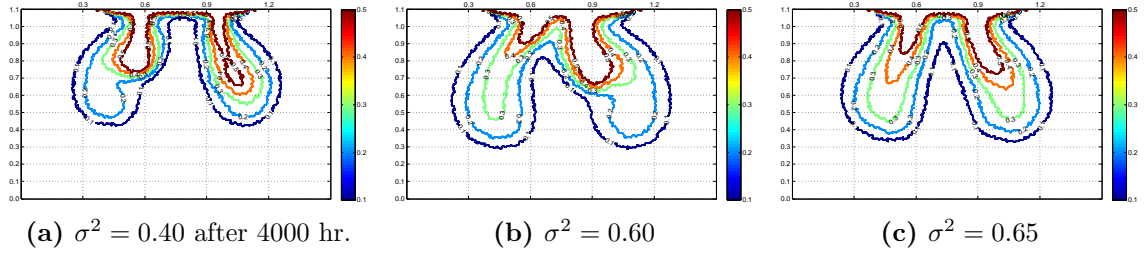


Fig. 5.13 The effect of increasing σ^2

The simulation at $\sigma^2 = 0.4$ is reported at an early time because after 7000 hours when other are taken, the fingers are already recombined into two. Even with a much bigger vertical distance, the misconception that a less heterogeneous medium was more stable had to be avoided.

5.4.3.2 Effect of the Medium Anisotropy ξ

The anisotropy ratio was defined as $\xi = \lambda_h/\lambda_v$. Increase in ξ was achieved by decreasing the vertical correlation length while the horizontal was kept constant. The increased medium heterogeneity in the vertical direction retards the advance of the front and dissipates the energy of the instabilities through spreading/mixing effects and thus results in a stabilised system.

Below are simulations at $\rho_{max} = 998.5 kg \cdot m^{-3}$, $\sigma^2 = 0.40$, $\lambda_h = 0.0075m$ and various λ_v so as to result in the respective ξ . The horizontal correlation length was

maintained at the constant value to achieve a system close to the transition point.

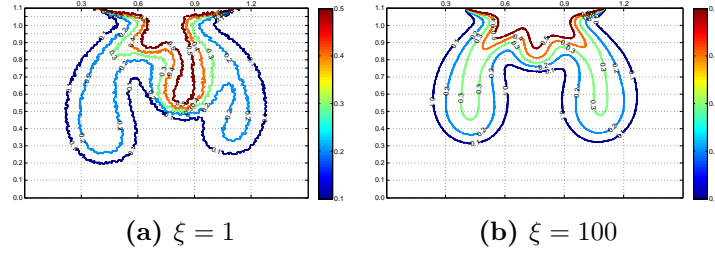


Fig. 5.14 The effect of ξ at $\sigma^2 = 0.40$

No stability numbers could be computed because the criterion does not explicitly contain the medium anisotropy. The stabilising effect of increasing ξ was however captured by the macrodispersion coefficients in Fig. 5.6 on page 93.

5.4.4 Effect of Dispersivity

In this section we present the effect of varying α_{\parallel} and α_{\perp} on flow stability.

5.4.4.1 Effect of the Longitudinal Dispersivity α_{\parallel} .

The results of varying the longitudinal dispersivity at the reference parameters, $\sigma^2 = 0.60$, $\rho_{max} = 998.6$, $\lambda_v = 0.0075$ and various α_{\parallel} are presented here. Table 5.4 shows the stability numbers, with a gradual increase indicating increased stability.

Table 5.4 Effect of α_{\parallel}

$\alpha_{\parallel} \times 10^{-3}m$	Λ_p^{**}
1.5	-2.180
7.5	-2.098
10.0	-1.751

The simulations show three fingers at first, which reduce to two at higher dispersivity.

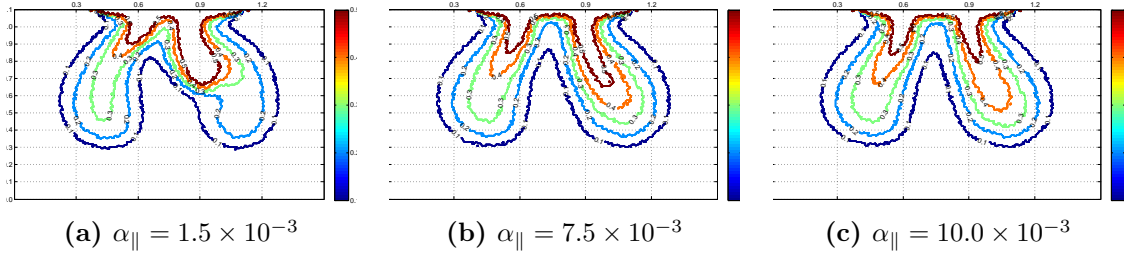


Fig. 5.15 The effect of α_{\parallel} in a heterogeneous medium

5.4.4.2 Effect of Transverse Dispersivity α_{\perp} .

In this section the effect of varying α_{\perp} at $\sigma^2 = 0.6$, $\rho_{max} = 998.6$, $\lambda_v = 0.0075$ and $\alpha_{\parallel} = 1.5 \times 10^{-3}$ are presented. Table 5.5 shows the stability numbers and Fig. 5.16 the simulations at the same parameters. The increase in stability is shown by the increase in the stability numbers and the transition from three to two fingers respectively.

Table 5.5 Effect of α_{\perp}

$\alpha_{\perp} (\times 10^{-4})m$	Λ_p^{**}
1.0	-2.180
5.0	-0.881
10.0	-0.269

The criterion is very sensitive to changes in the transverse dispersivity, as was already noted for the homogeneous medium. It predicted the last entry in the table with a very big number while the simulations still showed strong convection. That was wrong.

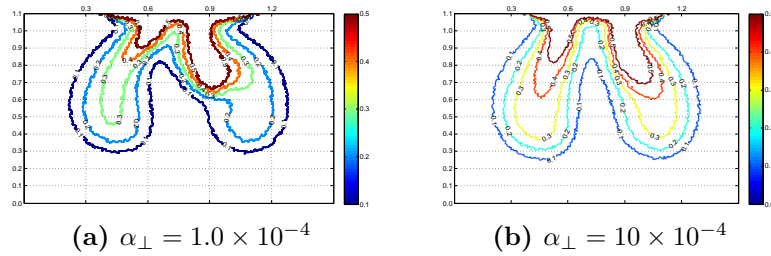


Fig. 5.16 The effect of α_{\perp} in a heterogeneous medium

Apart from the transverse dispersivity, the remainder of the variables showed the transition from two to three fingers over the range $-2.3725 < \Lambda_p^{**} < 2.1252$.

5.4.5 Discussion of Results

We used the expressions derived previously to evaluate the macrodispersion tensor elements for vertically downward density-driven flow. We obtained a symmetric tensor with zero off-diagonal elements. By turning off the density and viscosity contrast terms, we “emulated” passive tracers and our results compared well to those found in literature. The longitudinal coefficient showed scale dependency (asymptotic behaviour) and also reduced with increasing medium anisotropy while the transverse coefficient was not affected by anisotropy changes but reduced to zero after long times as documented in literature.

The behaviour of the longitudinal and transverse coefficients for systems with density and viscosity contrasts were then investigated. For stable systems, the longitudinal and transverse coefficients respectively decreased and increased with increasing system stability. As explained in the text, these behaviours were also consistent with the physical expectations.

For unfavourable densities, longitudinal and transverse coefficients that respectively increased and reduced with increasing system instability were obtained. The longitudinal coefficients showed asymptotic behaviour for moderate unstable density contrasts but grew indefinitely for larger densities. The asymptotic longitudinal coefficients could therefore be used to predict the range of unstable density contrasts stabilised by medium heterogeneities.

Transverse coefficients were obtained that increased with variance and medium anisotropy while the longitudinal coefficients increased with density contrast and correlation length. D_{11}^{eff} also decreased with anisotropy and all these observations were consistent with physical expectations. For an isotropic medium it was found that the longitudinal coefficient and the time it required to attain equilibrium increased with λ_v .

The numerical simulations returned a reduction in the number of fingers with stabilising variables and vice-versa. A transition from two to three fingers was obtained as the correlation length was increased beyond a certain value. The correlation length

at which the third finger appeared was a few multiples of the critical wavelength obtained previously in the homogeneous medium. The relation between the critical perturbation wavelength and the correlation length was not rigorously pursued. We assumed a simple linear relation that we collaborated with numerical simulations and assumed the numbers that fit. A rigorous analysis would be required to build the relationship.

The stability number at $\rho_{max} = 998.5 \text{ kg} \cdot \text{m}^{-3}$ increased from -1.976 in a homogeneous medium to -1.699 in the heterogeneous medium (at $\sigma^2 = 0.6$). At that density, three fingers previously formed in the homogeneous medium while the third finger first formed at $\rho_{max} = 998.6 \text{ kg} \cdot \text{m}^{-3}$ in the heterogeneous medium, at a stability number of -2.125 .

A comparison of the ranges of the stability numbers at which the transition from 2 to 3 fingers occurs in a homogeneous and heterogeneous medium is shown in Fig. 5.17.

Regime	Diffusive	Stable convective	Unstable convective
No. of Fingers	1	2	3
Homogeneous	$\Lambda_p^* > 0$	$-1.172 < \Lambda_p^* < 0$	$\Lambda_p^* < -1.967$
Heterogeneous	$\Lambda_p^{**} > 0$	$-2.125 < \Lambda_p^{**} < 0$	$\Lambda_p^{**} < -2.372$

Fig. 5.17 The regimes demarcated by the stability number

The region is shifted from the second hatched region on the first row to the dotted hatch in the second row. The reduction in the stability number means increased density at which fingering occurs in heterogeneous media. Heterogeneous mixing reduces the spectrum with long wavelengths that can grow into fingers, thereby stabilising. The stability criterion did not pinpoint the transition point from two to three fingers but from figures 5.11 through 5.15 and the corresponding tables, the range $-2.372 < \Lambda_p^{**} < -2.125$ is satisfied. The following criterion can be formulated from that range of stability numbers:

- I: **1 finger**: nearly diffusive system $\Lambda_p^{**} > 0$,
- II: **2 fingers**: stable convective system $-2.125 < \Lambda_p^{**} < 0$,
- III: **3 fingers**: unstable convective system $\Lambda_p^{**} < -2.372$.

It was also shown in numerical simulations and the criterion that both dispersivities have stabilising properties, with the longitudinal more stabilising than the transverse. The criterion was very sensitive to changes in the transverse dispersivity and in fact switched signs when the simulations still showed more than one finger. This was a failure probably arising from the expression for the dispersion zone width fitted in chapter 4. It might need to be re-investigated.

The assumption of very large Péclet numbers could not be relaxed to study the impact of dispersivities on the macrodispersion coefficients. This was due to the limitations from the available computing resources. Related to that, the effect of medium anisotropy on stability could not be quantified because the variable is not included in the stability number. However anisotropy was qualitatively found to stabilise in numerical simulations.

Longitudinal and transverse coefficients that respectively reduced and increased with anisotropy were obtained indicating stabilising capabilities. This was a collaboration of the simulation results on one hand but also the physical considerations mentioned in the text.

The stabilisation from heterogeneity variance for a range of density contrasts, the estimation of the cutoff correlation length and the shift of the region over which the transition from 2 to 3 fingers occurred provided proof of the hypotheses stated at the beginning the work. However, no instance was obtained where a favourable density contrast in a homogeneous medium resulted into fingering in a heterogeneous medium.

Chapter 6

Discussion and Conclusion

6.1 Discussion

The homogenization theory ideas from Held et al. (2005) were extended to derive expressions for the stability criterion and the macrodispersion tensor for density-driven flow in a saturated heterogeneous medium. Assumptions regarding isothermal conditions, absence of sources and sinks, chemical reactions and sorption were made. Steady states were also assumed in the mathematical analyses. That required to let the numerical simulations run for a long time to achieve stationarity in the finger evolution.

The work also utilised linear dependencies of density on both mass fraction and viscosity. This eased the underlying mathematics on one hand but also ensured continuity with the previous work of Held et al. (2005). Implementation of different state dependencies would result in different stability criteria formulations. However when the ideal relationship that is widely used e.g. in Oldenburg and Pruess (1995), Diersch and Kolditz (2002) and Johannsen (2002) was implemented, no significant differences were observed in the fingers at the low density contrasts used in this work.

The 2-scale expansion used for velocity was adopted from Lunati et al. (2002). Other methods exists where the expansions are done e.g. in terms of small and large Péclet

numbers. The two methods are comparable intermediately but the final results are different. The choice of Lunati et al.'s method was again to seamlessly extend the earlier work of Held et al. (2005).

The Oberbeck-Boussinesq approximation has been widely used in many previous studies. It was documented e.g. in Kolditz et al. (1998) that the effect of using the full equations was not known. It was ascertained here that whereas the numerical simulations with and without the approximation return no significant differences at low density contrasts, the predictions from criteria formulated with and without the approximation were completely different. The criterion derived in this work with the full equations made more timely stability transition predictions. The approximations have a stabilising effect arising from the neglected density terms.

A small domain was used throughout this work to achieve very fine grid and time refinement. The fine refinement was desired to ensure stability of the numerical solution without having to use upwind techniques. Much as the techniques are recommended e.g. by Frolkovič and De Schepper (2001) for convection-dominated problems, the numerical diffusion they introduce would distort the true stability state of the system. Big domains would have presented computational bottlenecks.

The dispersive part was expressed in terms of the perturbation wavelength, the mixing zone width and the two principal-direction dispersivities. An analytical expression for the mixing zone was derived and fitted. A method was also devised to induce perturbations with different wavelengths at the inflow zone, from which the critical wavelength could be obtained. The perturbation of the inflow region however resulted in loss of symmetry of the concentration front, a phenomenon also reported in Marle (1981) where a comparable perturbing function was used.

In the derivation of the expression for the mixing zone, molecular diffusion was neglected. Much as this simplified the analysis, the mechanism is responsible for transport of species across streamlines. It therefore contributes to the spreading mechanism and hence the mixing zone. Its exclusion is therefore erroneous and ought to be revisited.

To enable comparison with earlier researchers, it was necessary to reformulate the stability criterion in form of a Rayleigh number. Contrary to the usual procedure, the characteristic length (taken equal to the mixing zone width) and the effective dispersion were used instead of the domain size and molecular diffusion respectively. Viscosity was also included in addition to the density contrast. This resulted in Rayleigh numbers which were much smaller than what is found in literature but the documented phenomena e.g. the increase of the Rayleigh number with density contrast, the three regimes in Diersch and Kolditz (2002) and the transition in the number of fingers in Johannsen (2002) could be achieved.

The transition in the number of fingers (an indication of system stability) could also be modified by appropriately choosing the density, viscosity and dispersion lengths. We concluded that the unconditional instability widely reported for Elder-type systems is possibly a consequence of the high density contrasts (usually 20% is used) and insufficient stabilisation from diffusion. Those bottlenecks were overcome in this work by the inclusion of dispersion and the low densities.

The stability number could correctly predict the onset of convection (appearance of second finger) by changing sign from positive to negative. The appearance of subsequent fingers e.g. the third occurred at higher densities (smaller stability numbers) but no definite stability number was obtained at which the transition from two to three fingers occurred. A range was obtained for the transition.

Lognormally distributed permeability fields with Gaussian auto-correlation functions were used in this work. The choice of the lognormal distribution was primarily justified by the desire to avoid unphysical negative hydraulic conductivities. Gaussian auto-correlated fields are also suitable for conductivity fields without abrupt changes like fractures.

The extension of the stability studies to heterogeneous media was achieved by conceptualising large-scale mixing as a coupling of small-scale dispersion and macrodispersion acting at larger scales. One then has a large-scale mixing zone controlled by the effective dispersivities defined in terms of the local homogeneous-medium dispersivities and changes induced by medium heterogeneity. The heterogeneity-induced

dispersivities are functions of the heterogeneity variance and correlation length.

The mean displacement could still be taken from the expression derived for the homogeneous medium, with the effective instead of the local dispersivity. The heterogeneous medium stability number was not explicitly expressed in terms of a Rayleigh number because according to Nield (1994), the definition of such numbers for heterogeneous media is problematic.

By designating a simulation at certain parameters as reference, the individual medium heterogeneity effects: the variance, medium anisotropy and the correlation length could be studied. The expected stabilisation by medium heterogeneity was captured in the change to two fingers at a density contrast that returned three fingers in a homogeneous medium. Physically the stabilisation is due to mixing, which reduces the quantity of perturbations with long enough wavelengths (energy) to persist into fingers.

The destabilising effect of the correlation length was also shown in the transition from two to three fingers. That provided the answer to the question of when medium heterogeneities could destabilise. It was concluded that the range of correlation length up to a critical, which is a few multiples of the critical wavelength are stable. Simulations at bigger correlation lengths caused channeling effects that led to loss of symmetry of the concentration front (see e.g. Fig. 5.9c on page 95).

With medium heterogeneities included, we obtained an increase in the density contrast at which the third finger formed. The appearance of the third finger at higher densities (smaller stability numbers) is an indication of stabilisation by medium heterogeneity. It provided another answer to one of the key objectives of this work.

For the homogeneous medium, the critical wavelength was approximated from a sinus function used to perturb the in-flowing salt. The perturbed boundary condition was not necessary in heterogeneous media because the heterogeneities provide the local perturbations in the salt. The use of a constant boundary condition however led the quantity of salt to exceed that in the homogeneous case. The discrepancies in the salt quantity and the method of initiating instabilities meant that the results

might not have been exactly comparable.

Anisotropy was not included in the stability number, therefore its effects on stability could not be quantified. It was however shown to stabilise in the macrodispersion coefficients and numerical simulations. The stabilisation could also be accounted for physically.

The large-scale equation from homogenization theory was used to formulate the macrodispersion tensor. The tensor was symmetric with zero off-diagonal elements. The diagonal elements exhibited scale-dependency: for passive tracers, the longitudinal coefficient approached an asymptote and decreased with medium anisotropy while the transverse coefficient diminished after long times and responded marginally to changes in medium anisotropy. This behaviour was in agreement with the results in literature e.g. Dagan (1988).

For favourable density contrasts the longitudinal coefficient approached an asymptote but in general decreased with system stabilisation. The transverse coefficient on the other hand increased with system stabilisation. The respective increase and reduction in the longitudinal and transverse coefficients could be obtained from variables that destabilise: correlation length and density. Reverse behaviour was obtained from the heterogeneity variance and anisotropy which stabilise.

For unfavourable densities, the longitudinal coefficient increased with system destabilisation while the transverse coefficient reduced. That behaviour was consistent with physical considerations. The longitudinal coefficient remained asymptotic for a range of unfavourable density contrasts but eventually grew indefinitely with time. Therefore by carefully controlling the density contrast, the range of unfavourable density contrasts that exhibited asymptotic behaviour could be obtained. Welty and Gelhar (1991) reported infinitely large longitudinal coefficients for the whole range of unfavourable density contrasts.

By giving a window of unfavourable densities for which the coefficient remained asymptotic, this work provided a method of estimating the range of density contrasts that could be stabilised by heterogeneities.

The stabilising effects of the dispersivities could not be included in the computation of the macrodispersion coefficients. This was a result of constraints from computing infrastructure to allow the relaxation of the infinite Péclet number assumption.

Related to the computing restrictions was the evaluation of the macrodispersion coefficients for the problem in chapter 3 defined by Schincariol.

6.2 Conclusion

The homogenization ideas developed in Held et al. (2005) were successfully extended to derive a stability criterion for vertical flow in a heterogeneous medium. The extension was done in steps: a homogeneous medium without dispersion, which was extended to include dispersion and finally the inclusion of medium heterogeneity. For the first case, the stability number was positive for stable systems while positive numbers indicated the absence of convection in the latter two cases.

The stability criterion for heterogeneous media is the first known attempt to formulate both fluid and porous medium properties and use them to predict the onset of fingering. Even with the limitations of the underlying assumptions, the criterion produced reasonable predictions that were collaborated with physical processes and numerical simulations. Using the derived criterion, it is possible to estimate the onset of the unstable-convective regime in density-driven systems.

Answers have been provided to the various questions and hypotheses set out at the beginning. The effects of density, viscosity, flow velocity, dispersivities and medium heterogeneity on flow stability have been quantified. The medium heterogeneity was found to stabilise by increasing the density contrast at which fingering occurred. The variance always stabilised while the system remained stable as long as the correlation length was below a certain cutoff. In no instance did heterogeneities induce fingering at a density contrast that was stable in the homogeneous medium.

The analytical expression to estimate the dispersion mixing zone in terms of physical variables is another salient feature of the work. We addressed the ambiguity

previously related to making the choice (Buès and Aachib 1991, Schincariol et al. 1997).

Time-dependent macrodispersion coefficients for unfavourable density contrasts are not widely documented. Using the coefficients, we provided a method of estimating the range of unstable density contrasts stabilised by medium heterogeneities. The computation of the coefficients required a copyrighted software and were very demanding computationally. The computational bottlenecks restricted the evaluation of the coefficients to the simple vertical flow systems but not the more practical groundwater-type horizontal systems.

It is hoped that the study shed more light on the factors that impact the stability of density-driven flows. We also hope that seamless extensions can be made to bigger real-life domain extents.

6.3 Outlook

This work had a number of underlying assumptions, some of which need to be relaxed to better approximate real-life systems. We mention here the infinite Péclet number, linear state dependencies, linear perturbation theory (inclusion of higher expansion terms), lack of dependency of the mixing zone on diffusion and consideration of more practical horizontal flow systems.

Computing power allowing, it would be worthwhile to use a bigger, more realistic domain. This would also allow the choice of bigger correlation lengths and dispersion lengths.

Temperature effects were not included but are part of our ongoing investigations.

Appendix A

Mathematical Derivations

In this chapter detailed derivations for the contributions of the small-scale mass fraction and medium permeability heterogeneity to the mesoscale velocity fluctuations as well as the elements of the macrodispersion tensor are presented.

A.1 Derivation of $M(\mathbf{q})$

As already mentioned in Section 3.1, we assume a divergence-free flow that results into $\nabla \cdot \mathbf{v} = 0$. Any divergence-free vector field $\mathbf{v}(\mathbf{X})$ can be written as the rotation of a vector field $\mathbf{A}(\mathbf{X})$ i.e. $\mathbf{v}(\mathbf{X}) = \nabla \times \mathbf{A}(\mathbf{X})$. To completely define \mathbf{A} , $\nabla \cdot \mathbf{A} = 0$ is taken Held et al. (2005). Divergence free velocity is used for consistence with the form used in homogenizing the transport equation.

This work concerns 2-dimensional flow. In the following we see the vectors in \mathbb{R}^2 as three dimensional vectors with a zero third component. The second component remains the one corresponding to the gravitational direction. This allows us to use the cross product $\nabla \times \mathbf{v}$ in (A.1.2) and makes a further extensions to 3-dimensions problems straightforward.

To introduce the effects of density and viscosity on velocity, Held et al. (2005) used

the modified groundwater velocity introduced in section 3.1:

$$\mathbf{v} = -\frac{\rho(\omega)\mathbf{k}}{\mu(\omega)}\nabla p + \frac{\mathbf{k}\rho(\omega)^2}{\mu(\omega)}\mathbf{g}. \quad (\text{A.1.1})$$

Following Held et al. (2005) we split the vector

$$\nabla \times \mathbf{v} = \begin{pmatrix} 0 \\ 0 \\ \partial_1 v_2 - \partial_2 v_1 \end{pmatrix} \quad (\text{A.1.2})$$

into parts depending on the total velocity \mathbf{v} and the gravitational velocity \mathbf{v}^g defined as $\mathbf{v}^g = \frac{\rho(\omega)^2}{\mu(\omega)}\mathbf{k}\mathbf{g}$. We apply the product rule of differentiation on (A.1.1) and the linear dependencies of density and viscosity on salt mass fraction (equations (2.15) and (2.16)) to evaluate the right hand side of (A.1.2). This requires the Taylor expansions for $\partial_1 \left(\frac{\rho(\omega)}{\mu(\omega)} \right)$, $\partial_2 \left(\frac{\rho(\omega)}{\mu(\omega)} \right)$, $\partial_1 \left(\frac{\rho(\omega)^2}{\mu(\omega)} \right)$ and $\partial_2 \left(\frac{\rho(\omega)^2}{\mu(\omega)} \right)$, which with further simplification yields

$$\nabla \times \mathbf{v} = (\alpha - \beta) \left(\frac{\rho_0 \mu(\omega)}{\mu_0 \rho(\omega)} \right) \nabla \omega \times \mathbf{v} + \left[(2\alpha - \beta) \frac{\rho_0^2 \mu(\omega)}{\mu_0 \rho(\omega)^2} - (\alpha - \beta) \frac{\rho_0 \mu(\omega)}{\mu_0 \rho(\omega)} \right] \nabla \omega \times \mathbf{v}^g. \quad (\text{A.1.3})$$

The left hand side of equation (A.1.3) can be written as $\nabla \times \nabla \times \mathbf{A}$ and the potential \mathbf{A} as a series expansion in ϵ : $\mathbf{A} = \mathbf{A}_0 + \epsilon \tilde{\mathbf{A}}$, where a linear perturbation analysis has been performed with \mathbf{A}_0 , $\tilde{\mathbf{A}}$ being the large scale and fluctuating potentials respectively. We then have $\nabla \times \nabla \times (\mathbf{A}_0 + \epsilon \tilde{\mathbf{A}})$, which we expand in 2 scales using $\nabla = (\nabla_{\mathbf{x}} + \frac{1}{\epsilon} \nabla_{\mathbf{y}})/L$. The 2-scale expansion of \mathbf{A} is justified by its dependence on the 2-scale velocity. The expansion in (2.19) is applied on the ω in the right hand side of (A.1.3), products of perturbations neglected and the vector products evaluated using the approach developed by Lunati et al. (2002) to give the respective expressions defining the large-scale potential as:

$$\nabla_{\mathbf{x}}^2 \mathbf{A}_0 = L(\alpha - \beta) \nabla_{\mathbf{x}} \omega_0 \times \nabla_{\mathbf{x}} \times \mathbf{A}_0 + L\alpha \nabla_{\mathbf{x}} \omega_0 \times \mathbf{v}_0^g \quad (\text{A.1.4})$$

where \mathbf{v}_0^g is the mean macroscale gravity-driven velocity. The fluctuating potential

is similarly given as:

$$\begin{aligned}\nabla_{\mathbf{y}}^2 \tilde{\mathbf{A}} &= L(\alpha - \beta) \nabla_{\mathbf{x}} \omega_0 \times \tilde{\mathbf{v}} + L(\alpha - \beta) \nabla_{\mathbf{y}} \omega_1 \times \mathbf{v}_0 + L\alpha \nabla_{\mathbf{y}} \omega_1 \times \mathbf{v}_0^g \\ &\quad + L\alpha \nabla_{\mathbf{x}} \omega_0 \times \tilde{\mathbf{v}}^g ,\end{aligned}\tag{A.1.5}$$

where \mathbf{v}_0 is the macroscale mean drift and $\tilde{\mathbf{v}}$, $\tilde{\mathbf{v}}^g$ the respective fluctuations in the velocities. In (A.1.5), for consistency with the homogenization theory in Held et al. (2005), we have neglected terms of orders greater than $O(\epsilon^0)$. If for similar reasons we further neglect terms with $O(\omega_1)$ and higher arising from $\tilde{\mathbf{v}}$ and $\tilde{\mathbf{v}}^g$ we obtain:

$$\begin{aligned}\nabla_{\mathbf{y}}^2 \tilde{\mathbf{A}} &= -\partial_y^2 \tilde{\mathbf{A}} \\ &= L(\alpha - \beta) \nabla_{\mathbf{y}} \omega_1 \times \mathbf{v}_0 + L\alpha \nabla_{\mathbf{y}} \omega_1 \times \mathbf{v}_0^g .\end{aligned}\tag{A.1.6}$$

The solution for $\tilde{\mathbf{A}}$ follows by transforming (A.1.6) into Fourier space, in which case we obtain

$$\tilde{\mathbf{A}}(\mathbf{q}) = L \frac{(\alpha - \beta) i\mathbf{q} \times \mathbf{v}_0 + \alpha i\mathbf{q} \times \mathbf{v}_0^g}{\|\mathbf{q}\|^2} \omega_1(\mathbf{q}) .\tag{A.1.7}$$

Finally, the fluctuating velocity is obtained from the rotation of $\tilde{\mathbf{A}}(\mathbf{q})$:

$$\begin{aligned}\tilde{\mathbf{v}}(\mathbf{q}) &= \frac{1}{L} i\mathbf{q} \times \tilde{\mathbf{A}}(\mathbf{q}) \\ &= \frac{(\alpha - \beta) i\mathbf{q} \times i\mathbf{q} \times \mathbf{v}_0 + \alpha i\mathbf{q} \times i\mathbf{q} \times \mathbf{v}_0^g}{\|\mathbf{q}\|^2} \omega_1(\mathbf{q}) \\ &\equiv \mathbf{M}(\mathbf{q}) \omega_1(\mathbf{q}) .\end{aligned}\tag{A.1.8}$$

From equation (A.1.8), the velocity fluctuations caused by changes in mass fraction are given by (A.1.9):

$$\mathbf{M}(\mathbf{q}) = \frac{(\alpha - \beta) i\mathbf{q} \times i\mathbf{q} \times \mathbf{v}_0 + \alpha i\mathbf{q} \times i\mathbf{q} \times \mathbf{v}_0^g}{\|\mathbf{q}\|^2} .\tag{A.1.9}$$

To enhance the applicability of our findings, we give now explicitly the formula of $\mathbf{M}(\mathbf{q})$ for the two dimensional cases. Suppose the vectors have the components:

$\mathbf{v}_0 = \begin{pmatrix} v_1 \\ v_2 \end{pmatrix}$, $\mathbf{v}_0^g = \begin{pmatrix} v_1^g \\ v_2^g \end{pmatrix}$ and $\mathbf{q} = \begin{pmatrix} q_1 \\ q_2 \end{pmatrix}$. Then $\mathbf{M}(\mathbf{q})$ evaluates to:

$$\mathbf{M}(\mathbf{q}) = \frac{1}{(q_1^2 + q_2^2)} \begin{pmatrix} (\alpha - \beta)(q_2^2 v_1 - q_1 q_2 v_2) + \alpha(q_2^2 v_1^g - q_1 q_2 v_2^g) \\ (\alpha - \beta)(q_1^2 v_2 - q_1 q_2 v_1) + \alpha(q_1^2 v_2^g - q_1 q_2 v_1^g) \end{pmatrix}. \quad (\text{A.1.10})$$

A.2 Derivation of $\mathbf{L}(\mathbf{q})$

In the following we present the derivation of the contribution from the heterogeneous permeability field to mesoscale velocity fluctuations. The derivation follows similar steps to those used for $\mathbf{M}(\mathbf{q})$ in section A.1. We start from the modified groundwater velocity

$$\mathbf{v} = -\frac{\mathbf{k}\rho(\omega)}{\mu(\omega)}\nabla p + \frac{\mathbf{k}\rho(\omega)^2}{\mu(\omega)}\mathbf{g},$$

where $\mathbf{k} = k\mathbf{I}_2$. The rotation of the velocity then becomes

$$\begin{aligned} \nabla \times \mathbf{v} &= \overbrace{\partial_1 \frac{\rho(\omega)}{\mu(\omega)} [-\mathbf{k}\nabla p]_2 - \partial_2 \frac{\rho(\omega)}{\mu(\omega)} [-\mathbf{k}\nabla p]_1 + \partial_1 \frac{\rho(\omega)^2}{\mu(\omega)} [\mathbf{k}\mathbf{g}]_2 - \partial_2 \frac{\rho(\omega)^2}{\mu(\omega)} [\mathbf{k}\mathbf{g}]_1}^{\text{evaluated previously for } \mathbf{M}(\mathbf{q})} \\ &\quad + \partial_1 \mathbf{k} \left[-\frac{\rho(\omega)}{\mu(\omega)} (\nabla p - \rho(\omega)\mathbf{g}) \right]_2 - \partial_2 \mathbf{k} \left[-\frac{\rho(\omega)}{\mu(\omega)} (\nabla p - \rho(\omega)\mathbf{g}) \right]_1. \end{aligned} \quad (\text{A.2.1})$$

From here onwards, only the second row of (A.2.1) is considered. From (A.2.1), denoting the velocity contributed by the permeability field as \mathbf{v}_k one can write

$$\nabla \times \mathbf{v}_k = \frac{\nabla k \times \mathbf{v}}{k}. \quad (\text{A.2.2})$$

Next the permeability and velocity are split into the mean and fluctuating parts: $k = \bar{k} + \tilde{k}$, $\mathbf{v} = \mathbf{v}_0 + \tilde{\mathbf{v}}$; the 2-scale spatial derivatives are also used $\nabla = \nabla_{\mathbf{x}} + \frac{1}{\epsilon}\nabla_{\mathbf{y}}$ (see section 2.3.1 on page 28) to obtain

$$\begin{aligned} \nabla \times \mathbf{v}_k &= \frac{1}{\bar{k}} \left(1 - \frac{\tilde{k}}{\bar{k}} \right) \left(\nabla_{\mathbf{x}} \bar{k} \times \mathbf{v}_0 + \nabla_{\mathbf{x}} \bar{k} \times \tilde{\mathbf{v}} + \nabla_{\mathbf{x}} \tilde{k} \times \mathbf{v}_0 + \nabla_{\mathbf{x}} \tilde{k} \times \tilde{\mathbf{v}} \right) \\ &\quad + \frac{1}{\epsilon \bar{k}} \left(1 - \frac{\tilde{k}}{\bar{k}} \right) \left(\nabla_{\mathbf{y}} \tilde{k} \times (\mathbf{v}_0 + \tilde{\mathbf{v}}) \right), \end{aligned} \quad (\text{A.2.3})$$

in which $\frac{1}{(\bar{k} + \tilde{k})}$ has been approximated by a Taylor expansion up to the linear term. Following Held et al. (2005), the velocity is written as a rotation of a vector \mathbf{A} , which when expanded in 2 scales gives the left hand side of (A.2.3) as $\nabla \times \nabla \times (\mathbf{A}_{0k} + \epsilon \tilde{\mathbf{A}}_k)$ with the k subscript denoting the permeability field. Expanding the ∇ into large and small scales allows the contribution to be grouped into those respective scales. For the small-scale contribution, the products of fluctuations are neglected in conformity with the linear perturbation theory and only terms of order $O(\epsilon^0)$ considered (Held et al. 2005).

The surviving terms from (A.2.3) yield $\nabla_{\mathbf{y}} \times \nabla_{\mathbf{y}} \times \tilde{\mathbf{A}}_k = -\partial_y^2 \tilde{\mathbf{A}}_k = \frac{\nabla_{\mathbf{y}} \tilde{k} \times \mathbf{v}_0}{\bar{k}}$. In Fourier space one gets

$$\tilde{\mathbf{A}}_k(\mathbf{q}) = \frac{i\mathbf{q} \times \mathbf{v}_0}{\bar{k}\|\mathbf{q}\|^2} \tilde{k}(\mathbf{q}) . \quad (\text{A.2.4})$$

The velocity fluctuations contributed by the permeability heterogeneity are obtained by taking the rotation of (A.2.4):

$$\tilde{\mathbf{v}}_k(\mathbf{q}) = \frac{i\mathbf{q} \times i\mathbf{q} \times \mathbf{v}_0}{\bar{k}\|\mathbf{q}\|^2} \tilde{k}(\mathbf{q}) . \quad (\text{A.2.5})$$

The velocity fluctuations are given by

$$\tilde{\mathbf{v}}(\mathbf{q}, \tau) = \mathbf{M}(\mathbf{q})\omega_1(\mathbf{q}, \tau) + \mathbf{L}(\mathbf{q})\tilde{k}(\mathbf{q}) .$$

If the contribution from the permeability heterogeneity is compared with (A.2.5), one obtains

$$\mathbf{L}(\mathbf{q}) = \frac{i\mathbf{q} \times i\mathbf{q} \times \mathbf{v}_0}{\bar{k}\|\mathbf{q}\|^2} . \quad (\text{A.2.6})$$

Assuming the 2-dimensional vectors to have components

$$\mathbf{v}_0 = \begin{pmatrix} v_1 \\ v_2 \end{pmatrix} \text{ and } \mathbf{q} = \begin{pmatrix} q_1 \\ q_2 \end{pmatrix}, \text{ one further obtains}$$

$$\mathbf{L}(\mathbf{q}) = \begin{pmatrix} L_1(\mathbf{q}) \\ L_2(\mathbf{q}) \end{pmatrix} = \frac{1}{\bar{k}} \left(\frac{1}{q_1^2 + q_2^2} \right) \begin{pmatrix} q_2^2 v_1 - q_1 q_2 v_2 \\ q_1^2 v_2 - q_1 q_2 v_1 \end{pmatrix} . \quad (\text{A.2.7})$$

A.3 Derivation of the Macrodispersion Tensor Elements

The derivations of the individual elements in the macrodispersion tensor are presented here. The diagonal elements are derived first and the off-diagonal elements are presented at the end of the section. The general expression for the macrodispersion tensor was given as

$$\mathbf{D}^{\text{eff}} = \mathbf{D}^* - \overline{\tilde{\mathbf{v}} \otimes \boldsymbol{\chi}^\omega} ,$$

and the individual elements evaluated to

$$\mathbf{D}^{\text{eff}} = \begin{pmatrix} \rho(\omega) - \frac{L}{D_{\parallel}} \overline{\tilde{v}_1 \chi_1^\omega} & -\frac{L}{D_{\parallel}} \overline{\tilde{v}_1 \chi_2^\omega} \\ -\frac{L}{D_{\parallel}} \overline{\tilde{v}_2 \chi_1^\omega} & \rho(\omega) \frac{D_{\perp}}{D_{\parallel}} - \frac{L}{D_{\parallel}} \overline{\tilde{v}_2 \chi_2^\omega} \end{pmatrix} .$$

We proceed by using the velocity fluctuations

$$\tilde{\mathbf{v}}(\mathbf{q}, \tau) = \mathbf{M}(\mathbf{q})\omega_1(\mathbf{q}, \tau) + \mathbf{L}(\mathbf{q})\tilde{k}(\mathbf{q})$$

and the solution to the cell problem

$$\chi_n^\omega(\mathbf{q}, \tau) = -\kappa \int_0^\tau d\tau' L_n(\mathbf{q})\tilde{k}(\mathbf{q}) \exp \left(- \left(i \frac{L}{\rho(\omega)D_{\parallel}} \mathbf{v} \cdot \mathbf{q} + \frac{\mathbf{D}^* \mathbf{q} \cdot \mathbf{q}}{\rho(\omega)} + \frac{\Lambda}{\rho(\omega)} \right) \tau' \right)$$

in the expression above for the elements of the macrodispersion tensor.

The individual elements can generally be written as

$$\begin{aligned} D_{nj}^{\text{eff}} &= D_{nj} + \kappa \int_0^\tau d\tau' \int d^d q L_n(\mathbf{q}) L_j(\mathbf{q}) \tilde{k}(\mathbf{q}) \tilde{k}(\mathbf{q}') \\ &\quad \times \exp \left(- \left(i \kappa \mathbf{v} \cdot \mathbf{q} + \frac{\mathbf{D}^* \mathbf{q} \cdot \mathbf{q}}{\rho(\omega)} + \frac{\Lambda_p}{\rho(\omega)} \right) \tau' \right) \\ &\quad + \kappa \int_0^\tau d\tau' \int d^d q L_n(\mathbf{q}) M_j(\mathbf{q}) \omega_1(\mathbf{q}, \tau) \tilde{k}(\mathbf{q}) \\ &\quad \times \exp \left(- \left(i \kappa \mathbf{v} \cdot \mathbf{q} + \frac{\mathbf{D}^* \mathbf{q} \cdot \mathbf{q}}{\rho(\omega)} + \frac{\Lambda_p}{\rho(\omega)} \right) \tau' \right) . \end{aligned} \quad (\text{A.3.1})$$

For the vertical flow systems under consideration we assume the $\mathbf{1}$ principal direction to be in the direction of gravity such that $v_1 = v_0$ and the transverse component $v_2 = 0$. The contribution of the medium heterogeneity to velocity fluctuations evaluates to

$$\mathbf{L}(\mathbf{q}) = \frac{1}{\bar{k}} \left(\frac{1}{q_1^2 + q_2^2} \right) \begin{pmatrix} q_2^2 v_0 \\ -q_1 q_2 v_0 \end{pmatrix} .$$

Appropriate components have to be used for the various elements according to the values taken by the indices in (A.3.1). Additionally, the relations

$$\omega_1(\mathbf{q}, \tau) = \boldsymbol{\chi}^\omega(\mathbf{q}, \tau) \cdot \mathbf{G} ,$$

for the mesoscopic mass fraction and

$$\tilde{k}(\mathbf{q})\tilde{k}(\mathbf{q}') = w_f(\mathbf{q})$$

for the auto-correlation function, have to be substituted. After re-applying the equation for the solution to the cell problem, using the equation for the auto-correlation function again and the relation

$$M_1(\mathbf{q})G_1 = \Lambda_p$$

for the stability number, (A.3.1) simplifies to

$$\begin{aligned} D_{nj}^{\text{eff}} &= D_{nj} + \kappa \int_0^\tau d\tau' \int d^d q L_n(\mathbf{q}) L_j(\mathbf{q}) w_f(\mathbf{q}) \\ &\quad \times \exp \left(- \left(i\kappa \mathbf{v} \cdot \mathbf{q} + \frac{\mathbf{D}^* \mathbf{q} \cdot \mathbf{q}}{\rho(\omega)} + \frac{\Lambda_p}{\rho(\omega)} \right) \tau' \right) \\ &\quad - \Lambda_p \kappa \int_0^\tau d\tau'' \int_0^\tau d\tau' \int d^d q L_n(\mathbf{q}) L_j(\mathbf{q}) w_f(\mathbf{q}) \\ &\quad \times \exp \left(- \left(i\kappa \mathbf{v} \cdot \mathbf{q} + \frac{\mathbf{D}^* \mathbf{q} \cdot \mathbf{q}}{\rho(\omega)} + \frac{\Lambda_p}{\rho(\omega)} \right) \tau' \right) \\ &\quad \times \exp \left(- \left(i\kappa \mathbf{v} \cdot \mathbf{q} + \frac{\mathbf{D}^* \mathbf{q} \cdot \mathbf{q}}{\rho(\omega)} + \frac{\Lambda_p}{\rho(\omega)} \right) \tau'' \right) . \end{aligned} \quad (\text{A.3.2})$$

A.3.1 The Longitudinal Coefficient D_{11}^{eff} .

The indices in (A.3.2) are set to $n = j = 1$ and the expression for $L_1(\mathbf{q})$ from (5.15) used to obtain

$$\begin{aligned}
D_{11}^{\text{eff}} = & D_{11} + \kappa \int_0^\tau d\tau' \int_{-\infty}^\infty \int_{-\infty}^\infty \left(\frac{v_0 q_2^2}{\bar{k}(q_1^2 + q_2^2)} \right)^2 w_f(\mathbf{q}) \\
& \times \exp \left(- \left(i\kappa \mathbf{v} \cdot \mathbf{q} + \frac{\mathbf{D}^* \mathbf{q} \cdot \mathbf{q}}{\rho(\omega)} + \frac{\Lambda_p}{\rho(\omega)} \right) \tau' \right) dq_1 dq_2 \\
& - \Lambda_p \kappa \int_0^\tau d\tau'' \int_0^\tau d\tau' \int_{-\infty}^\infty \int_{-\infty}^\infty \left(\frac{v_0 q_2^2}{\bar{k}(q_1^2 + q_2^2)} \right)^2 w_f(\mathbf{q}) \\
& \times \exp \left(- \left(i\kappa \mathbf{v} \cdot \mathbf{q} + \frac{\mathbf{D}^* \mathbf{q} \cdot \mathbf{q}}{\rho(\omega)} + \frac{\Lambda_p}{\rho(\omega)} \right) \tau' \right) \\
& \times \exp \left(- \left(i\kappa \mathbf{v} \cdot \mathbf{q} + \frac{\mathbf{D}^* \mathbf{q} \cdot \mathbf{q}}{\rho(\omega)} + \frac{\Lambda_p}{\rho(\omega)} \right) \tau'' \right) dq_1 dq_2 . \quad (\text{A.3.3})
\end{aligned}$$

The coefficient is written as a sum of integrals: $D_{11}^{\text{eff}} = D_{11} + I_1 + I_2$ and a detailed derivation of the part I_1 is shown in the following. It is worthwhile to note the similarity of the integrands in I_1 and I_2 and all the other integrals making up the various coefficients. The only differences arise from the product $L_n(\mathbf{q})L_j(\mathbf{q})$, depending on the values taken by the indices n and j . Since the technique is applicable to all the other integrals, the details are given for I_1 only.

The following are the steps in the evaluation of I_1 : the integrands containing \mathbf{q}^{-4} , $\exp(-\mathbf{D}^* \mathbf{q} \cdot \mathbf{q} \tau')$ and $w_f(\mathbf{q})$ are expressed in form of Gaussian integrals as follows:

$$\begin{aligned}
\left(\frac{1}{q_1^2 + q_2^2} \right)^2 &= \int_0^\infty \exp(-r(q_1^2 + q_2^2)) dr \int_0^\infty \exp(-s(q_1^2 + q_2^2)) ds , \\
\exp \left(- \frac{\mathbf{D}^* \mathbf{q} \cdot \mathbf{q} \tau'}{\rho(\omega)} \right) &= \exp \left(- \frac{q_1^2 D_{11}^* \tau'}{\rho(\omega)} \right) \exp \left(- \frac{q_2^2 D_{22}^* \tau'}{\rho(\omega)} \right) , \\
w_f(\mathbf{q}) &= 4\pi \sigma_f^2 \varepsilon_v \varepsilon_h \exp(-\varepsilon_v^2 q_1^2) \exp(-\varepsilon_h^2 q_2^2) .
\end{aligned}$$

In the expression for the auto-covariance function the subscripts v, h represent the vertical and horizontal directions and the integral scale $\varepsilon_n = \lambda_n / \sqrt{2}$ where λ_n is the correlation length in direction n (Dentz 2000), $n = v, h$.

The various variables are next written in the hatted dimensionless forms:

$\hat{q}_1 = q_1 \varepsilon_v$; $\hat{q}_2 = q_2 \varepsilon_h$; $\varepsilon_v \xi = \varepsilon_h$; $\hat{\tau}' = v_0 \tau' / \varepsilon_v$; $\varepsilon_v dq_1 = d\hat{q}_1$; $\varepsilon_v dq_2 = d\hat{q}_2$; $v_0 d\tau' = \varepsilon_v d\hat{\tau}'$ where ξ is the anisotropy ratio also called the *anis* in Simmons et al. (2001) and defined here as $\varepsilon_h / \varepsilon_v$. Substituting the Gaussian forms and the dimensionless quantities into the expression for I_1 yields

$$\begin{aligned} I_1 = & \Theta \int_0^\infty dr \int_0^\infty ds \int_0^\tau e^{-\Lambda_p \hat{\tau}'} d\hat{\tau}' \\ & \times \int_{-\infty}^\infty \exp\left(-i\kappa \hat{q}_1 \hat{\tau}' - \hat{q}_1^2 \left(1 + \frac{\hat{\tau}'}{\rho(\omega) Pe} + r + s\right)\right) d\hat{q}_1 \\ & \times \int_{-\infty}^\infty \hat{q}_2^4 \exp\left(-\hat{q}_2^2 \left(\xi^2 + \frac{\hat{\tau}'}{\rho(\omega) Pe} + r + s\right)\right) d\hat{q}_2 . \end{aligned}$$

The pre-factor $\Theta = \frac{4\pi\kappa\varepsilon_v\xi v_0\sigma_f^2}{\bar{k}^2}$ has been introduced to shorten the notation. Considering very large Péclet numbers, $\frac{\hat{\tau}'}{\rho(\omega) Pe} \approx 0$ and the diffusion D_{11} can also be neglected (see also Dagan (1988), Fetter (1999), Dentz et al. (2003)). The substitution $\eta = r + s$ further reduces I_1 to

$$\begin{aligned} I_1 = & \Theta \int_s^\infty d\eta \int_0^\infty ds \int_0^\tau e^{-\Lambda_p \hat{\tau}'} d\hat{\tau}' \int_{-\infty}^\infty \exp\left(-i\kappa \hat{q}_1 \hat{\tau}' - \hat{q}_1^2 (1 + \eta)\right) d\hat{q}_1 \\ & \times \int_{-\infty}^\infty \hat{q}_2^4 \exp\left(-\hat{q}_2^2 (\xi^2 + \eta)\right) d\hat{q}_2 . \end{aligned}$$

The integrations with respect to space and time were performed analytically with the software **MAPLE**[®] to yield:

$$\begin{aligned} I_1 = & \Theta \int_s^\infty \int_0^\infty \frac{3}{4} \frac{\pi^{\frac{3}{2}} \exp\left(\frac{\Lambda_p^2 (1+\eta)}{\kappa^2}\right)}{\kappa (\xi^2 + \eta)^{5/2}} \\ & \times \left[\operatorname{erf}\left(\frac{\kappa^2 \tau + 2\Lambda_p + 2\Lambda_p \eta}{2\sqrt{1+\eta}}\right) - \operatorname{erf}\left(\frac{\Lambda_p \sqrt{1+\eta}}{\kappa}\right) \right] ds d\eta . \end{aligned}$$

The remaining two integrals have to be evaluated numerically. As mentioned earlier, the technique outlined above is applicable to the space and time integrals in I_2 and

all the other elements of the tensor. Following similar steps, I_2 can be written as

$$I_2 = \Theta \int_s^\infty d\eta \int_0^\infty ds \int_0^\tau e^{-\Lambda_p \hat{\tau}} d\hat{\tau}'' \int_0^\tau e^{-\Lambda_p \hat{\tau}'} d\hat{\tau}' \int_{-\infty}^\infty \exp\left(-i\kappa \hat{q}_1(\hat{\tau}' + \hat{\tau}'') - \hat{q}_1^2(1 + \eta)\right) d\hat{q}_1 \\ \times \int_{-\infty}^\infty \hat{q}_2^4 \exp(-\hat{q}_2^2(\xi^2 + \eta)) d\hat{q}_2 .$$

The space and time integrals can again be evaluated analytically with **MAPLE**[®]. The complete expression for the longitudinal dispersion coefficient then reads:

$$D_{11}^{\text{eff}} = \Theta \int_s^\infty d\eta \int_0^\infty ds \frac{3\pi}{4\kappa^3(\xi^2 + \eta)^{5/2}} \\ \times \left[A \left(2\Lambda_p^2(1 + \eta)(2\text{erf}(C) - \text{erf}(B) - \text{erf}(D)) \right. \right. \\ \left. \left. + \kappa^2 \left(2\Lambda_p \tau (\text{erf}(C) - \text{erf}(D)) + \text{erf}(C) - \text{erf}(B) \right) \right) \right. \\ \left. - 2\Lambda_p \kappa \sqrt{(1 + \eta)}(1 - 2F + G) \right] . \quad (\text{A.3.4})$$

Where

$$A = \sqrt{\pi} \exp\left(\frac{\Lambda_p^2(1 + \eta)}{\kappa^2}\right), \quad B = \frac{\Lambda_p \sqrt{1 + \eta}}{\kappa}, \quad \Theta = \frac{4\pi\kappa\varepsilon_1 \xi v_0 \sigma_f^2}{\bar{k}^2}, \\ C = \left(\frac{(\tau\kappa^2 + 2\Lambda_p + 2\Lambda_p\eta)}{2\kappa\sqrt{(1 + \eta)}}\right), \quad D = \frac{\Lambda_p\eta + \tau\kappa^2 + \Lambda_p}{\kappa\sqrt{1 + \eta}}, \quad \kappa = \frac{LG_n}{D_{\parallel}\rho(\omega)}, \\ F = \exp\left(-\frac{\tau(\tau\kappa^2 + 4\Lambda_p + 4\Lambda_p\eta)}{4(1 + \eta)}\right) \text{ and } G = \exp\left(-\frac{\tau(\tau\kappa^2 + 2\Lambda_p + 2\Lambda_p\eta)}{1 + \eta}\right).$$

D_{11} has been neglected because of the large Péclet number assumption. The term $\frac{q_2^4}{\|\mathbf{q}\|^4}$ in (A.3.3) can be written as $1 - \frac{2q_1^2}{\|\mathbf{q}\|^2} + \frac{q_1^4}{\|\mathbf{q}\|^4}$ yielding an expression similar to equation (22) in Dagan (1988) derived via stochastic theory and the method of moments for the longitudinal dispersion coefficient of passive tracers ($\Lambda_p = 0$) and large Péclet numbers.

A.3.2 The Transverse Coefficient D_{22}^{eff} .

To evaluate the transverse coefficient, we started from (A.3.2) set $n = j = 2$ and used the expression for $L_2(\mathbf{q})$ from (5.15) to obtain

$$\begin{aligned}
D_{22}^{\text{eff}} = & D_{22} + \kappa \int_0^\tau d\tau' \int_{-\infty}^\infty \int_{-\infty}^\infty \left(\frac{v_0 q_1 q_2}{\bar{k}(q_1^2 + q_2^2)} \right)^2 w_f(\mathbf{q}) \\
& \times \exp \left(- \left(i\kappa \mathbf{v} \cdot \mathbf{q} + \frac{\mathbf{D}^* \mathbf{q} \cdot \mathbf{q}}{\rho(\omega)} + \frac{\Lambda_p}{\rho(\omega)} \right) \tau' \right) dq_1 dq_2 \\
& - \Lambda_p \kappa \int_0^\tau d\tau'' \int_0^\tau d\tau' \int_{-\infty}^\infty \int_{-\infty}^\infty \left(\frac{v_0 q_1 q_2}{\bar{k}(q_1^2 + q_2^2)} \right)^2 w_f(\mathbf{q}) \\
& \times \exp \left(- \left(i\kappa \mathbf{v} \cdot \mathbf{q} + \frac{\mathbf{D}^* \mathbf{q} \cdot \mathbf{q}}{\rho(\omega)} + \frac{\Lambda_p}{\rho(\omega)} \right) \tau'' \right) \\
& \times \exp \left(- \left(i\kappa \mathbf{v} \cdot \mathbf{q} + \frac{\mathbf{D}^* \mathbf{q} \cdot \mathbf{q}}{\rho(\omega)} + \frac{\Lambda_p}{\rho(\omega)} \right) \tau' \right) dq_1 dq_2 . \quad (\text{A.3.5})
\end{aligned}$$

Without the Λ_p term, (A.3.5) again resembles equation (35) in Dagan (1988), which was for passive tracers. Following the steps for D_{11}^{eff} we used **MAPLE**[®] to evaluate the transverse coefficient as

$$\begin{aligned}
D_{22}^{\text{eff}} = & \Theta \int_s^\infty d\eta \int_0^\infty ds \frac{\pi}{4\kappa^5 (\xi^2 + \eta)^{3/2} (1 + \eta)^{3/2}} \\
& \times \left\{ A^* 2\Lambda_p^2 (\eta + 1) \left[2\Lambda_p^2 (\eta + 1) (\text{erf}(D) - 2\text{erf}(C) + \text{erf}(B)) \right. \right. \\
& + \kappa^2 ((\tau\Lambda_p + 1)\text{erf}(D) - (2\tau\Lambda_p + 5)\text{erf}(C) + 3\text{erf}(B)) \left. \right] \\
& + 2\Lambda_p \kappa (\eta + 1) [2\Lambda_p^2 (\eta + 1)(G - 2F + 1) + \kappa^2(G - 3F + 2)] \\
& \left. + \kappa^5 \tau F \right\} . \quad (\text{A.3.6})
\end{aligned}$$

Where $A^* = A\sqrt{1 + \eta}$ and B, C, D, F and G are as defined in (A.3.4).

A.3.3 The Off-diagonal Elements.

From (A.3.2), the off-diagonal elements are obtained by setting $n = 1, j = 2$ and $n = 2, j = 1$, which result into the products $L_1(\mathbf{q})L_2(\mathbf{q})$ and $L_2(\mathbf{q})L_1(\mathbf{q})$ respectively. From (5.15), the two products are equal implying a symmetric macrodispersion

tensor. The respective space integrals in the off-diagonal elements read

$$\int_{-\infty}^{\infty} \hat{q}_1 \exp\left(-i\kappa\hat{q}_1\hat{\tau}' - \hat{q}_1^2(1+\eta)\right) d\hat{q}_1 \int_{-\infty}^{\infty} \hat{q}_2^3 \exp(-\hat{q}_2^2(\xi^2 + \eta)) d\hat{q}_2$$

and

$$\int_{-\infty}^{\infty} \hat{q}_1 \exp\left(-i\kappa\hat{q}_1(\hat{\tau}' + \hat{\tau}'') - \hat{q}_1^2(1+\eta)\right) d\hat{q}_1 \int_{-\infty}^{\infty} \hat{q}_2^3 \exp(-\hat{q}_2^2(\xi^2 + \eta)) d\hat{q}_2 \ .$$

The respective products of \hat{q}_1 and \hat{q}_2^3 with the corresponding exponential functions are odd, making their integrals over the entire space zero. The symmetric tensor with zero off-diagonal elements was also obtained by Held et al. (2005).

References

- Ackerer, P., Younes, A. and Mose, R.: 1999, Modeling variable density flow and solute transport in porous medium: Numerical model and verification, *Transport in Porous Media* **35**(1), 345–373.
- Attinger, S.: 2006, Homogenization. Summer School, Utrecht.
- Attinger, S., Dentz, M., Kinzelbach, H. and Kinzelbach, W.: 1999, Temporal behaviour of a solute cloud in a chemically heterogeneous porous medium, *Journal of Fluid Mechanics* **386**, 77–104.
- Auriault, J. L.: 2002, Upscaling heterogeneous media by asymptotic expansions, *Journal of Engineering Mechanics* **128**(8), 817–822, doi:10.1061/(ASCE)0733-9399(2002)128:8(817).
- Bastian, P., Birken, K., Johannsen, K., Lang, S., Neuss, N. and Rentz-Reichert, H.: 1997, UG-a flexible software toolbox for solving partial differential equations, *Compt. Visualization Sci.* **1**, 1–40.
- Bear, J. and Bachmat, Y.: 1991, *Introduction to Modeling of Transport phenomena in porous media*, Kluwer.
- Bhadauria, B. S.: 2007, Double diffusive convection in a porous medium with modulated temperature on the boundaries, *Transport in Porous Media* **70**, 191–211.
- Brailovsky, I., Babchin, A., Frankel, M. and Sivashinsky, G.: 2006, Fingering instability in water-oil displacement, *Transport in Porous Media* **63**, 363–380, doi:10.1007/s11242-005-8430-z.

- Buès, M. A. and Aachib, M.: 1991, Effect of the heterogeneity of the solutions on the parameters of miscible displacement in saturated porous medium, *Experiments in Fluids* **11**, 25–32.
- Chang, S. and Slattery, J. C.: 1986, A linear stability analysis for miscible displacements, *Transport in porous media* **1**, 179–199.
- Chang, S. and Slattery, J. C.: 1988, Stability of vertical miscible displacements with developing density and viscosity gradients, *Transport in porous media* **3**, 277–297.
- Chao-Ying, J. and Hoetzel, H.: 2004, An experimental study of miscible displacements in porous media with variation of fluid density and viscosity, *Transport in Porous Media* **54**, 125–144.
- Chikhliwala, E. D., Huang, A. B. and Yortsos, Y. C.: 1988, Numerical study of the linear stability of immiscible displacement in porous media, *Transport in Porous Media* **3**, 257–276.
- Cioranescu, D. and Donato, P.: 1999, *An Introduction to Homogenization*, Oxford University Press.
- Coskuner, G.: 1993, Onset of viscous fingering for miscible liquid-liquid displacements in porous media, *Transport in Porous Media* **10**, 285–291.
- Coskuner, G. and Bentsen, R. G.: 1990, An extended theory to predict the onset of viscous instabilities for miscible displacements in porous media, *Transport in Porous Media* **5**, 473–490.
- Dagan, G.: 1986, Statistical theory of groundwater flow and transport: pore to laboratory, laboratory to formation, and formation to regional scale, *Water Resources Research* **22**(9), 120s–134s.
- Dagan, G.: 1987, Theory of solute transport by groundwater, *Ann. Rev. Fluid Mech.* **19**, 183–215.
- Dagan, G.: 1988, Time-dependent macrodispersion for solute transport in anisotropic heterogeneous aquifers, *Water Resources Research* **24**(9), 1491–1500.

- Dagan, G.: 1990, Transport in heterogeneous porous formations: Spatial moments, ergodicity and effective dispersion, *Water Resources Research* **26**(6), 1281–1290.
- Dautov, R. Z., Egorov, A. G., Nieber, J. L. and Sheshukov, A. Y.: 2002, Simulation of two-dimensional gravity-driven unstable flow, *in* C. methods in Water Resources (ed.), *Elsevier Ser. Dev. Water Sci.*, Vol. 47, Elsevier Sci. New York, pp. 9–16.
- Dentz, M.: 2000, *Temporal behaviour of transport parameters in heterogeneous porous media*, PhD thesis, Universitaet Heidelberg.
- Dentz, M., Kinzelbach, H., Attinger, S. and Kinzelbach, W.: 2003, Numerical studies of the transport behaviour of a passive solute in a two-dimensional incompressible random flow field, *Physical Review E* **67**, doi:10.1103/PhysRevE.67.046306.
- Diersch, H. J. G. and Kolditz, O.: 1998, Coupled groundwater flow and transport: 2. Thermohaline and 3D convection systems, *Advances in Water Resources* **21**(1), 401–425.
- Diersch, H. J. G. and Kolditz, O.: 2002, Variable-density flow and transport in porous media: approaches and challenges, *Advances in Water Resources* **25**, 899–944.
- Drazin, P. G. and Reid, W. H.: 2004, *Hydrodynamic stability*, Cambridge University Press.
- Drummond, I. T. and Horgan, R. R.: 1987, The effective permeability of a random medium, *J. Phys. A: Math. Gen* **20**, 4661–4672.
- Egorov, A. G., Dautov, R. Z., Nieber, J. L. and Sheshukov, A. Y.: 2003, Stability analysis of gravity-driven infiltrating flow, *Water Resources Research* **39**(9), 1266, doi:10.1029/2002WR001886.
- Elder, J. W.: 1967, Steady free convection in a porous medium heated from below, *J. Fluid Mech.* **27**(1), 29–48.

- Eliassi, M. and Glass, R. J.: 2001, On the continuum-scale modelling of gravity-driven fingers in unsaturated porous media: The inadequacy of the richards equation with standard monotonic constitutive relations and hysteretic equations of state, *Water Resources Research* **37**, 2019–2035.
- Farber, T. E.: 1997, *Fluid dynamics for physicists*, Cambridge University Press.
- Fein, E. and Schneider, A.: 1999, *d³f-Ein Programmpaket zur Modellierung von Dichtestroemungen*, GRS.
- Fetter, C. W.: 1999, *Contaminant hydrogeology*, Prentice Hall.
- Frind, E. O.: 1982, Simulation of long-term transient density-dependent transport in groundwater, *Advances in Water Resources* **5**, 73–88.
- Frolkovič, P.: 1998a, *d³f Ein Programmpaket zur Modellierung von Dichteströmungen*, GRS, chapter *d³f* documentation - the discretization, pp. 1–40.
- Frolkovič, P.: 1998b, Maximum principle and local mass balance for numerical solutions of transport equations coupled with variable density flow, *Acta Mathematica Universitatis Comenianae* **LXVII**(1), 137–157.
- Frolkovič, P. and De Schepper, H.: 2001, Numerical modelling of convection dominated transport coupled with density driven flow in porous media, *Advances in Water Resources* **24**, 63–72.
- Gelhar, L. W.: 1993, *Stochastic Subsurface Hydrology*, Prentice Hall, New Jersey.
- Gelhar, W. L. and Axness, C. L.: 1983, Three-dimensional stochastic analysis of macrodispersion in aquifers, *Water Resources Research* **19**(1), 161–180.
- Ghesmat, K. and Azaiez, J.: 2007, Viscous fingering instability in porous media: Effect of anisotropic velocity-dependent dispersion tensor, *Transport in porous Media*, doi:10.1007/s11242-007-9171-y .
- Held, R., Attinger, S. and Kinzelbach, W.: 2005, Homogenization and effective parameters for the Henry problem in heterogeneous formations, *Water Resources Research* **41**, W11420, doi:10.1029/2004WR003674.

- Helmig, R.: 2004, Hydromechanics. Lecture Notes at the University of Stuttgart.
- Holzbecher, E. O.: 1998, *Modelling density-driven flow in porous media: principles, numerics, software*, Springer, Berlin.
- Hornung, U.: 1996, *Homogenization and Porous Media*, Springer.
- Hsu, K.-C.: 2003, The influence of the log-conductivity auto-covariance structure on macrodispersion coefficients, *Journal of Contaminant Hydrology* **65**, 65—77.
- Irwin, N., Botz, M. M. and Greenkorn, R. A.: 1996, Experimental investigation of characteristic length scale in periodic heterogeneous porous media, *Transport in Porous Media* **25**, 235–246.
- Johannsen, K.: 2002, The elder problem-bifurcations and steady state solutions, *Computational Methods in Water Resources* **47**(1), 485–492.
- Johannsen, K.: 2003, On the validity of the boussinesq approximation for the elder problem, *Computational Geosciences* **7**(3), 169–182.
- Johannsen, K., Kinzelbach, W., Oswald, S. and Wittum, G.: 2002, The salt-pool benchmark problem-numerical simulation of saltwater up-coning in a porous medium, *Advances in Water Resources* **25**, 335–348.
- Kempers, L. J. T. M. and Haas, H.: 1994, The dispersion zone between fluids with different density and viscosity in a heterogeneous porous medium, *J. Fluid Mech.* **267**, 299—324.
- Kitanidis, P. K.: 1998, Prediction by the method of moments of transport in a heterogeneous formation, *Journal of Hydrology* **102**, 453—473.
- Knabner, P.: 2003, *Numerical Methods for Elliptic and Parabolic PDE's*, Springer.
- Kolditz, O.: 2001, *Computational Methods in Environmental Fluid Mechanics*, Springer.

- Kolditz, O., Ratke, R., Diersch, H. J. G. and Zielke, W.: 1998, Coupled groundwater flow and transport: 1. verification of variable-density flow and transport models, *Advances in Water Resources* **21**(1), 27–46.
- Kretz, V., Berest, P., Hulin, J. P. and Salin, D.: 2003, An experimental study of the effects of density and viscosity contrasts on macrodispersion in porous media, *Water Resources Research* **39**(2), 1032, doi:10.1029/2001WR001244.
- Kuznetsov, A. V. and Nield, D. A.: 2008, The effects of combined horizontal and vertical heterogeneity on the onset of convection in a porous medium: double diffusive case, *Transport in Porous Media* **72**, 157–170, doi: 10.1007/s11242-007-9141-4.
- Landman, A. J., Johannsen, K. and Schotting, R.: 2007, Density-dependent dispersion in heterogeneous porous media. part 1: A numerical study, *Advances in Water Resources* **30**, 2467–2480.
- Landman, A. J., Schotting, R., Egorov, A. and Demidov, D.: 2007, Density-dependent dispersion in heterogeneous porous media. part 2: Comparison with nonlinear models, *Advances in Water Resources* **30**, 2481–2498.
- Leveque, R. J.: 2002, *Finite Volume Methods for Hyperbolic Problems*, Cambridge University Press.
- Liu, H. and Dane, J.: 1996a, A criterion for gravitational instability in miscible dense plumes, *Journal of Contaminant Hydrology* **23**, 233–243.
- Liu, H. H. and Dane, J. H.: 1996b, Two approaches to modelling unstable flow and mixing of variable density fluids in porous media, *Transport in Porous Media* **23**, 219–236.
- Lunati, I., Attinger, S. and Kinzelbach, W.: 2002, Macrodispersivity for transport in arbitrary nonuniform flow fields: Asymptotic and pre-asymptotic results, *Water Resources Research* **38**(10), 1187, doi:10.1029/2001WR001203.

- Manickam, O. and Homsy, G. M.: 1993, Stability of miscible displacements in porous media with non monotonic viscosity profiles, *Phys. Fluids A* **5**(6), 1356–1367.
- Marle, C. M.: 1981, *Multiphase Flow in Porous Media*, Editions Technip.
- Meca, A. S., Alhama, F. and González-Fernández, C. F.: 2007, An efficient model for solving density driven groundwater flow problems based on the network simulation method, *Journal of hydrology* **339**, 39–53, doi: 10:1016/j.jhydrol.2007.03.003.
- Nield, D. A.: 1994, Estimation of an effective rayleigh number for convection in a vertically inhomogeneous porous medium or clear fluid, *Int. J. Heat and Fluid flow* **15**(4), 337–340.
- Nield, D. A. and Bejan, A.: 1992, *Convection in porous media*, Springer-Verlag.
- Oldenburg, C. M. and Pruess, K.: 1995, Dispersive transport dynamics in a strongly coupled groundwater-brine flow system, *Water Resources Research* **31**(2), 289–302.
- Oldenburg, C. M. and Pruess, K.: 1998, Layered thermohaline convection in hypersaline geothermal systems, *Transport in porous media* **33**, 29–63.
- Oltean, C., Felder, C. and Buès, M. A.: 2000, Density-driven flow and transport in saturated porous media: Infiltration with high permeability ratio, in L. R. Bentley, J. F. Sykes, C. A. Brebbia, W. G. Gray and G. F. Pinder (eds), *Proceedings of the international conference on Computational methods in Water Resources, Calgary, June 2000*, Vol. XIII, Balkema, Rotterdam, pp. 67–74.
- Pavliotis, G. A.: 2002, *Homogenization theory for advection-diffusion equations with mean flow*, PhD thesis, Rensselaer Polytechnic Institute, Troy New York.
- Pavliotis, G. A. and Stuart, A. M.: 2007, *Multiscale methods: averaging and homogenization*, Springer-Verlag.
- Perrine, R. L. and Gay, G. M.: 1966, Unstable miscible flow in heterogeneous systems, *Society of petroleum engineering journal* **6**, 228.

- Pieters, G. J. M.: 2004, *Stability and evolution of Gravity-driven flow in Porous Media applied to hydrological and ecological problems*, PhD thesis, Technische Universiteit Eindhoven.
- Reeves, M. and Ewiera, M. M. E.: 2000, Modeling density-dependent flow and transport, in L. R. Bentley, J. F. Sykes, C. A. Brebbia, W. G. Gray and G. F. Pinder (eds), *Proceedings of the international conference on Computational methods in Water Resources, Calgary, June 2000*, Vol. XIII, Balkema, Rotterdam, pp. 59–66.
- Robin, M. J. L., Gutjahr, A. L., Sudicky, A. L. and Wilson, E. A.: 1993, Cross-correlated random field generation with the direct fourier transform method, *Water Resources Research* **29**(7), 2385–2397.
- Rubin, Y.: 2003, *Applied Stochastic Hydrogeology*, Oxford University Press, New York.
- Schincariol, R. A.: 1998, Dispersive mixing dynamics of dense miscible plumes: natural perturbation initiation by local-scale heterogeneities, *Journal of Contaminant Hydrology* **34**, 247—271.
- Schincariol, R. A., Schwartz, F. and Mendoza, C. A.: 1997, Instabilities in variable density flows: Stability and sensitivity analyses for homogeneous and heterogeneous media, *Water Resources Research* **33**(1), 31–41.
- Schincariol, R. A. and Schwartz, F. W.: 1990, An experimental investigation of variable-density flow and mixing in homogeneous and heterogeneous media, *Water Resources Research* **26**(10), 2317–2329.
- Schincariol, R. A., Schwartz, F. W. and Mendoza, C. A.: 1994, On the generation of instabilities in variable density flow, *Water Resources Research* **30**(4), 913–927.
- Settari, A., Price, H. S. and Dupont, T.: 1977, Development and application of variational methods for simulation of miscible displacement in porous media, *Society of petroleum engineering journal* **17**, 228.

- Simmons, C. T., Fenstemaker, T. R. and Sharp, J. M.: 2001, Variable-density groundwater flow and solute transport in heterogeneous porous media: approaches, resolutions and future challenges, *Journal of Contaminant Hydrology* **52**, 245–275.
- Swartz, C. H. and Schwartz, F. W.: 1998, An experimental study of mixing and instability development in variable-density systems, *Journal of Contaminant Hydrology* **34**, 169–189.
- Talon, L., Martin, J., Rakotomalala, N. and Salin, D.: 2004, Stabilizing viscosity contrast effect on miscible displacement in heterogeneous porous media, using lattice bhatnagar-gross-krook simulations, *Physics of Fluids* **16**(12), 4408–4411.
- Tan, C. T. and Homsy, G. M.: 1986, Stability of miscible displacements in porous media: Rectilinear flow, *Phys. Fluids* **29**, 3549–3556.
- Ursino, N.: 2000, Linear stability analysis of infiltration, analytical and numerical solution, *Transport in Porous Media* **38**, 261–271.
- Van-Duijn, C. J., Pieters, G. J. M. and Raats, P. A. C.: 2004, Steady flows in unsaturated soils are stable, *Transport in Porous Media* **57**, 215–244.
- Wang, C. Y.: 2002, Convective stability in a rectangular box of fluid-saturated porous medium with constant pressure top and constant flux bottom heating, *Transport in Porous Media* **46**, 37–42.
- Wang, J. and Kitanidis, P.: 1999, Analysis of macrodispersion through volume averaging: comparison with stochastic theory, *Stochastic environmental research and risk assessment* **13**, 66–84.
- Welty, C. and Gelhar, W. L.: 1991, Stochastic analysis of the effects of fluid density and viscosity variability on macrodispersion in heterogeneous porous media, *Water Resources Research* **27**(8), 2061–2075.

- Welty, C., Kane III, A. C. and Kauffman, L. J.: 2003, Stochastic analysis of transverse dispersion in density-coupled transport in aquifers, *Water Resources Research* **39**(6), 1150, doi:10.1029/2002WR001631.
- Wooding, R. A.: 1962, Stability of an interface between miscible fluids in a porous medium, *Zeitschrift fuer angewandte Mathematik und Physik* **13**(3), 255–266.
- Woumeni, R. S. and Vauclin, M.: 2006, A field study of the coupled effects of aquifer stratification, fluid density and groundwater fluctuation on dispersivity assessments, *Advances in Water Resources* **29**(7), 181–198.

Sebständigkeitserklärung

Ich erkläre, daß ich die vorliegende Arbeit selbständig und unter Verwendug der angegebenen Hilfsmittel, persölichen Mitteilungen und Quellen angefertigt habe.

November 5, 2010 Jena.

Unterschrift des Verfassers /der Verfasserin

Acknowledgements/Danksagung

My sincere thanks go to my mentors Prof. Sabine Attinger and Dr. Florin Radu for the unwavering enthusiasm and keen interest shown in this work for the three years. My person has been tremendously improved during the time we have worked together. I'm also indebted to the co-operating work groups in the EDuR project for the advice I received during the project meetings and personal communications. Also to thank are Prof. Kai Totsche, Prof. Olaf Kolditz, Prof. Sacha Oswald and Dr. Michael Lampe for their advice and attention paid to the smallest of the small details in this work.

I also wish to thank Katharina Roß for the timely intervention that spared me blushes. The support from Prof. Attinger's work-group members at the UFZ in Leipzig is also greatly appreciated. Your willingness to help on the many occasions I requested left me humbled. Christoph, you were especially a blessing in every sense of the word. I also thank Prof. Totsche's work group at Uni Jena and everyone with whom we shared office space in the Wöllnitzerstr. You always made me feel at home, so far away from home.

To my friends Franklin, Rose, Theodore, Bony, Sisay and everyone with whom we spent many evenings that would otherwise have been uneventful, I greatly appreciated it. Helen, thank you for proofreading my manuscripts.

An alle Jenaer Kumpel, ich bedanke mich sehr für die Freundschaft. Mit euch fand ich in Jena ein neues Zuhause.

Last but not least, I thank my parents for letting me do the things I chose to do and all the family members for the support and encouragement. To Annette, I'm eternally grateful for allowing me inconvenience you whenever it was convenient for me.